ONLINE MODEL-BASED ESTIMATION FOR AUTOMATED OPTICAL SYSTEM ALIGNMENT AND PHASE RETRIEVAL ALGORITHM

A Dissertation

Presented to the Faculty of the Graduate School

of Cornell University

in Partial Fulfillment of the Requirements for the Degree of

Doctor of Philosophy

by

Joyce Fang

August 2018

ONLINE MODEL-BASED ESTIMATION FOR AUTOMATED OPTICAL SYSTEM ALIGNMENT AND PHASE RETRIEVAL ALGORITHM

Joyce Fang, Ph.D.

Cornell University 2018

Online model-based estimation is applied to two major applications in optics: Automated optical component alignment and wavefront reconstruction with simultaneous system parameter estimation. Both applications utilize mechanical perturbation in the optical system to generate phase diversity in real-time stochastic systems.

The first part of this study proposes a novel automated alignment method which improves efficiency and increases the flexibility of an optical system. Current optical systems with automated alignment capabilities are typically designed to include a dedicated wavefront sensor. Here, we demonstrate a self-aligning method for a reconfigurable system using only focal plane images. We define reconfigurable and reflective optical systems and simulate the images given misalignment parameters using ZEMAX software. We perform a principal component analysis (PCA) on the simulated dataset to obtain Karhunen-Loève (KL) modes, which form the basis set whose weights are the system measurements. A model function which maps the state to the measurement is learned using nonlinear least squares fitting and serves as the measurement function for the extended Kalman filter (EKF) and unscented Kalman filter (UKF) used to estimate the state and control the system. The observability and stability of the system are discussed. We present both simulated and experimental results of the full system in operation.

The second part of this study presents a novel algorithm for phase retrieval and optical system parameter estimation. Many wavefront reconstruction techniques estimate the amplitude and phase from multiple intensity measurements. One can generate phase diversity among these intensity measurements by varying certain parameters in the optical system. These parameters are subject to noise and disturbances, which might strongly degrade the accuracy of the reconstruction. The parallel algorithm iterative amplitude and phase retrieval (APR) have been proven to accurately reconstruct arbitrary wavefronts from multiple intensity measurements when system parameters are known exactly, given the ability to induce phase diversity between images. Such sets of intensity images with phase diversity can be generated by moving a lens in the optical system, but any position error on the lens will degenerate the reconstruction result. We demonstrate the use of an expectation-maximization (EM) algorithm with Kalman smoothing for recovering both the complex field and the lens position from a stack of intensity images. Our method successfully reduces the mean-squared-error of the estimated wavefront in comparison to an approach without position error estimation. We present and discuss the results of using a Kalman smoother and nonlinear least-square optimization for the estimation of the moving lens position.

We modify and extend the system variable estimation method to serial phase retrieval algorithm. We present the use of iterated extended Kalman filter (IEKF) to estimate the system variables in a multiple-image phase retrieval framework. An iterated extended Kalman filter is shown to effectively reduce the normalized mean-square-error of the reconstructed wavefront by estimating the defocus and transverse shifts of a moving camera in simulation. Experiments are conducted using two different test objects, and the results clearly demonstrate

the enhancement of detail and contrast of the wavefront when using the filter. A quadratic phase introduced by a convex lens is used with a binary mask as one of the test objects. The focal length estimated from the unwrapped phase agrees with the (±1% tolerance) value provided by the manufacturer.

BIOGRAPHICAL SKETCH

Joyce Fang was born in California on March 21st, 1989 and grew up in Taiwan. She attended her high school in Tainan, Taiwan, and played on the school basketball team. In 2011 Joyce completed her undergraduate degree at National Cheng Kung University in Taiwan. She also played on the women's basketball team in her department and served as team captain during her undergraduate years. Joyce holds a Master of Science in Mechanical Engineering from National Taiwan University. In her master she worked on computational mechanics. In 2013 she came to the United States to pursue her PhD degree in Mechanical Engineering at Cornell University in Ithaca, NY. Joyce Fang joined Space Imaging and Optical Systems Lab in January 2014. Her research focuses on automated optical system alignment and phase retrieval algorithm. She has held summer internships at Uber Technologies Inc. and Oculus VR, LLC during her graduate study. She enjoy snowboarding during the winter in Ithaca.

ACKNOWLEDGEMENTS

I would like to acknowledge all those who instructed, guided, and supported me along the journey to pursue an Ph.D.

Most importantly I would like to thank my advisor, Professor Dmitry Savransky for his guidance, direction, and support during my graduate study. I really appreciate everything I learned from him and I am very lucky to be his first PhD student. I would also like to thank Professor Hadas Kress-Gazit and Professor James Lloyd for being part of my dissertation committee and giving their time and expertise.

Thanks also to Professor Brian Kirby, Professor Mark Psiaki, Dr. Brandon Hencey for their insightful courses in research, estimation, and feedback control which allow me complete this thesis. I would like to thank Processor Elizabeth Fisher for her generous giving of optical equipments in our lab, and Dr. Douglas MacMartin for his guidance while I was his teaching assistant.

I would like to thank Marcia, Patti, Judy, Laura and all our staffs in MAE, for their patient and help on the administrative support during these years.

I would like to thank my fellow lab-mates Daniel Garrett, Gabriel Soto, Jacob Shapiro, Dean Keithly, Christian Delacroix, and James Lee. Without them I would not have been able to experience such an interesting journey of research. I would also like to thank all my friends at Cornell who made the time in Ithaca very enjoyable.

Lastly, I would like to especially thank my family. I thank them for being in my life and supporting me for all the decisions I have made.

TABLE OF CONTENTS

LIST OF TABLES

LIST OF FIGURES

CHAPTER 1

INTRODUCTION

Advanced optical systems are widely used in today's technology, including observing and tracing biological and chemical compounds with microscopes [1], detecting and imaging exoplanets and disks with ground-based and space telescopes [2], creating three-dimensional scenes with virtual reality (VR) displays [3], and sensing and correcting wavefront aberration for medical purposes [4]. As scientific and engineering optical systems become more complex, there has been a steady push for increased automation in their operation.

1.1 Wavefront Sensing

Wavefront sensing techniques are widely used in current imaging systems such as holographic microscopes [5, 6], adaptive optical systems in astronomical telescopes [7, 8], and phase-contrast X-ray imagers [9, 10]. There exist numerous wavefront measurement methods, roughly split between those employing a reference beam for interferometry, and techniques without a reference beam that utilize intensity measurements or other wavefront sensors. An interferometer measures the interference patterns of light for wavefront sensing and is commonly used in surface quality test [11]. These devices are generally more expensive, difficult to align, and require a great amount of space. In this thesis we focus on the wavefront sensing methods without a reference beam.

The most commonly used wavefront sensor that utilizes intensity measurements is a Shack-Hartmann wavefront sensor. It measures the displacements

of the intensity spots formed by a lens array to calculate wavefront tilt [12]. A Shack-Hartmann wavefront sensor can achieve high accuracy and large aberration measurement range. It is widely used in advanced adaptive optics system [13], holographic imaging [14], and standard testing of optical components. A beam splitter is usually required when using the Shack-Hartmann sensor in an existing optical system. This increases the complexity of, decreases the throughput of the system and, more importantly, can introduce non-common path errors.

There exist, however, various wavefront sensing schemes employing the primary system sensor and eliminating the need for dedicated wavefront sensors [15, 16]. These techniques are already being applied to current scientific instrumentation [17]. Some focal-plane wavefront sensing methods use pupil plane masking or multiple detectors to introduce phase diversity and reconstruct wavefront error [18, 19, 20]. The image moment-based wavefront sensing (IWFS) method uses image moment of measured point spread function (PSF) for alignment correction [21]. Focus diversity (FD) is introduced to break the nonlinearity and allows the system to sense full-field wavefront aberration. Certain applications use a deformable mirror to produce phase diversity for use in complex field estimation [22, 23]. Alternatively, asymmetric pupil masks can be used in adaptive optics systems for wavefront sensing and correction [20]. In this study, we are primarily interested in using mechanical parts to introduce phase diversity in the intensity measurements.

1.2 Optical Alignment

An automated optical alignment system can save the time and energy spent on manual alignment. This makes the assembly process of many optical devices, including microscopes, medical sensing devices, and camera systems, more efficient. Self-aligning techniques can also improve the alignment between lenses of a virtual reality headset and human eyes. Most current VR headset models only allow a manual adjustment of the interpupillary distance (IPD). Moreover, automated alignment is very important for space optical systems. Many satellites and space telescopes cannot be serviced after their launch. A slight inaccuracy in the engineering design or disturbance during launch or on orbit can easily cause optical misalignment [24]. The importance and benefits of automatically aligning an optical system increase with the complexity and flexibility of the instruments themselves. Of particular interest is the ability for complex instruments to automatically align using existing internal imaging sensors, without requiring the addition of dedicated wavefront sensors, or other large changes to their basic beam paths.

Many static components in optical systems (such as reimaging and collimating optics) are bolted down after begin carefully aligned the first time. In these cases, the manual alignment procedures are time consuming and optical misalignment caused by environmental disturbances cannot be fixed. A reconfigurable system, which has multiple filters or other components in pupil and focal planes, needs the ability to self-align, and may be made more flexible if internal components are allowed to move. For example, the Gemini Planet Imager (GPI) [25], a ground-based instrument which includes a coronagraph and an extreme adaptive optics system for direct imaging of extrasolar planets, has au-

tomated alignment features on coronagraph components using computer vision algorithms [26]. The closed loop control process allows GPI to achieve high precision alignment in the presence of a continuously changing gravity gradient and thermal flexure. A distributed optical system, such as an optical communication system, needs to be accurately aligned within limited space and setup time. Finally, there are cases where allowing for motion degrees of freedom creates new sensing capabilities as in interferometric devices and self-coherent imaging systems [27].

The most widely used alignment methods relate misalignment parameters to optical wavefront error as measured by various wavefront sensing devices. One of these methods involves mapping misalignments to Zernike terms using a sensitivity table [28, 29]. Sensitivity tables, however, are limited in their accuracy when the misalignments are large and the nonlinearity increases. Merit function regression solves this problem and is presented in Kim et al. [30]. This method estimates the misalignment by performing damped least square optimization with merit function values defined as the difference between the measured and ideal Zernike coefficients of the optical system wavefronts. Lee et al. [31] proposed a differential wavefront sampling (DWS) method for the efficient alignment of optical systems. By perturbing optical elements this technique generates a set of linear equations used to solve for the misalignment of a system. Oh et al. [32] integrated revised DWS sampling method with MFR nonlinear optimization on a three-mirror anastigmat optical system. The integrated alignment method results in better alignment accuracies than standard MFR and DWS methods. Instead of using a numerical approach, Gu et al. [33] presented a method for aligning a three-mirror anastigmatic telescope using nodal aberration theory. These methods all require measuring the wavefront error of

the system using a dedicated wavefront sensor, such as Shack-Hartmann wavefront sensor.

In this thesis, we propose a method which corrects the misalignment of an optical systems with existing internal imaging instruments in the system, such as a focal plane camera, there by saving the extra resources and space need for splitting the beam, and avoiding throughput loss and non-common path error. Moreover, this approach makes it easier to retrofit an existing optical system to perform self-alignment since the major difference is changing the static optical components to kinematic ones.

1.3 Phase Retrieval Algorithm

This section focuses on the algorithm for the phase retrieval technique which is one of the wavefront sensing methods discussed in Section 1.1. In recent years, various phase retrieval methods have been proposed for wavefront reconstruction without a reference beam, a wavefront sensor, or additional optical components. The phase of a complex field can be retrieved using a set of defocused images. The well-known Gerchberg-Saxton algorithm [34] was invented for iteratively retrieving the phase of a wavefront given its intensity. Multiple phase retrieval algorithms based on the Gerchberg-Saxton algorithm have also been shown to produce improved convergence rates. The generalized Gerchberg-Saxton algorithm can be used for any phase retrieval problem with proper constraints [35].

Phase retrieval is a high-dimensional ill-conditioned problem in complex domain. Adding intensity data from the measurement by changing the optical pa-

rameters in the system can improve the estimation of the phase. Multiple-image phase retrieval can be primarily separated into two types: parallel computing and serial computing [36]. The parallel computing methods estimate the complex field with multiple measurements simultaneously and the computation using those measurement are independent of each other. While the serial computing methods use the output of the previous measurement as the input of the next measurement after phase diversity applied, which is suitable for dynamic phase retrieval application. The parallel computing technique amplitude-phase retrieval (APR) is used to retrieve amplitude and phase simultaneously with multiple intensity images [37, 38]. The current estimate is forward propagated to each measurement plane, and the amplitude of the field is replaced at the measurement plane. The new estimated state is obtained by averaging over the back propagated complex fields from each measurement plane. The multi-stage algorithm is one of the serial computing structure, where the forward and backward propagation between the object and observed image plane are applied in gyrator transform domain [39]. Another commonly used serial computing method is the single-beam, multiple intensity reconstruction (SBMIR) algorithm. In this method the propagation is completed between observed image planes. The complex field is estimated after the algorithm reaches the last measurement and back propagated to the object plane [40].

Many optical setups use multiple detectors or a moving camera to obtain multiple intensity images [40]. The existing position error might strongly degrade the precision of the reconstruction [41]. Some applications place the focusing lens instead of the camera on a translation stage and move the lens to produce defocused images for amplitude and phase retrieval [42]. This avoids potential positioning errors while moving the component on the translation stage.

With the growing computing power the real-time wavefront reconstruction using iterative phase retrieval algorithm become more achievable. Advanced optical devices, such as deformable lens [43] and digital micromirror device (DMD) [44], are used to improve the image acquisition speed.

In this thesis, we are interested in simultaneously estimating the complex wavefront and the unknown system variables. We assume the uncertainly of the system is an unobserved Markov process, and combine Bayesian filter for estimating focus diversity and iterative phase retrieval algorithms. Our work focus on estimating mechanical uncertainty but the concept can be applied on other devices that generates the phase diversity by changing the unknown variables in the optical system. Objects with gradually changing wavefront, including cellular movement and deformation with greater characteristic times [45] and industrial paint drying process [46], are potential applications for dynamic iterative phase retrieval algorithm.

1.4 Kalman Filtering

Kalman filtering is a sequential estimation algorithm that estimates partially observed states of a dynamic system using a series of observations, a dynamic or probabilistic model of the system, and statistical models of the system's process and observation measurement noise. It is an optimal estimator for a linear Gaussian dynamical system. The Kalman filter algorithm iterates over two steps, dynamic propagation and measurement update. The dynamic propagation step propagates the previous state estimate through state transition and control-input model to predict an current estimate. This current estimate is

known as the a priori state estimate which does not include the information of current observation. In the measurement update step the a priori estimated is combined with current measurement information to improve the state estimate to the a posteriori estimate [47].

Since most engineering problems are nonlinear, many algorithms have been developed to apply Kalman filtering method to nonlinear systems. An extended Kalman filter (EKF) is a nonlinear version of Kalman filter which uses local linearization of the nonlinear system dynamics to approximate the mean and covariance of the current state estimate [47]. The model includes nonlinear state transition and measurement functions which cannot be directly applied to the covariance computation. The Jacobians of the nonlinear function are computed with the current states, then used for covariance computation in EKF algorithm. In practice, an iterated extended Kalman filter (IEKF) is used for the forward filtering pass. IEKF is an iterative version of EKF that ensures convergence in the measurement update step [47, 48]. It improves the accuracy of the EKF by taking multiple Gauss-Newton steps during each filter iteration.

The EKF is the standard technique for stochastic nonlinear estimation. However, it provides only first-order approximation and neglects the higher order terms in the Taylor expansions. In some case it is difficult to derive analytical expressions for the Jacobians of the nonlinear functions and also very costly to compute them in real-time. The unscented Kalman filter (UKF), also known as the sigma points filter, addresses the approximation issues of the EKF. It uses a minimal set of carefully chosen sample points to obtain the true mean and covariance of the Gaussian random variable in the prediction step, and captures the posterior mean and covariance with a higher-order approximation [49, 50].

The UKF is more computationally intensive than the EKF, but still orders of magnitude faster than the IEKF. The UKF might diverge in the case when the nonlinear functions have discontinuities or singularities. Kalman filtering is widely used in optical state estimation and wavefront control, including linear [51, 52] and nonlinear [53] filters. In this thesis, we apply Kalman filtering to automated optical alignment and phase retrieval algorithms.

1.5 Dissertation Overview

The overall theme of this dissertation is solving the estimation problem in optical systems involving mechanical degrees of freedom. Two main topics are presented in this thesis: 1. An innovative method for automated optical alignment. 2. A novel algorithm for phase retrieval with diversity estimation. The automated optical alignment is presented in chapter 2 and chapter 3, and the phase retrieval method is discussed in chapter 4 and chapter 5. Both topics include simulation and experimental result from the SIOS Optics Laboratory at Cornell.

Chapter 2 presents the idea of automated optical alignment with focal plane sensing and solves a toy problem of a single lens system. We applied a fundamental perturbation control method to the problem and introduce the devices and components used in the SIOS Optics Laboratory. A Gaussian beam is passed through a lens, and the deformation of the spot image is analyzed to determine the misalignments on the lens. Corrections based on these measurements are applied in closed loop to align the system. We discuss various techniques for mitigating measurement errors, characterizing the system and op-

erating the control loop and present results from the experiment. The method only detects low order features which is not directly related to the aberration modes caused by the misalignments. A better focal-plane sensing and automated alignment scheme is presented in the next chapter.

Chapter 3 demonstrates a self-aligning method for a reconfigurable system using only focal plane images. We define a two lens optical system with eight degrees of freedom. Images are simulated given misalignment parameters using ZEMAX software. We perform a principal component analysis (PCA) on the simulated dataset to obtain Karhunen-Loève (KL) modes, which form the basis set whose weights are the system measurements. A model function which maps the state to the measurement is learned using multivariate regression and serves as the measurement function for the optimal estimator (Extended and Unscented Kalman filters) used to calculate control inputs to align the system. We present and discuss both simulated and experimental results of the full system in operation. We also applied the automated alignment method to a reflective optical system. An off-axis parabolic mirror (OAP) alignment with optical setup similar to a scanning microscope is presented.

Chapter 4 presents an amplitude and phase retrieval method with simultaneous diversity estimation using expectation-maximization algorithm. We propose using recursive Bayesian filtering for focus diversity estimation in iterative phase retrieval algorithm. The intensity images with phase diversity are generated by moving a lens in the optical system. The position error on the lens will degenerate the reconstruction result. We demonstrate the use of an expectation-maximization (EM) algorithm with Kalman smoothing for recovering both the complex field and the lens position from a stack of intensity images. The com-

plex field is estimated using the parallel APR algorithm in the maximization step, and the focus diversity is estimated using Kalman smoother in the expectation step. Our method successfully reduces the mean-squared-error of the estimated wavefront in comparison to an approach without position error estimation. We present and discuss the results of using a Kalman smoother and nonlinear least-square optimization for the estimation of the moving lens position.

Chapter 5 discusses dual estimation of complex wavefront and focus diversity using serial computing phase retrieval algorithm and stochastic filtering techniques. We present the use of extended Kalman filtering to estimate the system variables in a multiple-image phase retrieval framework. An iterated extended Kalman filter is shown to effectively reduce the normalized mean-square-error of the reconstructed wavefront by estimating the defocus and transverse shifts of a moving camera in simulation. An experiment is conducted in the SIOS Optics Lab with phase diversity generated by a moving camera. Experiments are conducted using two different test objects, and the results clearly demonstrate the enhancement of detail and contrast of the wavefront when using the filter. A quadratic phase introduced by a convex lens is used with a binary mask as one of the test objects. The focal length estimated from the unwrapped phase agrees with the (±1% tolerance) value provided by the manufacturer. The algorithm framework is suitable for dynamic reconstruction. With the growing of hardware technology and computing power the method has the potential to be implemented in real-time where the stochastic online algorithm is preferred over batch estimation. Although our experiment is implemented with mechanical moving device, the same method can be applied on advanced hardware setups. For example, estimating the focus of a tunable liquid lens on-

line with the wavefront retrieval. This has the potential to avoid extra lookup tables and reduce the time for calibration.

Chapter 6 summarizes the final conclusions and outlines directions for future research in wavefront estimation of imaging systems involving mechanical and focus diversity variation.

CHAPTER 2

AUTOMATED ALIGNMENT OF A SINGLE LENS USING IMAGE FEATURE DETECTION

In this chapter we present a naive approach, which utilize the image processing and fundamental feedback control, to align a single lens system using only focal plane intensity measurement. The image feature of a Gaussian spot is analyzed to determine the tilt and shift misalignments on the lens, and the corrections based on these features are applied in closed loop to align the system. We introduce the SIOS Optics laboratory at Cornell and present the first on bench experiment. Finally, we discuss the lacking of the naive approach and move forward the advanced focal plane alignment method is Chapter 3.

2.1 Methodology

In this section we present the image feature detection and control methods for aligning the optical component using focal plane sensing. Figure 2.1 shows a schematic of the control system. Each block represents either hardware in the system or a software program. The concept is to control the moving component in the optical system and achieve alignment by feeding back the image information obtained from the CCD camera. A collimated beam goes through the optical system with a moving component and forms a final image on the CCD camera. The final image is then sent to the measurement system which extracts specific features to quantify the system misalignment. Finally, the system feeds back the measurement error and the control loop is established.

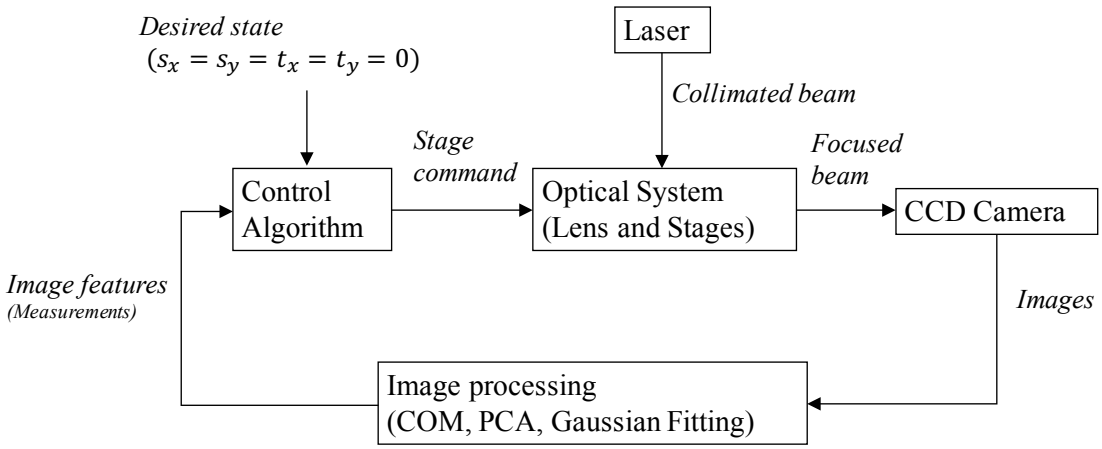

Figure 2.1: Schematic of the control system using image feature detection.

The model of the optical system block in Figure 2.1 is a single lens system shown in Figure 2.2. The z-axis is along the beam path and the x-y plane is normal to the beam path, with the x-axis along the vertical. The gray ellipses and red lines represent lenses and the beam path. The incoming laser beam is passed through a spatial filter to generate a axisymmetric Gaussian beam. A collimated beam passes through the moving lens and is focused on a CCD detector. Our goal is to calibrate the moving lens, which has 4 degrees of freedoms: translation in x and y and tip and tilt about z. The states s_x and s_y in the control procedure shown in Figure 2.1 correspond to the lens shift in the x and y directions, t_x and t_y are tip and tilt.

2.1.1 Image Feature Detection

To precisely estimate the lens misalignments, we need to have a robust image processing method to extract important features of the images. Image process-

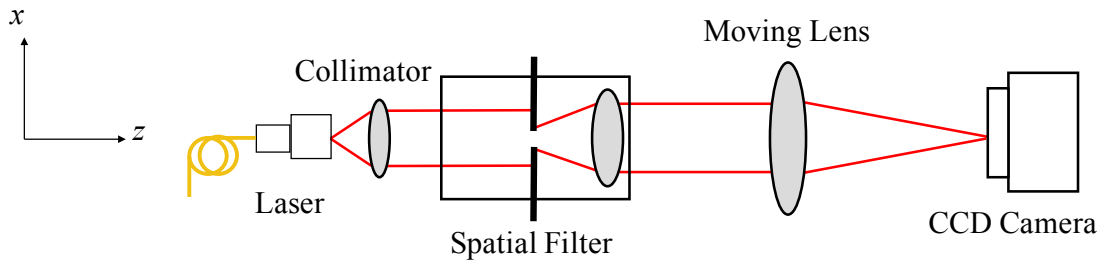

Figure 2.2: Single lens optical system with 4 degrees of freedom.

ing techniques, including center of mass (COM), principal component analysis (PCA) [54], and Gaussian fitting are used for feature detection [55]. First, we set a threshold and use COM to estimate the center of the image spot. Next, PCA is used to estimate the semi-major and minor axes, and rotation of the ellipse. Finally, we use the parameters obtained via COM and PCA as the starting points for a two dimensional Gaussian fitting to precisely measure the aspect ratio and rotation of the image.

Figure 2.3(a) shows a simulated image when the lens is misaligned. The simulated image is obtained using paraxial ray tracing simplified from geometrical optics. The misalignments cause the spot center to move, and induce an elongation in the spot, giving it a non-unity aspect ratio and associated rotation. The magenta lines are center axes of the image frame. We set the threshold value to be 2-3 times higher than the image noise, and a weighted COM is used compute the center of the image with pixel values above the threshold. We then use PCA to estimate the semi-major and minor axes with respect to the center of mass. For all pixels above threshold, we package x and y pixel coordinates into vector $\boldsymbol{r}_x$ and $\boldsymbol{r}_y$ and calculate the deviations from the mean:

$$\boldsymbol{M} = [\boldsymbol{r}_x - m_x \quad \boldsymbol{r}_y - m_y] \tag{2.1}$$

where m_x and m_y are the center of image obtain by COM. $\boldsymbol{M}$ is a $N_p \times 2$ matrix where N_p is the number of selected pixels. The covariance of $\boldsymbol{M}$ is:

$$\boldsymbol{C} = \frac{\boldsymbol{M}\boldsymbol{M}^T}{N-1} \tag{2.2}$$

where $(\cdot)^T$ is the transpose operator. The covariance matrix $\boldsymbol{C}$ can then be decomposed as:

$$\boldsymbol{C}\boldsymbol{V} = \boldsymbol{V}\boldsymbol{\Lambda} \tag{2.3}$$

where $\boldsymbol{V}$ is the eigenvectors of $\boldsymbol{C}$, and $\boldsymbol{\Lambda}$ is the diagonal matrix of the eigenvalues. The eigenvector corresponding to greater eigenvalue represents the principal axis, which is the semi-major axis in our case. Similarly, the eigenvector with smaller eigenvalue represents the semi-minor axis.

After the center position, semi-major and minor axes are estimated, we extract a smaller frame with center at the estimated m_x and m_y. We apply a Gaussian fit to the subframe:

$$\begin{aligned} F(x,y) &= G_1 + G_2 \exp\left(\frac{-(\frac{x'}{a})^2 - (\frac{y'}{b})^2}{2}\right) \\ x' &= (x - C_x)\cos\phi - (y - C_y)\sin\phi \\ y' &= (x - C_x)\sin\phi + (y - C_y)\cos\phi \end{aligned} \tag{2.4}$$

using the parameters obtained via COM and PCA as initial points for the fit. The unknown parameters (C_x, C_y) represent the center position of the Gaussian spot, (G_1, G_2) represent the Gaussian coefficients, (a, b) represent the semi-major and minor axis, and ϕ represents the rotational angle of the ellipse. The Gaussian fitting result give us the measurements used to calibrate the shift, tip, and tilt misalignments. Figure 2.3 shows the simulated image and the Gaussian fitting result of the image. The yellow frame in Figure 2.3(a) is the region of interest in Gaussian fitting. The black dot is the Gaussian center (C_x, C_y), and the green line

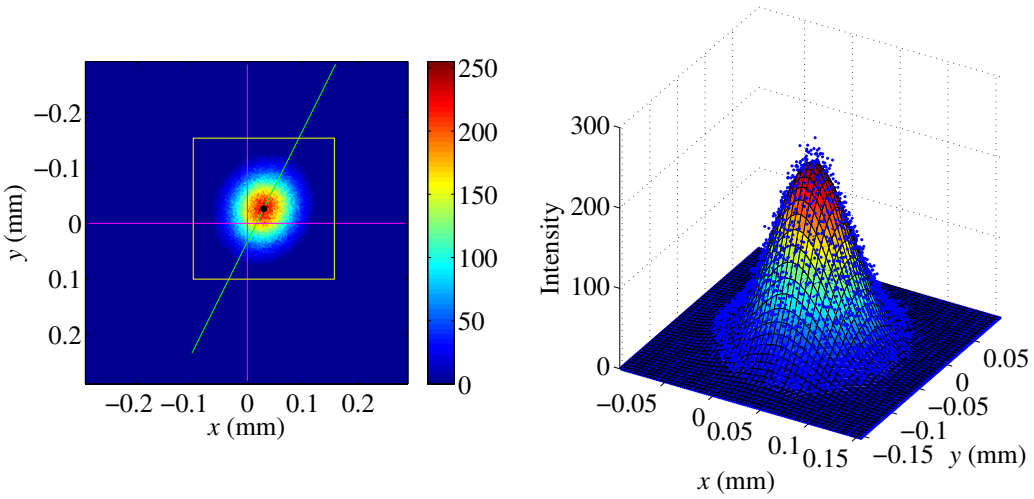

(a) (b)

Figure 2.3: Feature detection of a simulated image: (a)Image and the sub-frame, (b) Gaussian fitting result of (a).

shows the direction of the semi-major axis. Figure 2.3(b) shows a surface plot of the Gaussian fitting method. The blue dots represent the data and the colored surface is the fitting result.

2.1.2 Control Procedure

To design a control algorithm to correct misalignments, we first need to find the mapping from our measurements to the misalignment parameters. While it is difficult to decouple the effects of shift from tip and tilt, we can exploit the change in the spot shape caused by the tip and tilt misalignments. Both tip-tilt and shift misalignments will cause the image center to shift, but tip and tilt errors will also deform the image spot into an elliptical shape. In this case, the aspect ratio of the spot (a/b) and the rotation of the ellipse (ϕ) allow us to characterize the tilt errors. We can then decouple tip-tilt from shift misalignments.

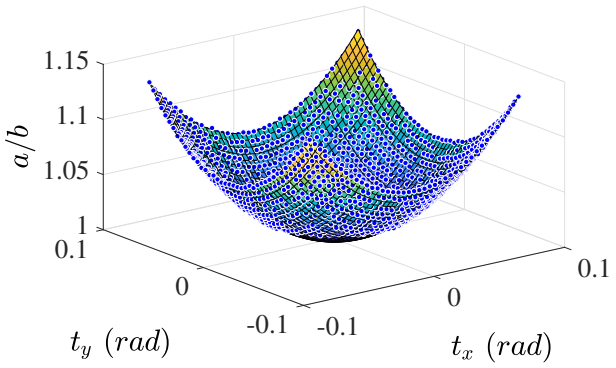

Figure 2.4: Aspect ratio of the ellipse as functions of tip-tilt misalignments.

Figure 2.1.2 shows a second order polynomial fit to data generated by scanning through different tip and tilt settings and measuring the aspect ratio of the spots produced. The resulting surface has a global minimum at the center, which corresponds to zero tip and tilt. The angle measurement $\phi \in [0, \pi)$ is not as robust as the aspect ratio for determining the system state, we use the aspect ratio (which is nicely symmetric about the zero point) when designing our control algorithm.

Figure 2.5 shows the steps of our control procedure as a flow chart. Each rectangular block represents an action, and each diamond block represents a logical branch point. b_A, b_B, b_C, and b_D are boolean variables while g_1, g_2, g_3, and g_4 correspond to the stage values of shift in x and y, and tip and tilt, respectively. The four boolean parameters, (b_A, b_B, b_C, and b_D) are used to determine when to break out of the global loop and subloops, and are initialized to $(1, 1, 0, 0)$. We break each control step into two parts: correction of the shift misalignment and correction of the tip-tilt misalignment, labeled $\mathbf{P}_s$ and $\mathbf{P}_t$, respectively. Process $\mathbf{P}_g$ represents the external loop. In process $\mathbf{P}_s$ we measure C_x and C_y and compare to a threshold β_s. We proceed to $\mathbf{P}_t$ if the absolute values of C_x and C_y are both below β_s. Otherwise, we set b_A to 0 and iteratively update g_1 and g_2 until C_x and

C_y are below the threshold.

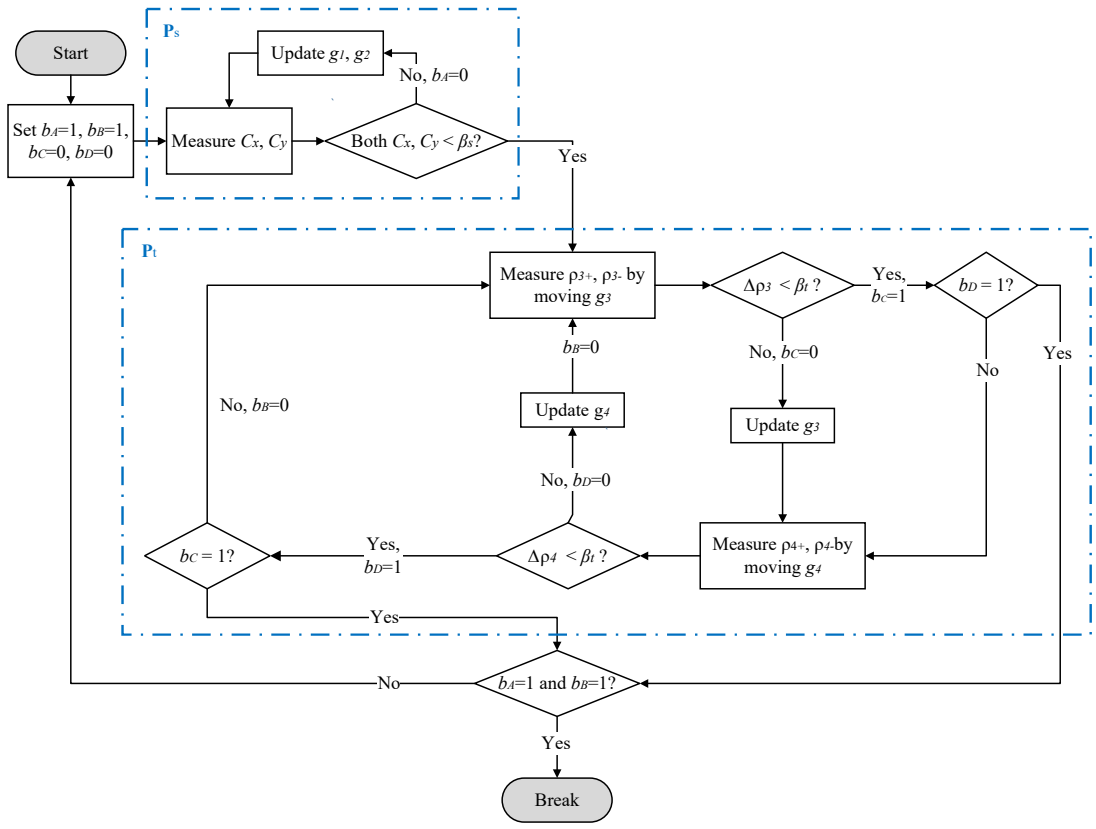

Figure 2.5: Decision chart of the control algorithm.

We can see in Figure 2.1.2 that the aspect ratio is close to 1 when t_x and t_y are small. This indicates that the relative measurement error is greater in those regions of the phase space. To avoid using those data in our calibration procedure, we measure aspect ratios that are away from the global minimum. We apply a control effort Δg in each direction to the tip-tilt stages g_3 and g_4:

$$\begin{aligned} g_{3+} &= g_3 + \Delta g, \quad g_{3-} = g_3 - \Delta g \\ g_{4+} &= g_4 + \Delta g, \quad g_{4-} = g_4 - \Delta g \end{aligned} \tag{2.5}$$

and measure the aspect ratio at these position as ρ_{3+}, ρ_{3-}, ρ_{4+}, and ρ_{4-}, where $\rho = a/b$. Assuming the aspect ratio surface is symmetric, the pairs of aspect

ratios should have the same values when the lens is aligned. We set

$$\begin{aligned} \Delta\rho_3 &= \rho_{3+} - \rho_{3-} \\ \Delta\rho_4 &= \rho_{4+} - \rho_{4-} \end{aligned} \tag{2.6}$$

and use these values as the error feedback in the $\mathbf{P}_t$ loop. This loop terminates when the errors are below a threshold β_t, in which case b_C and b_D are set to 1.

When both b_C and b_D are 1, we check whether either b_A and b_B are 0, in which case a new iteration of $\mathbf{P}_g$ is started. If both b_A and b_B are 1, this implies that b_C and b_D are also 1, and we consider the system to be aligned and break the outer loop. This only happens when two events occur in series in the $\mathbf{P}_g$:

1. $|C_x|$ and $|C_y|$ are both smaller than β_s on their initial measurement (without needing to update g_1 and g_2)
2. $\Delta\rho_3$ and $\Delta\rho_4$ are both smaller than β_t on their initial measurement (without needing to update g_3 and g_4).

2.2 Experiment

2.2.1 SIOS Optics Laboratory

The SIOS Optics Laboratory at Cornell currently consists of optical devices and components for the automated alignment and wavefront reconstruction experiments. The main devices include laser source, CCD camera, motorized stages as shown in Table 2.1. These devices are used in most of the experiments presented this thesis. Individual optical component used in a specific experiment

will be listed out in each experiment section. The laser, CCD, and all stages can be drive remotely with the software interface in MATLAB.

Table 2.1: List of main devices in SIOS Optics Laboratory

List	**Description**
Laser source	*Thorlabs 4-Channel MCLS1*: • wavelength λ = 520, 635, 670, 785 *nm*
Motorized stages	*Thorlabs translation stage PT1-Z8*: • range: 0-25*mm*, min increment: 100*nm*, Backlash < 12 μm *Thorlabs tip-tilt stage KS1-Z8*: • range: ±4°, resolution: 6*arcsec*, Backlash < 8 μm
CCD Camera	*Apogee A694*: • 16 bits, pixel size: 4.54μm, array size: 2750×2200

2.2.2 Setup

Figure 2.6 shows the experimental setup for the single lens model shown in Figure 2.2. The laser, stages, and camera in the system are listed in Table 2.1. Additional optical components include a collimator, Thorlabs KT310 spatial filter, and a 200 *mm* bi-convex lens. The 200 *mm* lens is mounted on the tip-tilt motorized stage which is connected to the translation stages moving along x and y axes.

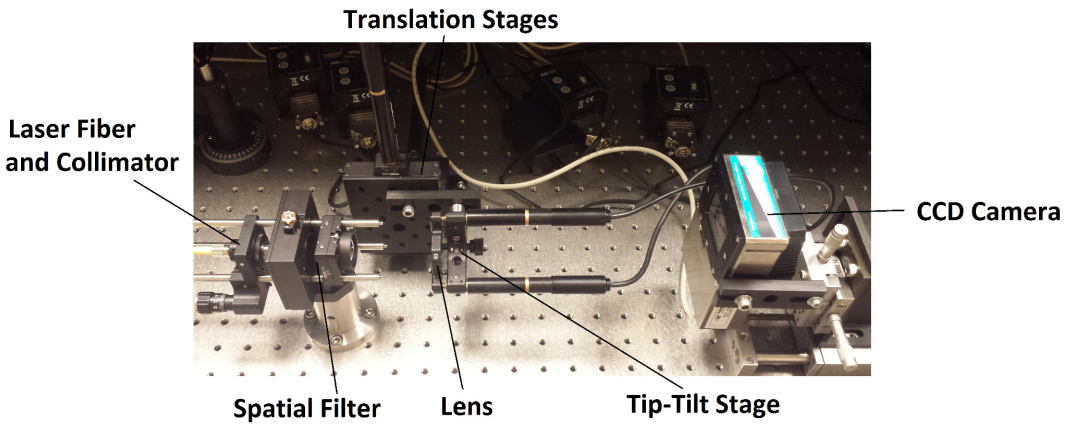

Figure 2.6: Experiment setup for examining the single lens model in Figure 2.2.

2.2.3 Results

Before attempting to run the closed loop control on our experimental setup, we first validated our simulated measurement algorithm, and the carried out precision and accuracy tests on the measurements, as described below.

Figure 2.7 shows the image processing steps described in Section 2.1.1 applied to real data. Figure 2.7(a) is the original image, where the magenta lines represent the central axes of the image frame. The weighted center of mass (m_x,m_y) of the spot is shown as the blue circle in Figure 2.7(b). The image in Figure 2.7(b) is a binary mask of the original image used to find the principal axis of the spot shown as the cyan line. The values found by the COM and PCA steps are then used as initial conditions in the final Gaussian fit carried out on the yellow subframe in Figure 2.7(b), with the results shown in Figure 2.7(c).

Figure 2.8 shows the precision test of the measurement. The red dots are measured when all the stages are stationary. To measure the precision of the

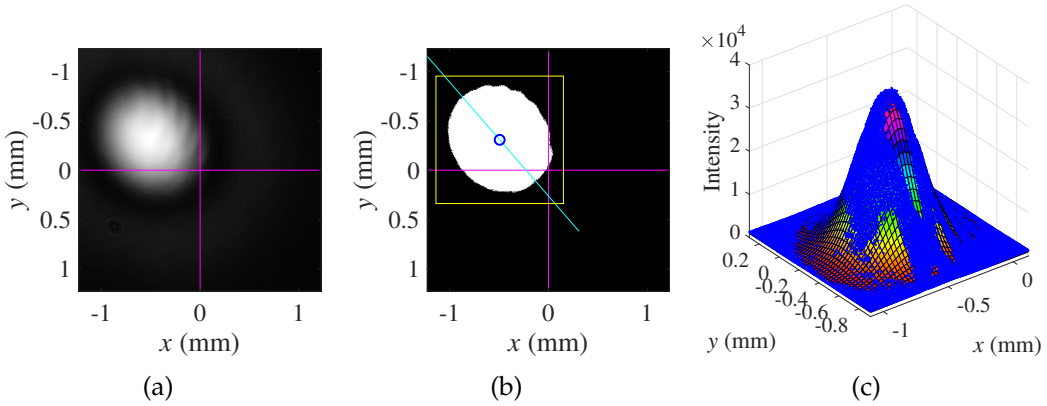

Figure 2.7: Feature detection steps in experiment. (a) Original image. (b) Binary-valued image. (c) Gaussian fitting result.

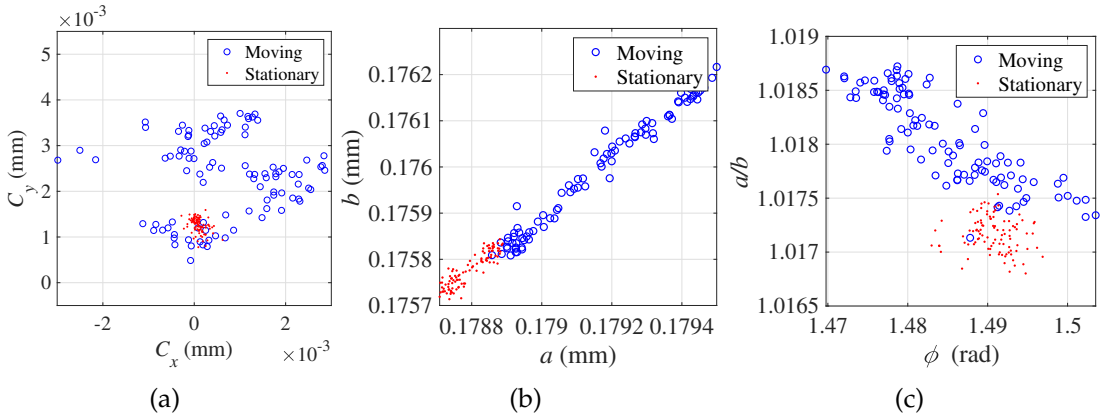

Figure 2.8: Precision test of (a) C_x and C_y, (b) a and b, and (c) ϕ and a/b under moving and stationary conditions.

tip-tilt stage, we increase and decrease g_3 and g_4 by $2mm$, and then return them to their original settings. The blue circles in Figure 2.8 are the result of measurements made after the stages have been moved. The moving measurements have relatively low precision compared to the stationary data indicating a large control error in the motorized stages. Figure 2.8(a), 2.8(b), and 2.8(c) are the test results of (C_x, C_y), (a, b), and (ϕ, a/b), respectively. In Figure 2.8(a), the stationary precision of the center position is within 1 μm, and the moving precision is around one image pixel (4.54 μm).

Figure 2.9 to 2.12 show the results of applying the control procedure described in Section 2.1.2 with thresholds $\beta_s = 1\ \mu m$ and $\beta_t = 0.001$. Figure 2.9 shows the convergence of the center position C_x and C_y. The bottom x-axis denotes the local steps in shift process $\mathbf{P}_s$, while the top x axis represents the global steps in process $\mathbf{P}_g$. The blue dots represent the measurement of C_x in process $\mathbf{P}_s$ in Figure 2.5, and the red stars represent C_y. The circle marks are the global steps where the $\mathbf{P}_s$ process converges below β_s. Figure 2.10 shows the translation stage values g_1 and g_2 with respect to local and global steps in the same notation as in Figure 2.9. Once the center position converges in the local process $\mathbf{P}_s$, the system switches to the tip-tilt process $\mathbf{P}_t$.

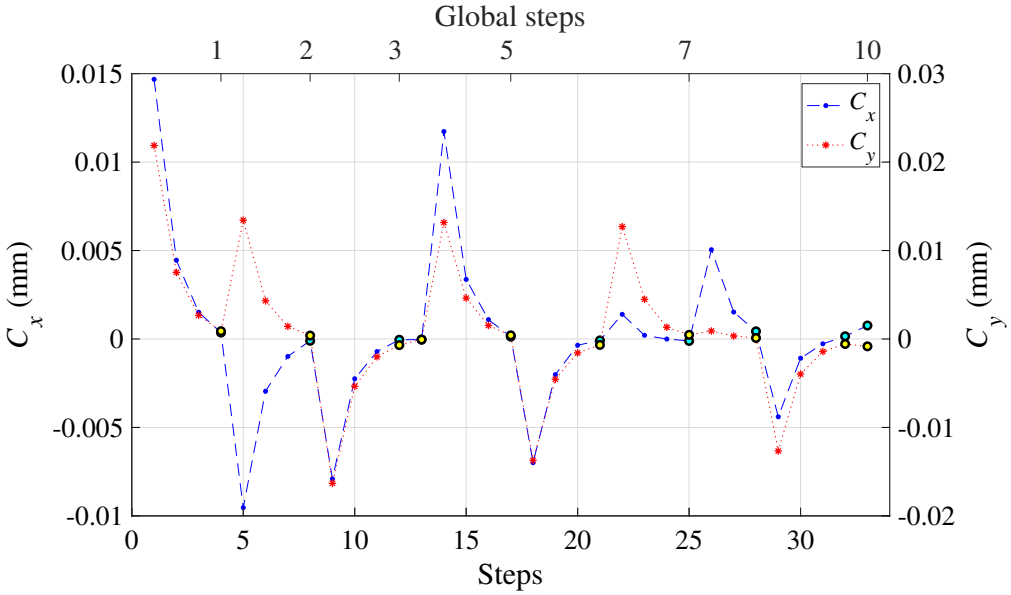

Figure 2.9: Measurement C_x and C_y in convergence test.

The tip-tilt process $\mathbf{P}_t$ begins at the first point in Figure 2.11. Figure 2.11 shows the tip-tilt stage value g_3 and the aspect ratio after updating g_3. When it reaches the first circle mark in the figure, the system steps into the first point in Figure 2.12, which shows the tip-tilt stage value g_4 and the aspect ratio after

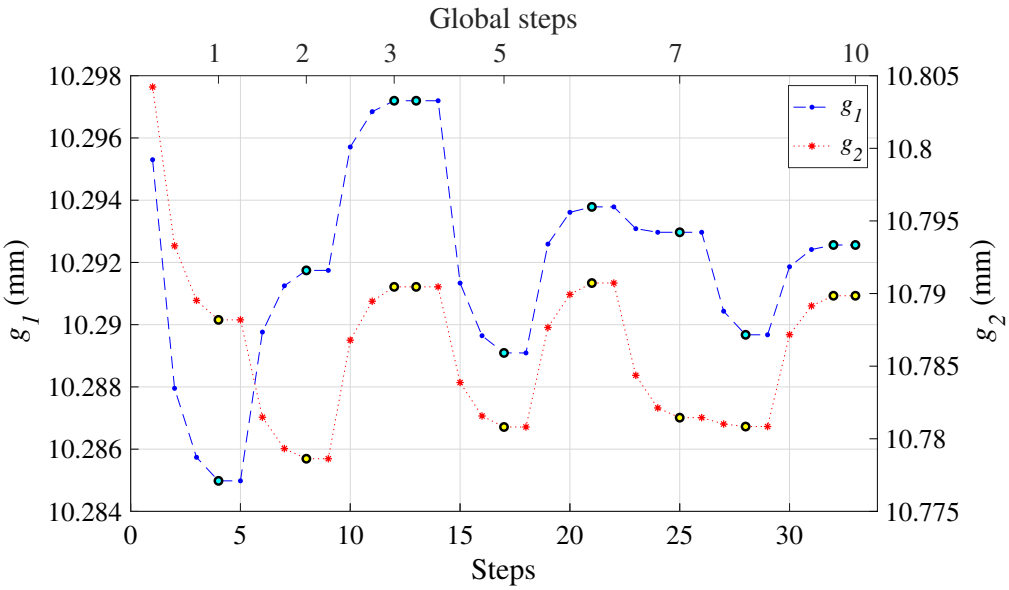

Figure 2.10: Stage command g_1 and g_2 in convergence test.

updating g_4. The first loop of external control process $\mathbf{P}_g$ is completed as the system reaches the first global step in Figure 2.12. We reset the boolean variables b_A, b_B, b_C, and b_D and start the second global loop. The points after the first circle in Figure 2.9 and 2.10 are the beginning of the second global loop. The global loop $\mathbf{P}_g$ keeps running until the system satisfies the global break condition (b_A, b_B, b_C, and b_D are all equal to 1), which occurs at the last circled point in Figure 2.12.

2.3 Discussion

In our control procedure, we define convergence in terms of thresholds on the differential measurements of the aspect ratio at two symmetric control points around the current system state ($\Delta\rho_3$ and $\Delta\rho_4$), but our real goal is to minimize the final aspect ratio of the beam spot. As shown in Figure 2.11 and 2.12, the

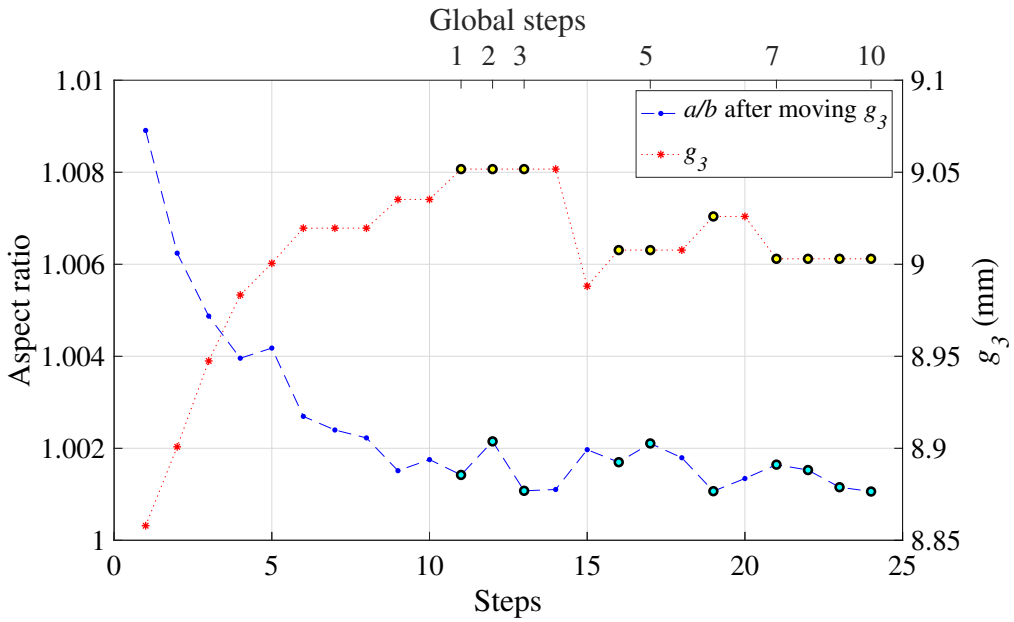

Figure 2.11: Aspect ratio and stage position g_3 after updating g_3 in $\mathbf{P}_t$.

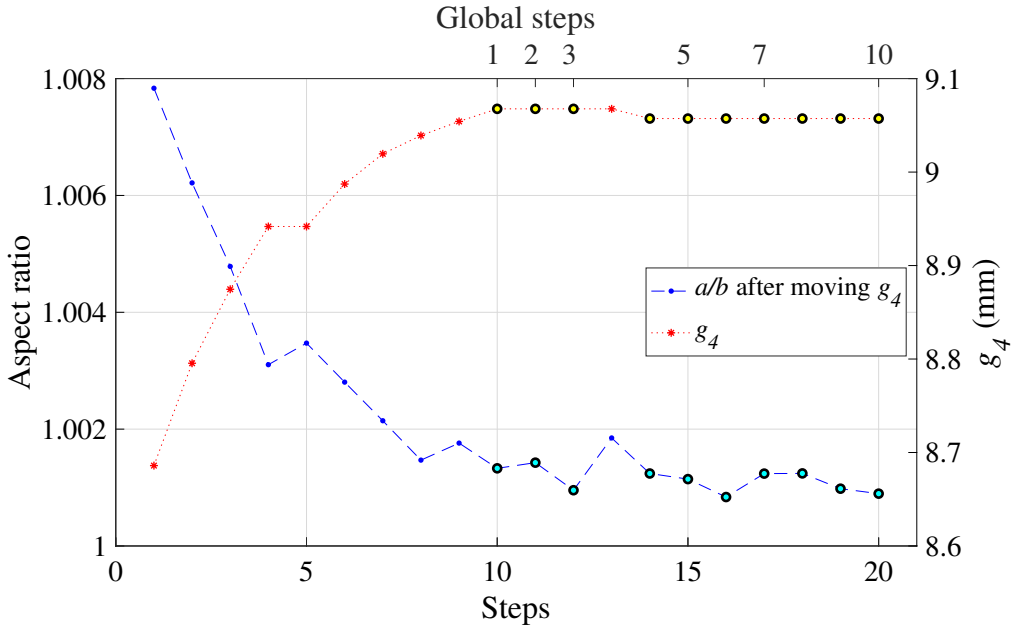

Figure 2.12: Aspect ratio and stage position g_4 after updating g_4 in $\mathbf{P}_t$.

aspect ratio converges to approximately 1.001 in 10 global steps. There are multiple possible reasons that cause the remaining steady-state error. Instrumental limitations, including the finite pixel size and dynamic range of the camera and the limited precision in tip-tilt and translation stages, will bound the accuracy of our measurements. At the same time, camera dark and read noise, instability in the laser beam, and various thermal effects degrade the image quality and thus the precision of the measurement. Finally, the center of the subframe used in the measurement may not be the exact center of the beam path. In this case, we may end up calibrating the tip-tilt misalignments of the system under a non-axisymmetric condition.

In terms of instrument limitations, the stationary precision test of the spot center in Figure 2.8(a) is approximately 1 *micron*. It is a reasonable value (1/5 of the pixel size) for a camera with pixel size 4.54 *micron*. We are more interested in the effect of tip-tilt stage precision on the convergence test. In Figure 2.11 and 2.12, the last four points in the tip-tilt process $\mathbf{P}_t$ have measurements below the threshold β_t at the first measurement, but the global step is not terminated. This indicates that the center of the Gaussian spot is shifted to a value greater than the threshold β_s when moving the tip-tilt stage. This observation agrees with the kinematic precision test shown in Figure 2.8(a). The shift process $\mathbf{P}_s$ cannot get the measurement below the threshold at the first measurement, and so the boolean b_A is set to zero. The global loop continues until the effect of moving tip-tilt stage does not shift the center of Gaussian spot above the threshold. The system will reach global convergence in fewer iterations if the tip-tilt stage has a higher precision.

To minimize the effects of camera dark current, we subtract an average dark

frame (made from doing pixel-by-pixel averaging on a set of dark frames) from all images prior to doing any calculations. While this improves the dark noise characteristic, it does not mitigate the camera read noise, which remains as a potential major noise source in photon-limited cases. However, as our laser intensity is tuned to produce measurements with count rates at the center of the beam spot towards the maximum of the linear range of our camera, we believe that read noise does not make a significant contribution to the measurement error in the experiment described here. We also observe some thermal effect when performing a precision test measurements over long time intervals. However, our closed loop control operates on much shorter time scales, and so is able to consistently calibrate the system misalignments.

In our optical model, we assumed that the beam path intersects with the CCD at the center of the image frame. With this assumption we can claim that the aspect ratio with respect to t_x and t_y when s_x and s_y are zero (as shown in Figure 2.1.2) is axisymmetric. In our physical system, we assume that the intersection of the beam and the CCD is very close to the center of the frame, so that any non-axisymmetric effects are negligible. Of course, if the intersection actually occurs far away from the center of the image frame, we might constantly shift the lens to some misaligned s_x and s_y, and t_x and t_y will not be able to converge to a local minimum since our assumptions for using $\Delta\rho_3$ and $\Delta\rho_4$ as feedback measurements will not hold. The local minimum can be obtained by using the aspect ratio itself as the measurement instead of $\Delta\rho_3$ and $\Delta\rho_4$, but the trade off is the relatively measurement noise close to any minimum. For the cases when the intersection might be far away from the center of the grabbed frame, an algorithm finding the global minimum of the 4-dimensional space s_x, s_y, t_x, and t_y is needed. Instead of converging C_x and C_y to zero, we should con-

verge them to some initially unknown values which can be learned by fitting the aspect ratio in the 4-dimensional space.

In this chapter we develop a fundamental control method to align an optical component using low order feature detection. However, the detected features chosen are based on the observation of a deformed Gaussian spot, instead of directly decomposed from the misaligned images. The misalignments of the optical components will case some specific aberration modes at the image plane. These modes can be found by decomposing an image dataset collected at different misaligned positions. In the next chapter we discuss how to use singular value decomposition (SVD) to find the focal plane modes directly related to the misalignments in the system. Moreover, the control algorithm developed in this chapter is a decision based algorithm. This control method does not model the full system nor take into account the disturbance and noise. In the next chapter we use stochastic filtering techniques which address these problems in the estimation.

CHAPTER 3

AUTOMATED ALIGNMENT OF OPTICAL SYSTEMS USING FOCAL-PLANE SENSING AND KALMAN FILTERING

3.1 Introduction

In Section 1.1 and 1.2 we discuss existing wavefront sensing and optical alignment methods. These methods generally require additional sensors, such as Shack-Hartmann wavefront sensor. In this chapter we propose a method which corrects the misalignment of an optical systems using existing camera in the system. A new sensing and control method for aligning a reconfigurable optical system is presented. We demonstrate the ability to align a two lens system using only a focal plane camera.

An optical model of a monochromatic beam, two moving lenses, and a science camera is connected to a closed-loop control system. We implement an iterated extended Kalman filter (IEKF) and unscented Kalman filter (UKF) to estimate the states in the control process. Our current alignment methodology is focused on narrow field of view (FOV) systems and focuses on the on-axis signal. However, the basic approach can be extended to also consider off-axis sources and be made relevant for systems with larger FOVs. Examples of small FOV systems currently in use include light detection and ranging (LiDAR) systems for detail local mapping [56], high contrast imaging system for imaging exoplanets near bright stars [57], and high resolution satellites [58, 59].

In Section 3.2, we define the reconfigurable optical model and control scheme. In Section 3.3 we discuss the methods used in modeling and estima-

tion, including Karhunen-Loève modal reconstruction, model fitting, and state estimation. We present the simulation result and introduce the experimental setup. In Section 3.4, the experimental result is presented. Both image reconstruction and closed-loop state estimation are shown. The importance of the observability and stability are discussed in Section 3.5. We extend the unknown states in the system and analysis the nonlinear observability and error bounds in the simulation. Finally, we apply the method on a reflective optical system with a misaligned off-axis parabolic mirror. The simulation and experimental result presented in Section 3.6.

3.2 Reconfigurable Optical Model

Figure 3.1 shows a two lens optical system. The two moving lenses are represented as gray ellipses, the collimated laser beam is represented by the red line along the z-axis, the x-y plane is normal to the beam path, and the x-axis is along the vertical. The collimated Gaussian beam passes through two moving lenses A and B, and is focused on a CCD camera. The focal lengths of lens A and B are set as 200 and 100 mm, respectively, the image plane has pixel size 4.54 μm, and the laser beam has wavelength 635 nm. The distance between the collimated laser beam and lens A is 50 mm, and the distance between lens A and lens B is 400 mm. The CCD camera is placed at a distance of 212 mm after lens B. Our goal is to calibrate the moving lenses, which have a total of 8 degrees of freedom - shift in x and y direction, tip and tilt for each lens. This is a simple model where the despace misalignments of both lens A and B are assumed to have smaller influence on the system compared with lateral motions, and the shift along the z axis of both lenses are not included in the model. A column

vector $\boldsymbol{x} = [s_x^A, s_y^A, s_x^B, s_y^B, t_x^A, t_y^A, t_x^B, t_y^B]^T$ is used to describe the state of our system.

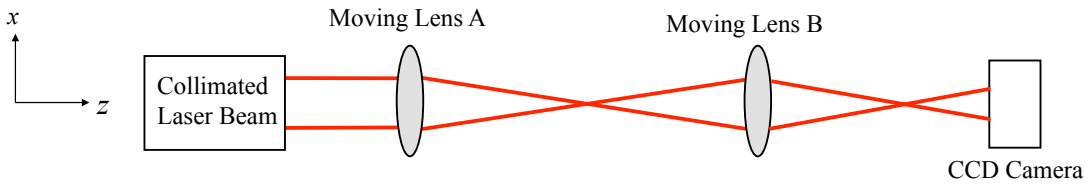

Figure 3.1: Two lens optical system. A collimated Gaussian beam is passed through two moving lenses A and B, and focuses on a CCD camera.

Figure 3.2 shows a schematic of the self-algining control system. The optical model in Figure 3.1 is in the upper dashed block (Plant), and the lower dashed block represents a Kalman filter in closed-loop control system. The images captured from the camera are projected onto Karhunen-Loève (KL) modes obtained from principal component analysis (PCA), which will be discussed in the next section, with the corresponding KL weights serving as the measurements of the control system. The measurements are sent to the Kalman filter to compare with the measurement predicted from our measurement model function (section 3.3.3). The state estimate predicted by the Kalman filter is fed back to correct the misalignment (section 3.3.4).

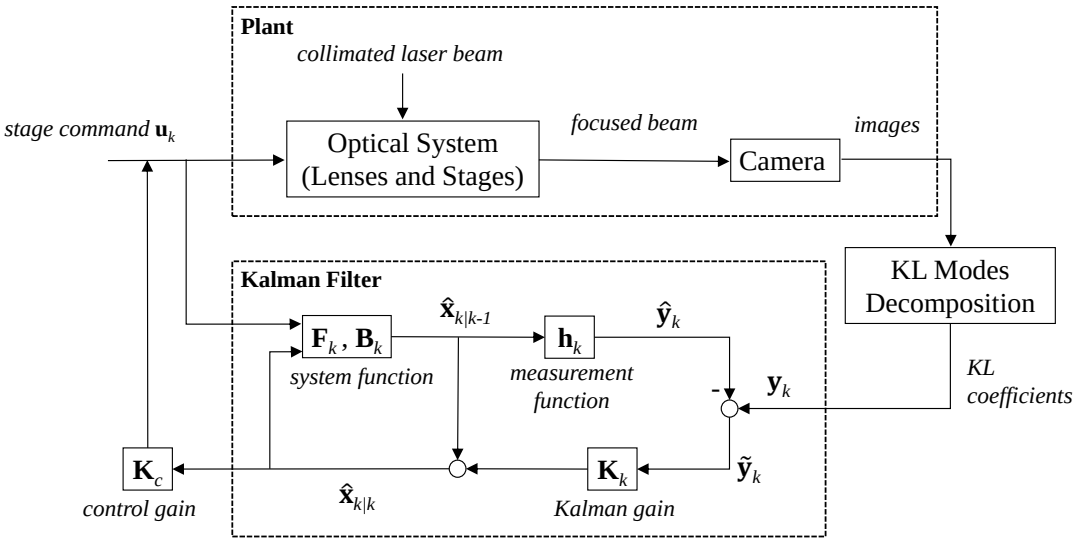

Figure 3.2: Schematic of control system. Upper dashed block represents the optical system in Figure 3.1, and lower dashed block represents a Kalman filter.

3.3 Methodology

3.3.1 Image Processing

We simulate images given misalignment parameters using ZEMAX software (shown in Figure 3.3). The prescription in ZEMAX is set as the optical system described in Section 3.2. Thorlabs lens LB1945 and LB1676 are imported as lens A and lens B, respectively. The laser, lenses, and camera parameters are chosen to model the conditions in the experiment as shown in Table 3.5.

Misalignment of the lenses introduces wavefront aberrations into the optical system, resulting in motion and shape changes to the nominally axisymmetric Gaussian spot in focal plane images. Figure 3.4 shows a sample misalgined

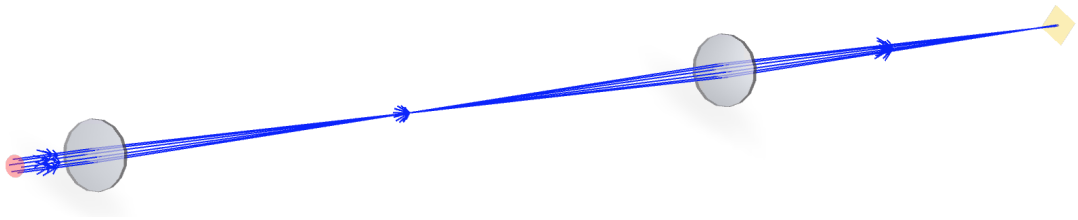

Figure 3.3: 3D model of the two lenses in ZEMAX.

image in 250×250 pixels. Our first image processing step is to fit a 2D Gaussian to the image to obtain the center position of the Gaussian spot of the image, and then perform PCA to decompose the image dataset into KL modes.

Figure 3.4 shows the Gaussian fitting of the simulated image in contour plot. The Gaussian center C_x and C_y can be obtained and will be used as our measurements.

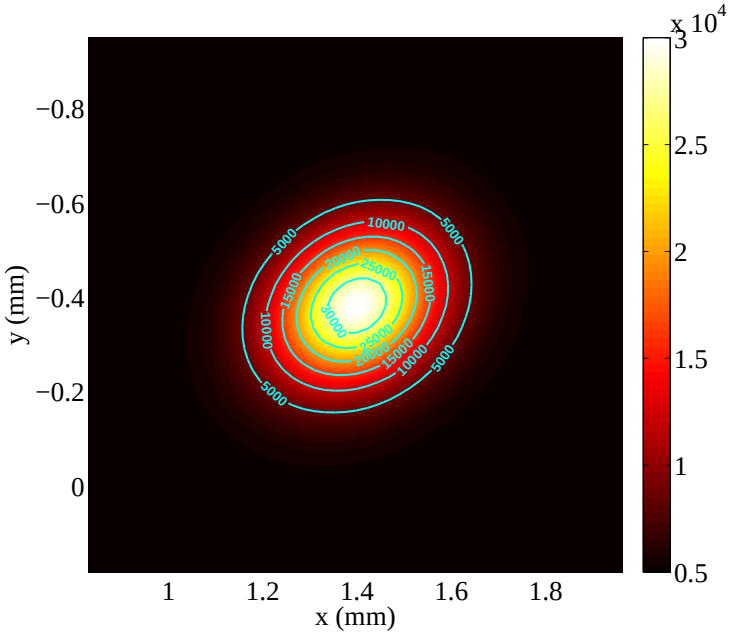

Figure 3.4: Subframe of the simulated image from Zemax and its 2D Gaussian fitting in contour plot.

3.3.2 Principle Component Analysis and Image Decomposition

We perform a PCA using the Karhunen-Loève Transform (KLT) to create an orthogonal basis of eigenimages [54, 60]. KLT method decomposes observed signals into a combination of linearly independent modes called principal components. The observed signals are the image data set we collected from ZEMAX. In this section we call the linearly independent modes KL modes.

We collect the image dataset by scanning through eight state variables s_x^A, s_y^A, s_x^B, s_y^B, t_x^A, t_y^A, t_x^B, and t_y^B. Each state is perturbed with 3 misaligned values $-\delta$, 0, and δ, where δ is a small misalignment for each state. We perturb the shift and tip-tilt by 0.4 *mm* and 4 *degree* respectively. The collected images include all combinations of the perturbation on the states. This results in a total of 3^8 scanned images. We capture a fixed size subframe ($N_p \times N_p$) around the Gaussian center C_x and C_y. The subframe image matrix is reshaped into a p-element column vector $\boldsymbol{v}_i$, where $p = N_p^2$ and i indicates the image number. We use the vector-mean-subtracted value of the image vector

$$\bar{\boldsymbol{v}}_i = \boldsymbol{v}_i - \mu(\boldsymbol{v}_i)\,, \tag{3.1}$$

where $\mu(\cdot)$ is a mean operator. A large matrix containing all the scanned data can be obtained as

$$\bar{\boldsymbol{V}} = [\bar{\boldsymbol{v}}_1, \bar{\boldsymbol{v}}_2, ..., \bar{\boldsymbol{v}}_n]\,. \tag{3.2}$$

The image-to-image covariance matrix of the scanned data set is given by

$$\boldsymbol{S} = \frac{1}{p-1}\bar{\boldsymbol{V}}^T\bar{\boldsymbol{V}}\,, \tag{3.3}$$

where $\boldsymbol{S}$ is an $n \times n$ matrix. We perform an eigendecomposition of covariance $\boldsymbol{S}$ and obtain matrices $\boldsymbol{\Phi}$ and $\boldsymbol{\Lambda}$ such that

$$\boldsymbol{S}\boldsymbol{\Phi} = \boldsymbol{\Phi}\boldsymbol{\Lambda}\,, \tag{3.4}$$

where $\mathbf{\Phi}$ is an $n \times n$ matrix whose columns are the eigenvectors of $\boldsymbol{S}$, and $\mathbf{\Lambda}$ is an $n \times n$ diagonal matrix whose entries are the corresponding eigenvalues. The KL transform matrix is then

$$\boldsymbol{Z} = \bar{\boldsymbol{V}}\mathbf{\Phi}\,, \tag{3.5}$$

where $\boldsymbol{Z}$ is a $p \times n$ matrix whose columns are the KL modes.

Figure 3.5 shows the first 12 KL modes (in order of decreasing eigenvalue) and the corresponding eigenvalue in log scale. Each image has a frame size of 250×250 pixels, and all images are independently stretched to show details of the mode shapes.

The image $\bar{\boldsymbol{v}}_i$ can be reconstructed as a weighted sum of the first m KL modes with coefficients

$$\boldsymbol{w}_i = \boldsymbol{Z}_m^{\dagger}\bar{\boldsymbol{v}}_i\,, \tag{3.6}$$

where $(\cdot)^{\dagger}$ is the pseudoinverse of a matrix, and $\boldsymbol{Z}_m$ contains the first m KL modes. The reconstructed image $\bar{\boldsymbol{c}}_i$ can be calculated as

$$\bar{\boldsymbol{c}}_i = \boldsymbol{Z}_m\boldsymbol{w}_i\,, \tag{3.7}$$

where $\boldsymbol{w}_i$ is an m-element column vector of the coefficients calculated above. Figure 3.6(a) shows the reconstructed image $\bar{\boldsymbol{c}}_i$ of the simulated image in Figure 3.4 using the first six KL modes. The subtracted image in Figure 3.6(b) shows the difference $(\bar{\boldsymbol{v}}_i - \bar{\boldsymbol{c}}_i)$ between the simulated image in Figure 3.4 and the reconstructed image.

Figure 3.7 shows the reconstruction error using the first eight modes to reconstruct the image, with all of the images plotted on the same intensity scale. As expected, we can see that the reconstruction error decreases gradually as the number of mode used increases. The RMS pixel errors ϵ_i of the reconstruction

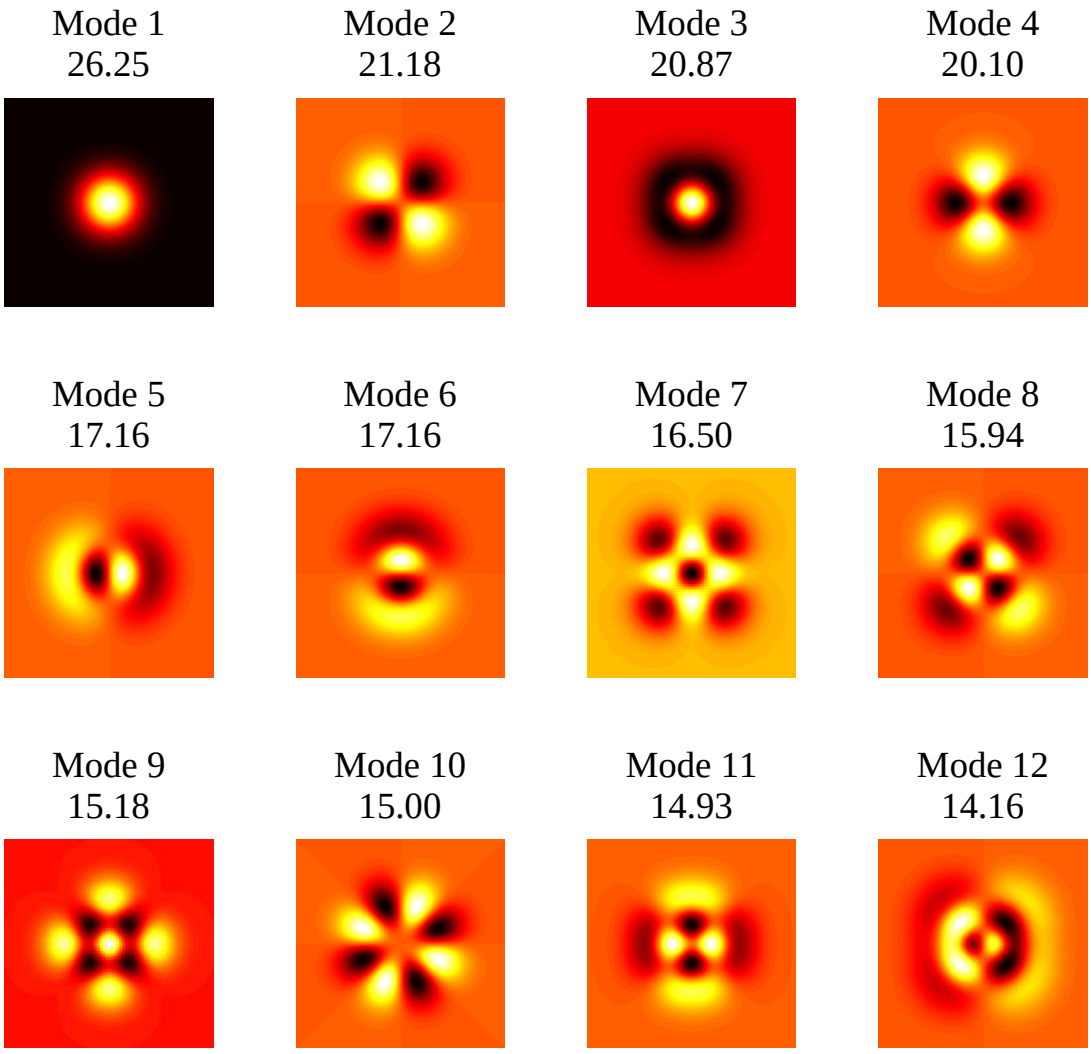

Figure 3.5: First 12 KL modes obtained from PCA decomposition with subframe 250×250 pixels. Each image is plotted under different intensity scale and its corresponding eigenvalue is shown under the mode number in log scale.

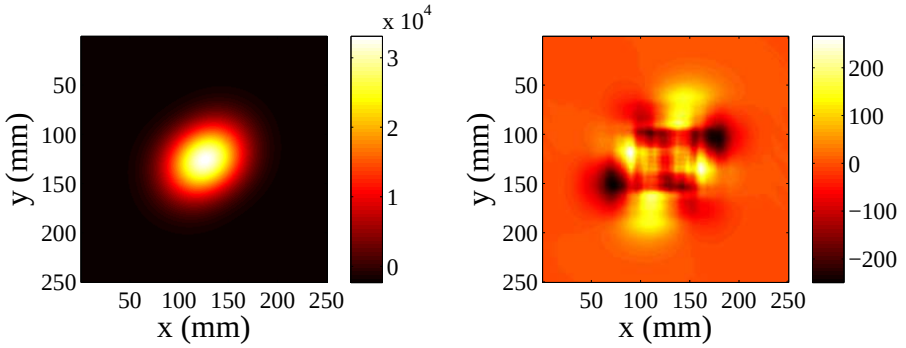

(a) (b)

Figure 3.6: Reconstruction of simulated image in Figure 3.4 using the first six KL modes.

of image i is defined as

$$\epsilon_i = \frac{\sqrt{(\bar{\boldsymbol{v}}_i - \bar{\boldsymbol{c}}_i)^T(\bar{\boldsymbol{v}}_i - \bar{\boldsymbol{c}}_i)}}{p}, \tag{3.8}$$

and is used as a metric for the quality of the image reconstruction. The blue circle markers in Figure 3.8 shows the RMS error ϵ_i after the frist 10 modes used. The RMS pixel error shown is the average over all of the training data.

3.3.3 Measurement Model Function

The weights of KL modes 2-6, normalized by mode 1, together with the Gaussian center C_x and C_y are used as the measurements. The measurement $\boldsymbol{y}$ can be written as

$$\boldsymbol{y} = [\frac{w_2}{w_1}, \frac{w_3}{w_1}, \frac{w_4}{w_1}, \frac{w_5}{w_1}, \frac{w_6}{w_1}, C_x, C_y]. \tag{3.9}$$

The simulated image set described in Section 3.3.2 was obtained by scanning through the eight system states and generating 6,561 images for the KL mode decomposition. Now, we generate 60,000 images given random misaligned

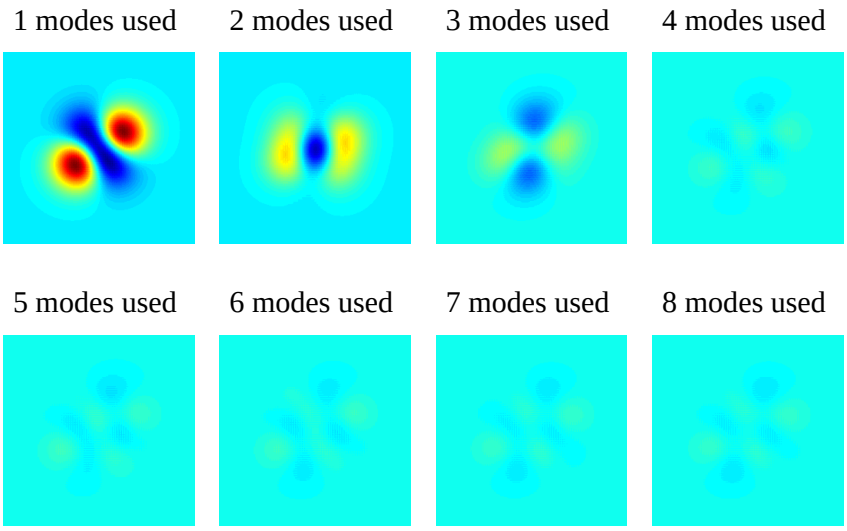

Figure 3.7: Residual error with modes 1 - 8 used in image reconstruction. The reconstruction error decreases gradually as the number of modes used increases.

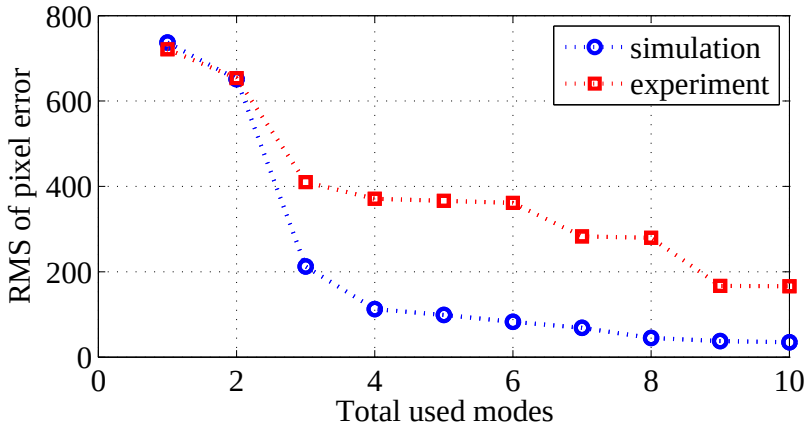

Figure 3.8: Reconstruction RMS pixel error using the first 10 modes.

Table 3.1: NRMSE of measurement y_1 to y_7. Both training and test error are computed to ensure the model is not overfitted.

NRMSE (‰)	y_1	y_2	y_3	y_4	y_5	y_6	y_7
Training set	3.26	5.51	4.05	3.97	4.18	1.05	1.06
Test set	3.27	5.54	4.10	4.07	4.27	1.05	1.06

states to train the measurement function. Two thirds of these images (40,000) are used as our training set, and the remaining one third (20,000) as the test set.

We perform a nonlinear least squares fitting on the training set using the Levenberg-Marquardt algorithm [61]. The nonlinear measurement model function $\boldsymbol{h}$ is learned to predict measurement $\boldsymbol{y}$, computed as $\hat{\boldsymbol{y}} = \boldsymbol{h}(\boldsymbol{x})$. Each nonlinear function h_j is a second order polynomial which maps the misaligned state $\boldsymbol{x}$ to predict measurement $\hat{\boldsymbol{y}}$, where j is the number of measurement from 1 to 7. The error between the simulated and predicted measurements is $\boldsymbol{e} = \hat{\boldsymbol{y}} - \boldsymbol{y}$, and the NRMSE are calculated to ensure the model does not suffer from overfitting.

$$\text{NRMSE}(e_j) = \frac{\sqrt{(\sum_{i=1}^{n} e_{j,i})/n}}{\max y_j - \min y_j}. \tag{3.10}$$

where i ranges from 1 to n for n points in the dataset. Table 3.4 shows the NRMSE of the prediction on measurement 1 to 7. The NRMSE are calculated to ensure the model does not suffer from overfitting.

We plot the histogram of error $\boldsymbol{e}$ as shown in Figure 3.9. The blue and red lines are the best-fit normal distribution functions of the error distributions. The more Gaussian the distribution of the error, the better our measurement model performs in Kalman filtering. The error covariance matrix $\boldsymbol{R}_{model}$ is calculated as

$$\boldsymbol{R}_{model} = \boldsymbol{e}\boldsymbol{e}^T, \tag{3.11}$$

and used as part of the measurement covariance matrix in Kalman filtering.

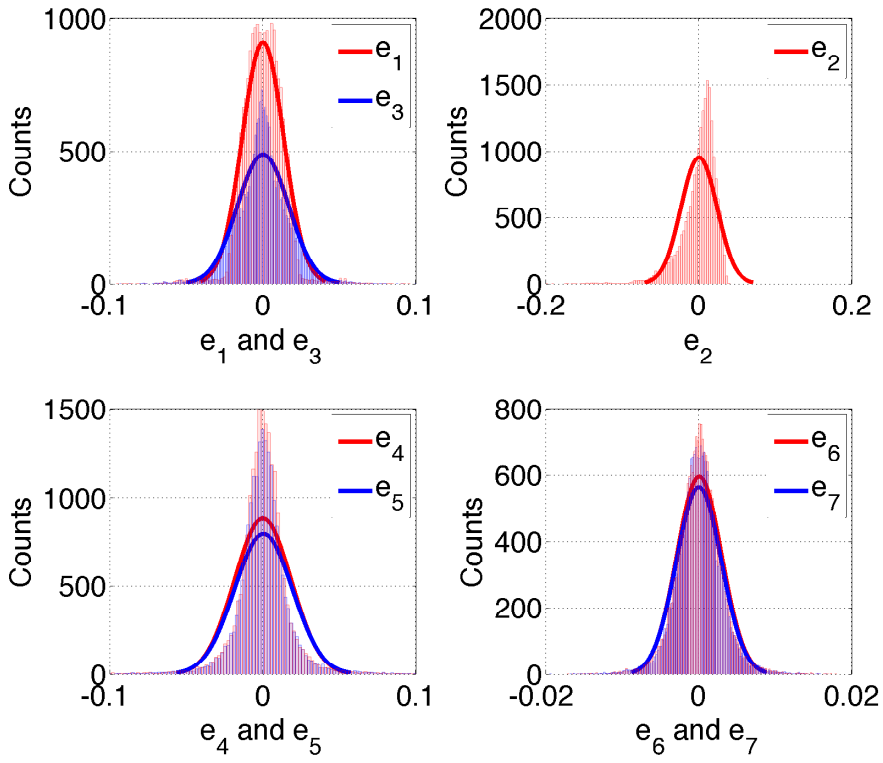

Figure 3.9: Histogram of the residual e_1 to e_7 and their best fitted normal distribution.

3.3.4 State Estimation and Control

Kalman Filtering

Our state space representation is

$$\begin{aligned} \boldsymbol{x}_k &= \boldsymbol{F}_k \boldsymbol{x}_{k-1} + \boldsymbol{B}_k \boldsymbol{u}_k + \boldsymbol{q}_k \\ \boldsymbol{y}_k &= \boldsymbol{g}_k(\boldsymbol{x}_k) + \boldsymbol{r}_k \,, \end{aligned} \tag{3.12}$$

where the state transition matrix $\boldsymbol{F}_k$ and the control input matrix $\boldsymbol{B}_k$ are taken to be identity matrices. The process noise $\boldsymbol{q}_k$ is a zero mean Gaussian with covariance $\boldsymbol{Q}_k$, $\boldsymbol{q}_k \sim N(0, \boldsymbol{Q}_k)$. The observation function $\boldsymbol{g}_k$ maps the misaligned states $\boldsymbol{x}_k$ to the measurement $\boldsymbol{y}_k$, and $\boldsymbol{r}_k \sim N(0, \boldsymbol{R}_k)$ is the measurement noise. The

observation function is modeled by nonlinear measurement function $\boldsymbol{h}$ learned in section 3.3.3.

An iterated extended Kalman filter (IEKF) is used to estimate the misaligned states. Extended Kalman filter (EKF) is an nonlinear version of Kalman filter which approximates the mean and covariance of the current estimate using local linearization of the nonlinear function. IEKF is a modified version of EKF which takes multiple Gauss-Newton steps during each iteration[62]. The IEKF algorithm is shown in Algorithm 1. The parameter i_{max} is set to 100 steps and $\alpha_{min} = 1 \times 10^{-8}$.

Since our state transition ($\boldsymbol{F}_k$, $\boldsymbol{B}_k$) is linear, the nonlinear approximation only occurs in the measurement update step where we calculate the Jacobian of nonlinear function $\boldsymbol{h}$. UKF is also a nonlinear Kalman filter which uses unscented transform to estimate Gaussian distribution. The mean and covariance of state estimates are approximated by sigma points generated in the algorithm. The general process of Kalman filtering is shown as the lower dashed block in Figure 3.2.

Simulation result

We generate process noise with covariance $\boldsymbol{Q}_k$ and measurement noise with covariance $\boldsymbol{R}_{meas}$ in the simulation. The processing noise is generated to model the stages in the experiment and has standard deviation

$$\sigma_{process} = [0.005, 0.005, 0.005, 0.005, 0.04, 0.04, 0.04, 0.04]^T.$$

The measurement noise $\boldsymbol{R}_{meas}$ is estimated by collecting many stationary images at multiple position in the experiment, and has standard deviation

$$\sigma_{measurement} = [0.0029, 0.0082, 0.0050, 0.0219, 0.0354, 0.00025, 0.00026]^T.$$

The total measurement noise covariance is $\boldsymbol{R}_k = \boldsymbol{R}_{model} + \boldsymbol{R}_{meas}$. The state estimate and estimate covariance in Kalman filtering are denoted as $\hat{\boldsymbol{x}}$ and $\hat{\boldsymbol{P}}$. We implement an IEKF and a UKF given initial guesses of the state estimate $\hat{\boldsymbol{x}}_0$ and state estimate covariance $\hat{\boldsymbol{P}}_0$.

Figure 3.10 shows the RMS state residual plot of IEKF and UKF given random control input in the simulation. The lines with blue diamond red circle markers represent the IEKF and UKF estimation, respectively. Both IEKF and UKF achieve approximately $6\mu m$ error in shift and 0.02 *degree* error in tip and tilt. The lines with green square and magenta cross markers show the state residuals with full state feedback ($\boldsymbol{u}_k = -\hat{\boldsymbol{x}}_{k-1}$) after the 25th step in the IEKF and UKF estimation. Instead of feeding back the state estimate as the control input, we collect information by giving random inputs away from the center in the beginning of the closed-loop process. The reason we need a random walk for our system is to produce phase diversity which is not available using a single focal plane image. The perturbation needs to be above a certain value to have diversity for us to track the state, and the number of perturbations needed depends on the initial guesses of the state estimate. The step at which we start feedback is decided by the state covariance obtained in IEKF or UKF. We start full state feedback after the state estimate covariance converges and remain stable for a few steps.

In the simulation we are showing one of the worst cases where the state residual decreases gradually. This indicates the initial misalignment is at a po-

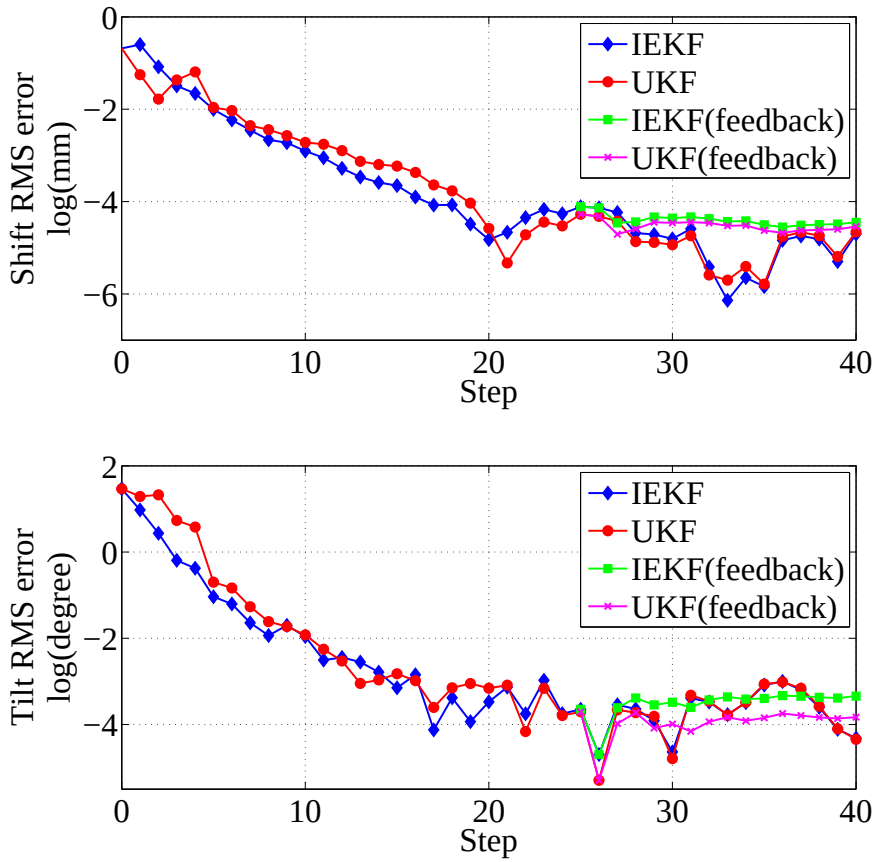

Figure 3.10: RMS state residuals of IEFK and UKF in the simulation.

sition from which our algorithm takes a long time to converges. In most of the cases the residual will drop down quickly in the first 2-10 steps. 25 steps were taken to get to a point where both our simulation and experiment have state covariance converging to a stable value, for presenting our results.

Figure 3.11 shows the RMS standard deviation of state estimation using IEFK and UKF in the simulation. The standard deviation is square root of each diagonal elements of the state estimate covariance matrix $\boldsymbol{P}_k$ in IEKF and UKF. The lines with blue diamond and red circle markers represent IEKF and UKF estimation, respectively. In the initial estimation-only phase, the uncertainty in the state estimate can be seen to decrease rapidly in the first few steps. When we

start feeding back the state estimate as a control input, the uncertainties become more stable as shown by the green square and magenta cross marked lines.

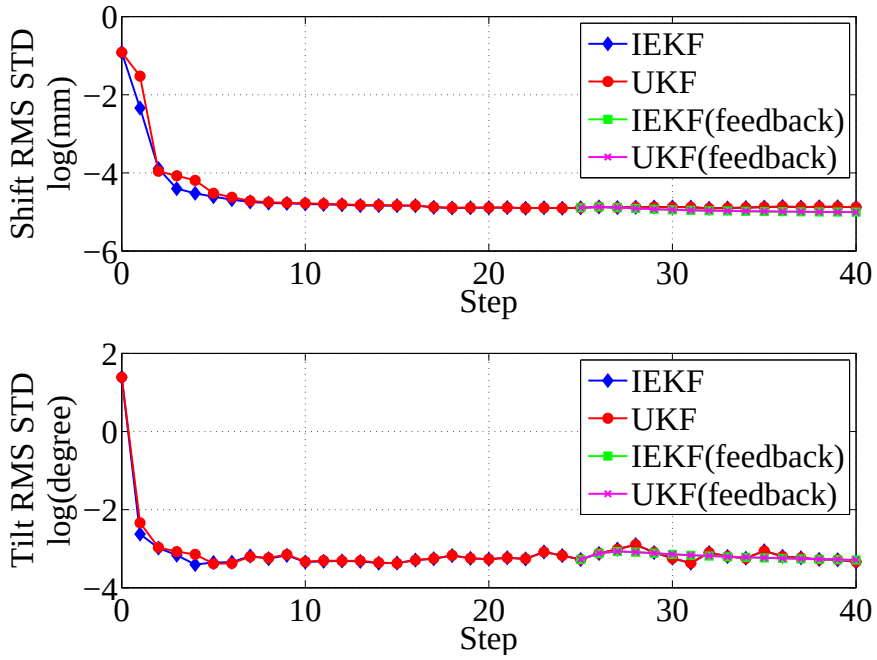

Figure 3.11: RMS standard deviation (STD) of state estimation using IEFK and UKF in the simulation.

3.4 Experiment

3.4.1 Setup

Figure 3.12 shows the experimental setup. The input 635 *nm* laser beam is passed through a customized collimator to produce a collimated beam as in the simulation. A neutral density (ND) filter is installed after the collimator to reduce the power of the laser beam. The moving lens A is placed after the ND filter, and the moving lens B is placed 400 *mm* after lens A. The CCD cam-

Table 3.2: List of components and devices in the experiment

Item	Model	Description
Collimator	TC25FC-633	Beam diameter ($1/e^2$): 4.67 *mm*
ND filter	NE50B-A	OD: 5.0
Lens A	LB1945-A	Focal length: 200 *mm*
Lens B	LB1676-A	Focal length: 100 *mm*

era is 212 *mm* away from lens B. Both lens A and B are mounted on motorized tip-tilt and translation stages. The stages and CCD camera are connected to a local computer which performs all data processing and can send actuation commands to the stages. The CCD camera, laser source, and stages are listed in Table 2.1. Table 3.5 shows the detailed information of the (Thorlabs) optical components in the experiment. The experimental results are presented in the next section.

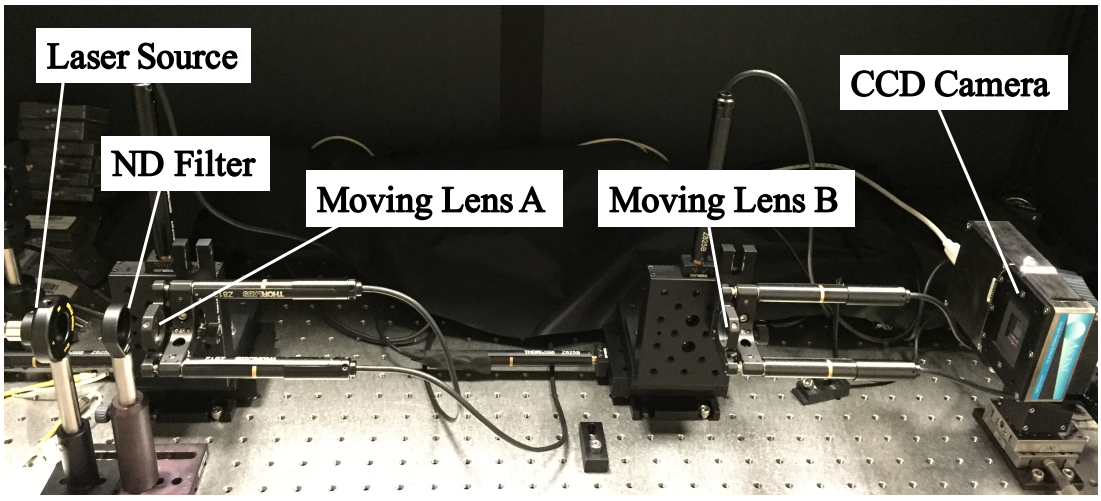

Figure 3.12: Experiment setup of optical model shown in Figure 3.1. A collimated laser beam passes through a ND filter, two moving lenses A and B, and focuses on a CCD camera.

3.4.2 Results

In this section we present the image reconstruction in the experiment and the result of closed-loop control with Kalman filtering.

Experiment Image Reconstruction

Figure 3.13 shows the residual error after reconstructing a single experimental image using the first eight KL modes derived in simulation. The corresponding sum of RMS pixel errors are shown as the red line with square markers in Figure 3.8. The sum of RMS errors shown is the average over 500 images with random state inputs collected in the experiment. The reconstruction error in the experiment has the same trend as a function of KL mode number as in the simulation. The higher pixel error in the experiment is caused by the additional noise sources in the system, such as variations in the laser source, imperfections in the optics, and undamped vibrations in the lens stages.

State Estimation Result

In the experiment we give random input to the stages for the first 25 iteration steps, and then feed back the full state estimate as the control input $\boldsymbol{u}_k = -\hat{\boldsymbol{x}}_{k-1}$ from step 26 through 50. The state residual cannot be obtained in the experiment since the true state is unknown. Figure 3.14 shows the stage position as a function of iteration using the IEKF. Stages 1-4 correspond to state elements $\boldsymbol{x}_1$ to $\boldsymbol{x}_4$, and stages 5-8 are the tip and tilt stages driven by translation motors. We decrease the process noise covariance matrix to $\boldsymbol{Q}_k/4$ from step 26 on as the noise should be relatively small when the motor is moving in a small range. The stage

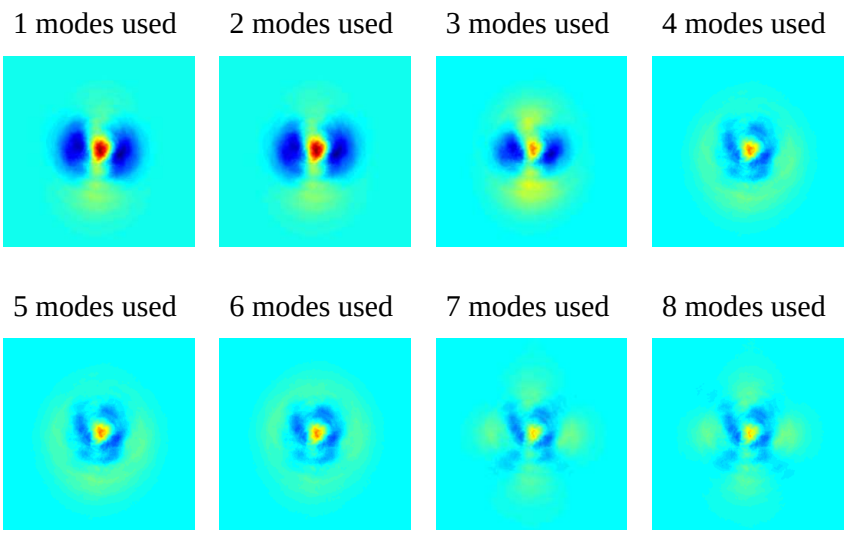

Figure 3.13: Residual error of the reconstruction of a single images acquired with the experimental setup shown in Figure 3.12.

positions converge to steady-state values as shown in Figure 3.14. The UKF experiment has similar results to the IEKF in terms of stage position.

Figure 3.15 shows the initial and final experimental images, before and after closed-loop control. The left image shows the subframe before the state feedback, and the right images is the subframe after the state feedback converges. As expected, the image shifts to the center and becomes significantly more axisymmetric after state feedback converges.

Figure 3.16 shows the RMS standard deviation of state estimation averaging over 20 executions of the closed loop experiment. The lines with blue diamond and red circle markers represent the IEKF and UKF estimation, respectively. Similar to the simulation, the uncertainly drops down rapidly in the first few steps. The STD of tilt estimate increases slightly when we start feeding back the state estimates, but drops down gradually after a few steps.

Although the stage positions converge to stable values in a single test, the

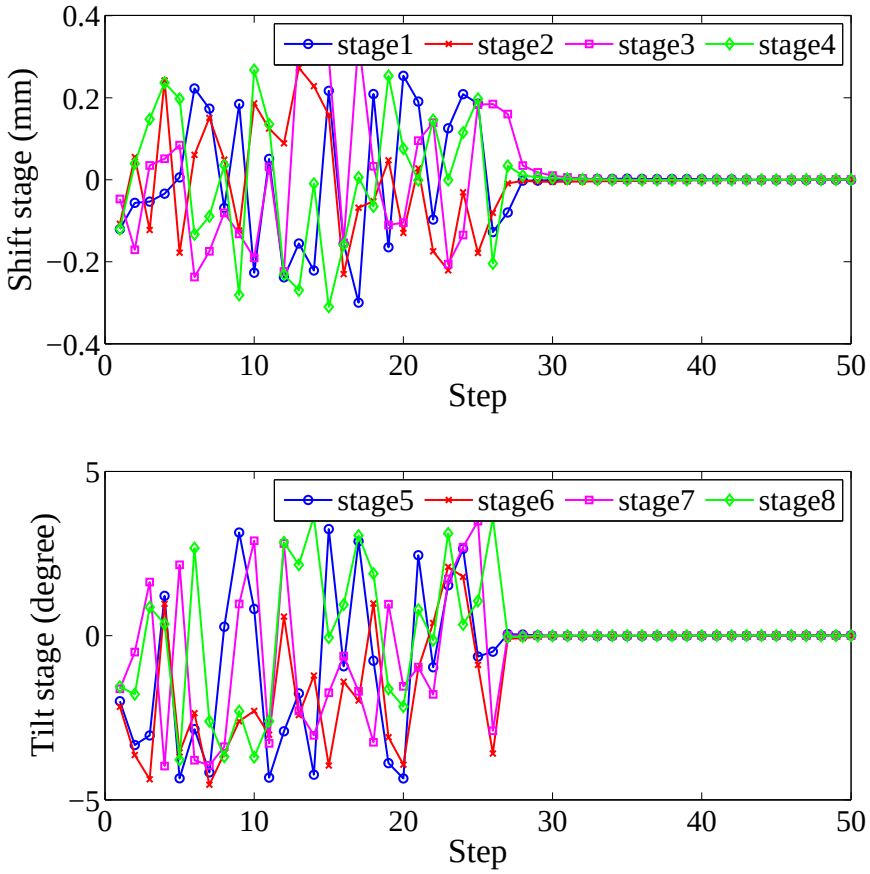

Figure 3.14: Stage positions from step 1 to 50 using IEKF. Stages 1-4 correspond to the shift stages, and stages 5-8 are the tip and tilt stages driven by translation motors.

final stable values vary somewhat between different runs. When the states are close to zero it is likely to converge to a local minimum where the shifts, tip, and tilt of the two lenses compensate with each other. Table 3.3 shows the standard deviation of stage convergence value in 20 tests. The variance of the final convergence values are of the same order. There is no evidence showing that UFK outperforms IEKF on our system, and vice versa. This indicates that the local linearization approximation in the IEKF is reasonable as UFK would capture the nonlinearity better than IEKF.

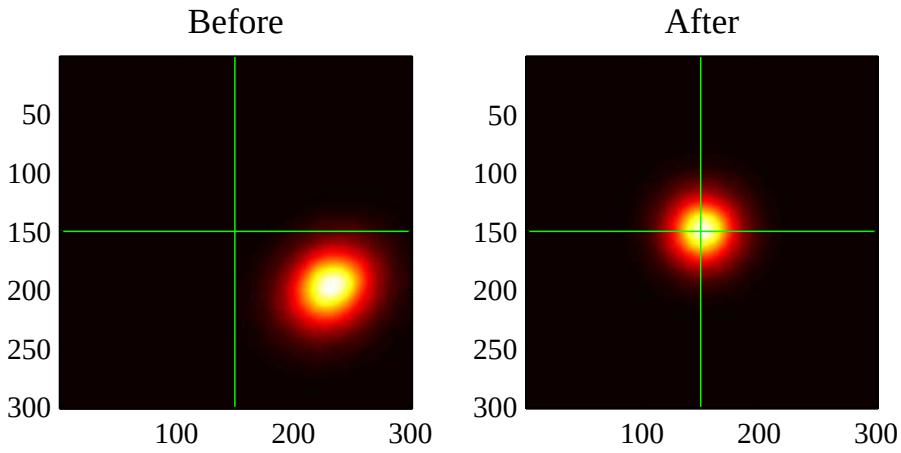

Figure 3.15: Experimental image before and after state feedback . The left image shows the 300×300 subframe before the correction, and the right image is the subframe after the correction. The intersection of the green lines represent the center of the camera.

Table 3.3: STD of stage convergence value in 20 runs. Both IEKF and UKF are presented.

	IEKF STD (mm)	UKF STD (mm)
stage 1	0.0345	0.0335
stage 2	0.0394	0.0454
stage 3	0.0360	0.0344
stage 4	0.0189	0.0232
stage 5	0.1342	0.1163
stage 6	0.1092	0.0845
stage 7	0.1067	0.1469
stage 8	0.0897	0.1071

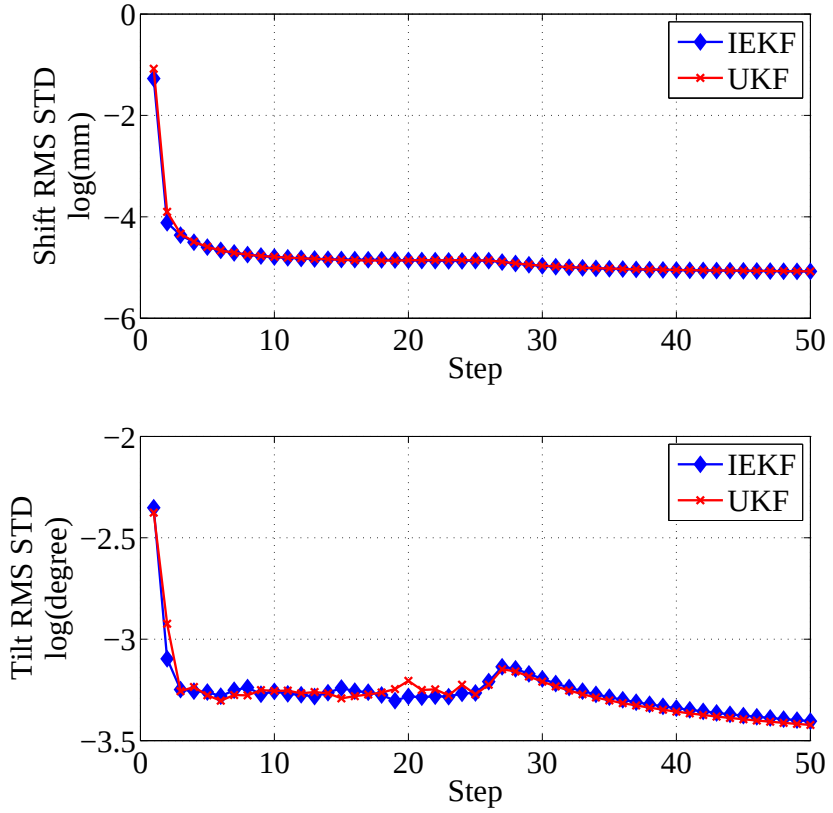

Figure 3.16: RMS standard deviation of state estimate averaging over 20 experiments.

3.4.3 Discussion

The automated alignment algorithm described here has two fundamental steps: 1. Image processing and reconstruction, and 2. State estimation and control. In the first step, the reconstruction error can be separated into the reconstruction bias and the detector noise. The bias is denoted as $(\bar{\boldsymbol{v}}_i - \bar{\boldsymbol{c}}_i)$ in section 3.3.2 and is neglected in the calculations for this step since it does not have a direct effect on the measurement error, and is considered as redundant information for correcting the system. In contrast, the noise in the image will be projected together with the image into the measurement $\boldsymbol{y}$ and becomes measurement noise $(\boldsymbol{R}_{meas})$

in the control and estimation step.

There are two additional error sources in the control and estimation step which are the modelling error and the process noise ($\boldsymbol{Q}_k$). The modelling error includes the measurement function fitting error ($\boldsymbol{R}_{model}$) and inconsistencies between the simulated optical system and the experimental setup. The inconsistencies can include both errors in component placement as well as unmodeled effects such as thermal drifts, and these effects cannot be corrected with the current implementation of Kalman filtering. The process noise ($\boldsymbol{Q}_k$) includes the actuator repeatability, backlash, and stage hysteresis, etc. The overall experiment error is a combination of all of these error sources. The uncertainty of these factors results in the variation of the final stage position shown in Table 3.3. The less sensitive our lenses are to misalignment, the greater the variation of the stage positions will be. Different local minima are found in various iterations in the experiment. The variation of the pixel value between these iterations has an average standard deviation ~ 24 in a 2^{16} dynamic range. The pixel with the highest STD (~ 600) occurs around the center of the each image.

Although z axis misalignments of lenses A and B are ignored in the current model, the despace parameter (z axis) is important in optical alignment. The component placement error might decrease if the z axis movement is included in state variables. The movement corresponds to focus motion, and will occur mostly on axisymmetric KL modes such as Mode 3 (similar to defocus). A nonlinear function mapping from the despace parameter to the weight of KL modes can be learned. We expect the misalignment can be calibrated using an IEKF as long as the modeled nonlinear function has good performance using the local linearization approximation. If the learned measurement model function

is highly nonlinear, we expect UKF will outperform IEKF, and should be used for state estimation. The misalignment of the focus motions will be included in future applications.

In simulation we have state residuals in multiple tests that show that the method is able to correct the misalignment to below a certain threshold. However, the method utilizes only an on-axis point source, and does not consider the alignment effects on optical aberrations across full FOV. Since many optical instruments use wide FOVs, a particularly important set of future tests will be to evaluate the effects of the variability of the final converged stage positions on off-axis point sources and images of extended sources. To the extent that this variability represents the insensitivity of the whole imaging system to this level of misalignments, we would expect similar results for on-axis and off-axis sources. However, if the different results actually represent truly different local minima where the lenses compensate for each others' misalignments in different ways, then we may expect different levels of distortion throughout the final image.

3.5 Observability and Stability

In this section we focus on the observability and stability analysis of our focal-plane sensing and estimation method. We discuss the sufficient conditions for error bounds, and the observability of a system with an underdetermined measurement function.

3.5.1 Boundedness of estimation error

Discrete-time nonlinear systems are described by the following equations, including a discrete time state transition function and a discrete measurement function

$$\boldsymbol{x}_{k+1} = \boldsymbol{f}_k(\boldsymbol{x}_k, \boldsymbol{u}_k) + \boldsymbol{G}_k \boldsymbol{w}_k \tag{3.13}$$

$$\boldsymbol{y}_k = \boldsymbol{h}_k(\boldsymbol{x}_k) + \boldsymbol{D}_k \boldsymbol{v}_k \tag{3.14}$$

Assumption: There are positive real numbers $\bar{a}$, $\bar{g}$, $\bar{c}$, $\bar{d}$, $\underline{p}$, $\bar{p}$, $\underline{q}$, $\bar{q}$, $\underline{r}$, $\bar{r} > 0$ such that

$$\|\boldsymbol{F}\| \leq \bar{a}, \quad \|\boldsymbol{G}\| \leq \bar{g}, \quad \|\boldsymbol{H}\| \leq \bar{c}, \quad \|\boldsymbol{D}\| \leq \bar{d} \tag{3.15}$$

$$\underline{p}\boldsymbol{I} \leq \boldsymbol{P}_{k+1|k} \tag{3.16}$$

Under the assumption, there are bounds $\epsilon_w > 0$ and $\epsilon_v > 0$ for the stochastic noise covariance matrices, i.e.,

$$\mathbb{E}\left[\boldsymbol{w}_k \boldsymbol{w}_k^T\right] \leq \epsilon_w^2 \mathbb{I} \tag{3.17}$$

$$\mathbb{E}\left[\boldsymbol{v}_k \boldsymbol{v}_k^T\right] \leq \epsilon_v^2 \mathbb{I}, \tag{3.18}$$

and a bound $\delta > 0$ for the initial estimation error, i.e.,

$$\mathbb{E}\left[\|\boldsymbol{e}_0\|^2\right] \leq \delta, \tag{3.19}$$

such that the estimation error $\boldsymbol{e}_k$ is exponentially bounded in mean square with probability 1.

3.5.2 Nonlinear Observability

For any admissible input sequence $(\boldsymbol{u}_0, \boldsymbol{u}_1, ..., \boldsymbol{u}_{k-1})$ and initial state $\boldsymbol{x_0}$, a discrete-time nonlinear system is observable if at $\boldsymbol{x}_0$ if the set of states indistinguishable

from $\boldsymbol{x}_0$ contains only $\boldsymbol{x}_0$ [63]. A nonlinear system is locally observable if $\boldsymbol{x}_0$ can be distinguished from its neighbors.

The local observability of a discrete nonlinear system can be evaluated using the following observability matrix [64]

$$\mathcal{O} = \begin{bmatrix} \dfrac{\partial \boldsymbol{h}}{\partial \boldsymbol{x}}(\boldsymbol{x}_k) \\ \dfrac{\partial \boldsymbol{h}}{\partial \boldsymbol{x}}(\boldsymbol{x}_{k+1})\dfrac{\partial \boldsymbol{f}}{\partial \boldsymbol{x}}(\boldsymbol{x}_k) \\ \vdots \\ \dfrac{\partial \boldsymbol{h}}{\partial \boldsymbol{x}}(\boldsymbol{x}_{k+n_m})\dfrac{\partial \boldsymbol{f}}{\partial \boldsymbol{x}}(\boldsymbol{x}_{k+n_m-1})\cdots\dfrac{\partial \boldsymbol{f}}{\partial \boldsymbol{x}}(\boldsymbol{x}_k) \end{bmatrix}, \tag{3.20}$$

where n_m and n_s is the number of measurements and states. The nonlinear system is weakly locally observable if matrix $\mathcal{O}$ is full rank. Nothing can be inferred about the observability if the rank condition is not satisfied. The observability matrix can be a function of the control input sequence $(\boldsymbol{u}_k, \boldsymbol{u}_{k+1}, ..., \boldsymbol{u}_{k+n_m-1})$. If the observability matrix is full rank and does not depend on the control input, this means the system is observable at any input. The control effort could force observability of unobservable dynamics.

3.5.3 Simulation

Here we extended the reconfigurable optical system in Section 3.2 to a 10 degrees of freedom model, where we introduce defocus misalignment for both lens A and B.

PCA decomposition

Figure 3.17 shows the KL modes from the decomposition in a 10 degrees of freedom system. The weight w_i and be obtained by projecting the image to mode m_i where $i \in \{0 \cdots 9\}$. Mode m_7 to m_9 are very likely to be dominated by noise, and consequently, we do not include weight w_7 to w_9 in the measurements. An extra mode obtained in the 10 degrees of freedom is the

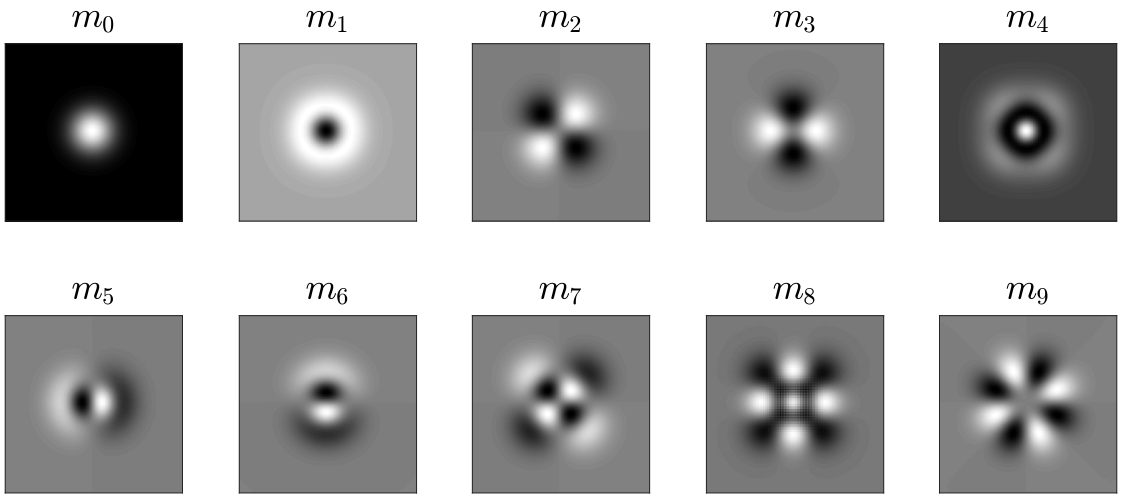

Figure 3.17: PCA decomposed modes in a 10 degrees of freedom system.

Training set visualization

We collect 5000 images with random 10 DOF misalignments in Zemax as our training set. Figure 3.18 show the visualization of the KL weights w_0 to w_6, and image center C_x and C_y. As shown in the figure most of the measurements have low correlation except for w_0, w_1, and w_4.

Figure 3.19 show the scatter plot matrix between the states and the measure-

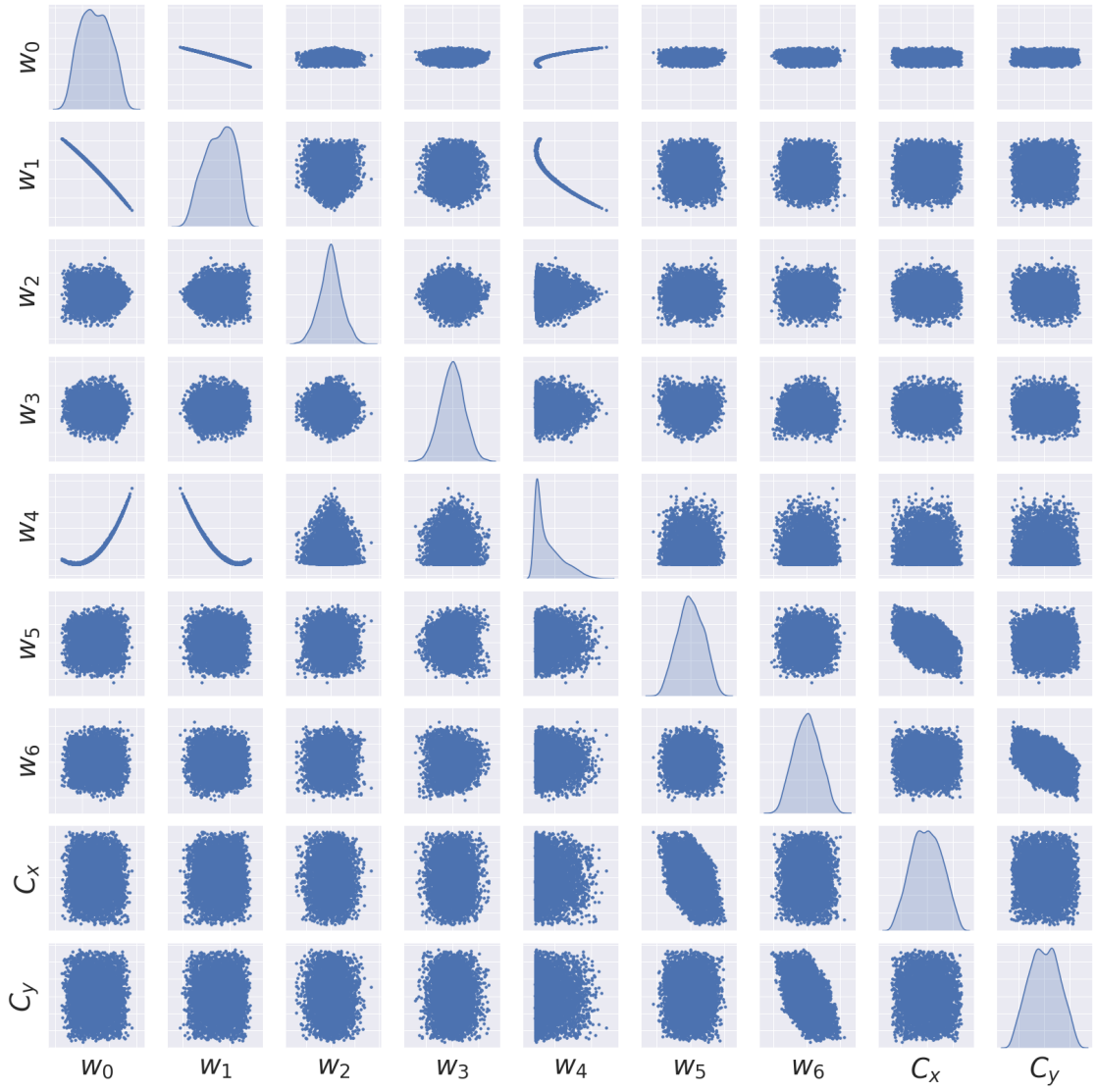

Figure 3.18: Autocorrelation of the measurement data in training set.

ments. The states in the figure are the decenters (s_x^A, s_y^A, s_x^B, s_y^B), tip-tilts (t_x^A, t_y^A, t_x^A, t_y^B), and defocus (d_z^A, d_z^B). Modes w_2 and w_3 are sensitive to tip and tilt misalignment since they are astigmatism related modes. Modes w_5 and w_6 are comma related modes which is sensitive to both decenter and tilt. The center positions C_x and C_y are sensitive to the decenter of the lenses. w_0, w_1, and w_4 are mainly affected by the defocus of the lenses.

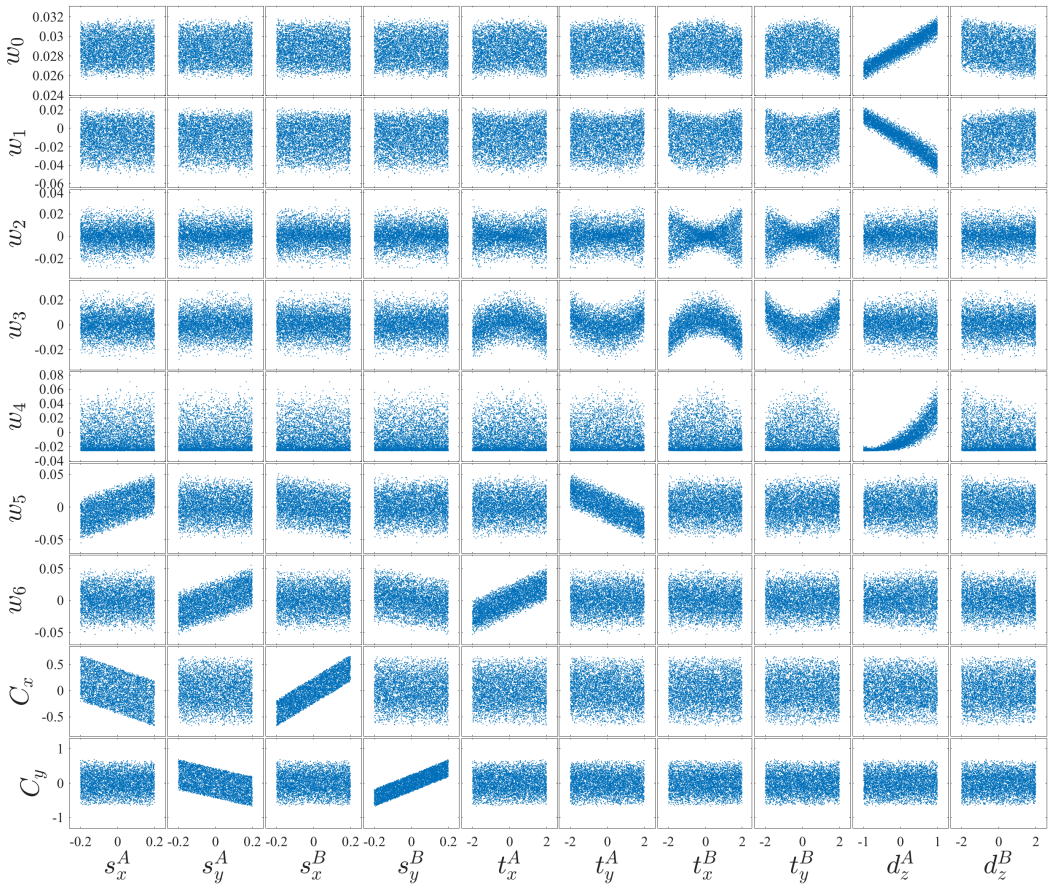

Figure 3.19: Scatter plot matrix between misalignment and measurement in training set.

Goodness of fit and error distribution

We use a multivariable polynomial regression (from 2 to 4 degree) to fit a model of measurement function $\boldsymbol{h}$. Figure 3.20 show the goodness of fit on a test with 2000 images. The result show R-squared values greater than 0.99. Figure 3.21 shows the error distribution of the test set. Since the model and shows low error in each measurement and close to normal distribution, we analysis the observability of the system based on the learned model and include the model error into measurement noise $\boldsymbol{v}_k$ in Equation 3.14.

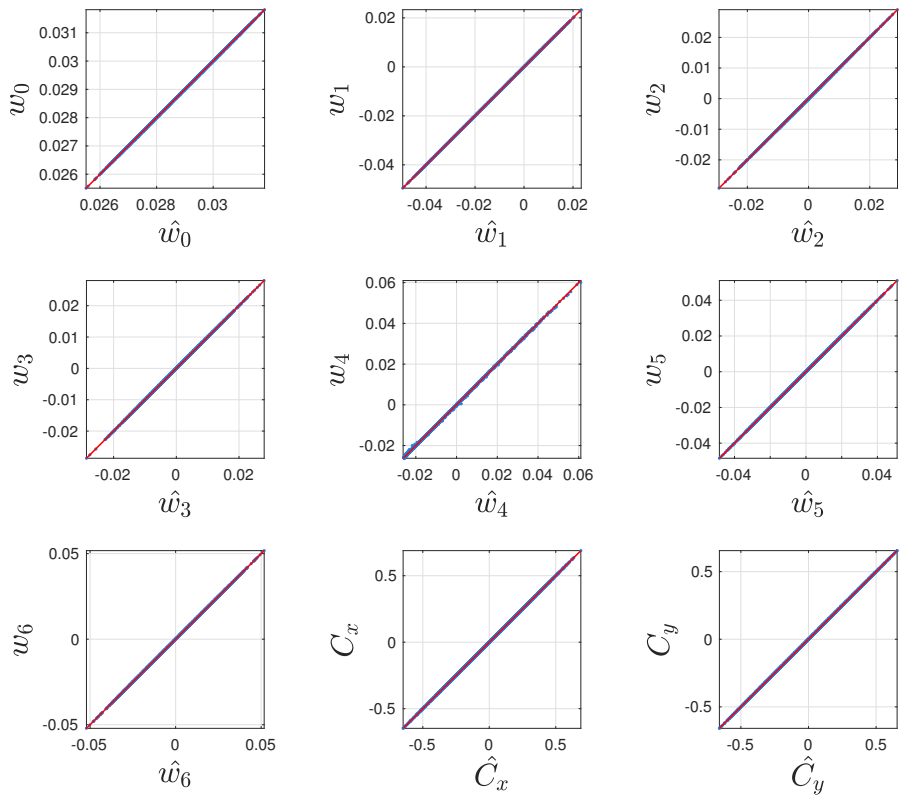

Figure 3.20: Goodness of fit of the measurement model on the test test.

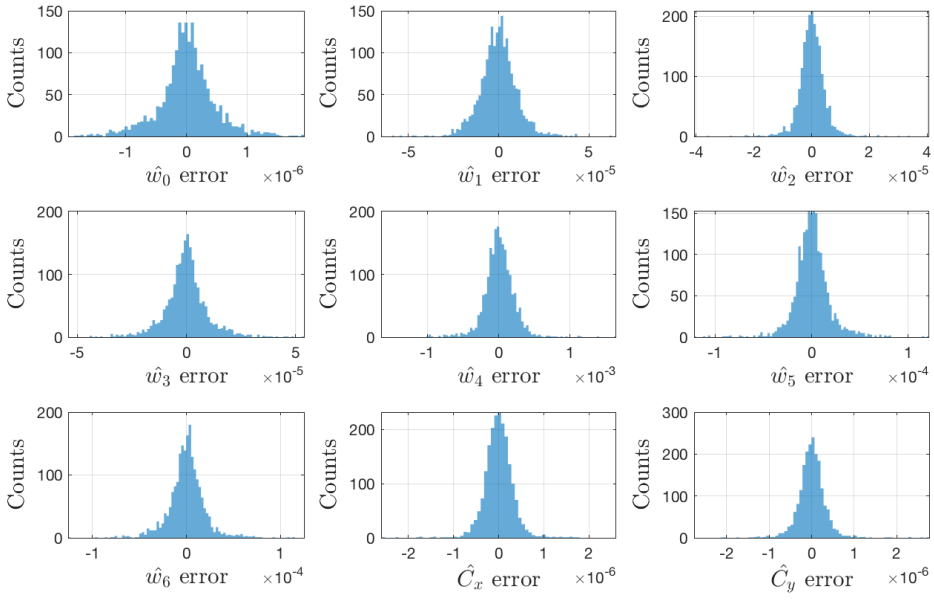

Figure 3.21: Error distribution of the test set

Control input driven observable system

We assume the state transition function is

$$\boldsymbol{f}_k(\boldsymbol{x}_k, \boldsymbol{u}_k) = \boldsymbol{I}x + \boldsymbol{u}_k, \tag{3.21}$$

where $\boldsymbol{I}$ is an identity matrix with size n_s and we have control over the change of the state. The proposed system is controllable and we focus on the observability analysis. We assume the polynomial model is sufficiently good and use it to determine the observability of the 10 degrees of freedom system. We plot w_0, w_1, and w_4 together in a 3D space since they show high correlation in Figure 3.18. As shown in the 3D plot Figure 3.22 the data points spread out on a polynomial line. This indicates that using all those modes as measurement does not improve the observability of our system.

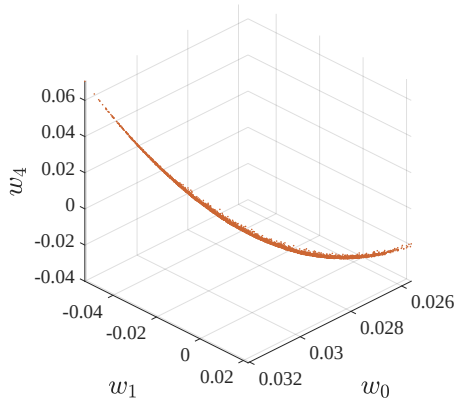

Figure 3.22: 3D visualization of measurements w_0, w_1, and w_4.

These three modes mostly affect the estimation of the defocuses d_z^A and d_z^B. Note that including w_1 and w_4 can improve the overall estimation if the noise is uncorrelated and the noise covariance matrix $\boldsymbol{R}_k$ in the estimation process properly weights each measurement. The improvement using all three modes under

the assumption will be shown later in the closed-loop simulation. One can also project these three measurements onto the principle plane in Figure 3.22 and use the projected component as the measurement. These different approaches will lead to the same system observability rank condition. To simplify the analysis we use the major modes w_0 as one of the measurements for the observability analysis and remove mode w_1 and w_4. As a result, we analyze a system with 7 measurements and 10 unknown states in the simulation.

To determinate the observability of the system we check the rank condition of the O matrix in Equation 3.20. Here we construct an $n_m n_s$ by n_s matrix O where $n_m = 7$ and $n_s = 10$. We say the system is locally weakly observable if the observability matrix $O \in \mathbb{R}^{70\times10}$ is full rank. Under the assumption of Equation 3.21 the Jacobian $\frac{\partial f}{\partial \boldsymbol{x}}$ in Equation 3.20 is the identity matrix $\boldsymbol{I}$. This indicates that we can only make the system observable by adding control inputs, which force $\boldsymbol{x}_k, \boldsymbol{x}_{k+1}, ..., \boldsymbol{x}_{k+n_m}$ in Equation 3.20 to have different values.

We can generate a random walk control input which force the observability matrix O to be full rank, and the rank condition can be check in the process. In fact, only two control input steps is needed to make $rank(O) = n_s$ since the matrix with the first two row $[\ \frac{\partial \boldsymbol{h}}{\partial \boldsymbol{x}}(\boldsymbol{x}_k) \quad \frac{\partial \boldsymbol{h}}{\partial \boldsymbol{x}}(\boldsymbol{x}_{k+1})\ ]^T$ is full rank when $\boldsymbol{x}_k$ and $\boldsymbol{x}_{k+1}$ have different non-zero values. However, checking the observability rank condition only gives us a yes or no answer instead of the degrees of observability and unobservability. Moreover, The rank condition of the observability matrix O may not yield a correct result if the when it is close to the singularity.

The calculation of the matrix condition number provides a more accurate measure of the observability [65]. We use the inverted formula of the condition

number $\zeta \in [0, 1]$

$$\zeta = \frac{\left|\lambda_{min}(O^T O)\right|}{|\lambda_{max}(O^T O)|}, \tag{3.22}$$

where $\lambda_{min}(\cdot)$ and $\lambda_{max}(\cdot)$ represent the minimum and maximum singular value of $O^T O$. $\zeta = 0$ means no observability and $\zeta = 1$ indicates full observability.

We compute the average the observability index of the random walk process at different ranges. The random walk value of the ith state is a uniform distribution $x_i \in [-\delta_i, \delta_i]$, where

$$\boldsymbol{\delta} = c_s \cdot [0.4, 0.4, 0.4, 0.4, 4, 4, 4, 4, 2, 4]^T . \tag{3.23}$$

c_s is the scale of the random walk. δ_1 to δ_4, δ_9 and δ_{10} are in the unit of millimeter (mm), and δ_5 to δ_8 are tip-tilts in degree (°). Figure 3.23 show the relationship between the scale c_s and the observability index ζ. Each label in the figure is an average of 500 tests using Equation 3.22. The center red line indicates the median, and the top and bottom edges of the box are the 25th and 75th percentiles. The whiskers extend to 1.5 interquartile range (IQR) away from the edges of the box, and the data outside this range are consider outliers plotted individually using red dots. The result shows that the system is less observable when approaching zero misalignments. With 10 degrees of freedom we can get better estimation when the system is away from the perfect alignment position.

Closed-loop estimation

Our system meets the assumption in Section 3.5.1. In the closed-loop simulation the given initial error, process noises, and measurement noises satisfy the limits in Equation 3.17 to 3.19. Figure 3.24 shows the error of the decenter estimates with random walk at $c_s = 1$. The estimation error is at the order of 1-10 μm.

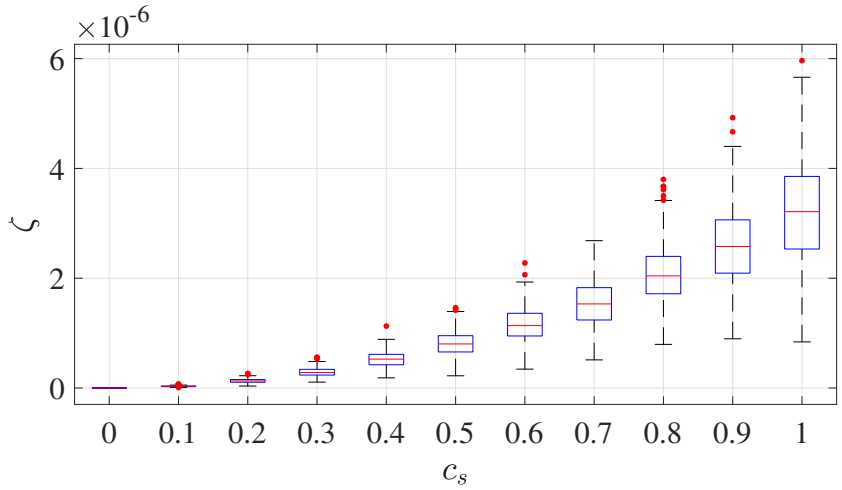

Figure 3.23: Observability index ζ at different random walk scales c_s.

Figure 3.25 shows the error of the tilt estimates of the same test, and the order of the estimation error is 0.01-0.1 degree. Both of these behave similar to the 8 degrees of freedom system.

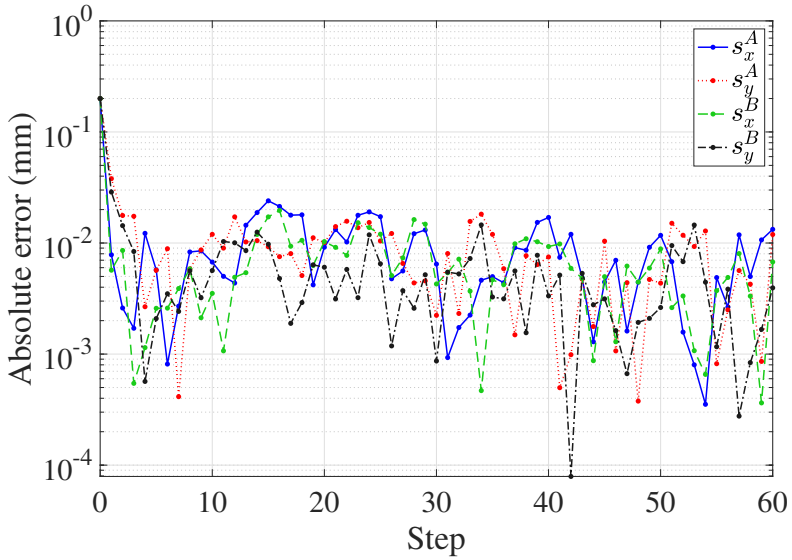

Figure 3.24: Absolute error of decenter estimates in the simulation.

Figure 3.26 shows the extra defocus degrees of freedom in this simulation. Here we simulate with both $n_m = 7$ and $n_m = 9$. As mention in the previous

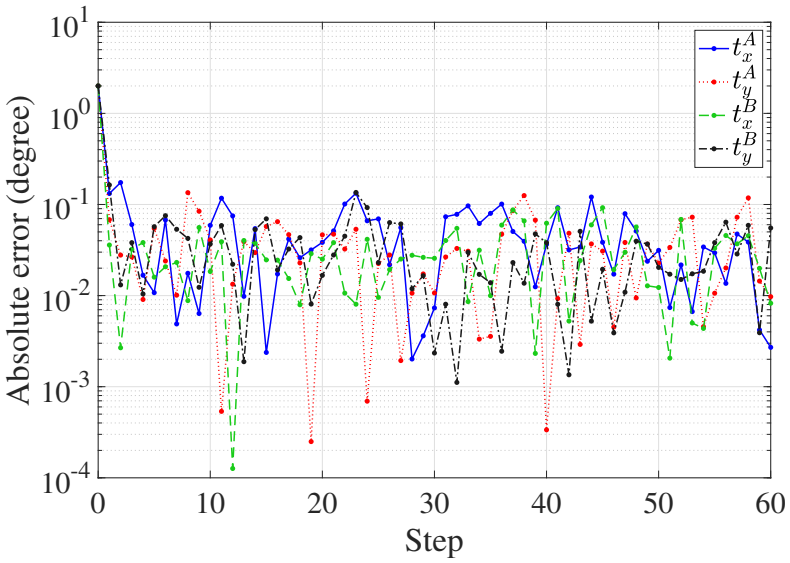

Figure 3.25: Absolute error of tilt estimates in the simulation.

section, adding more measurement can improve the overall estimation if the noise is uncorrelated and the noise covariance matrix $\boldsymbol{R}_k$ is properly selected. We can see in Figure 3.26 that both d_z^A and d_z^B have smaller error when all 9 measurements are used.

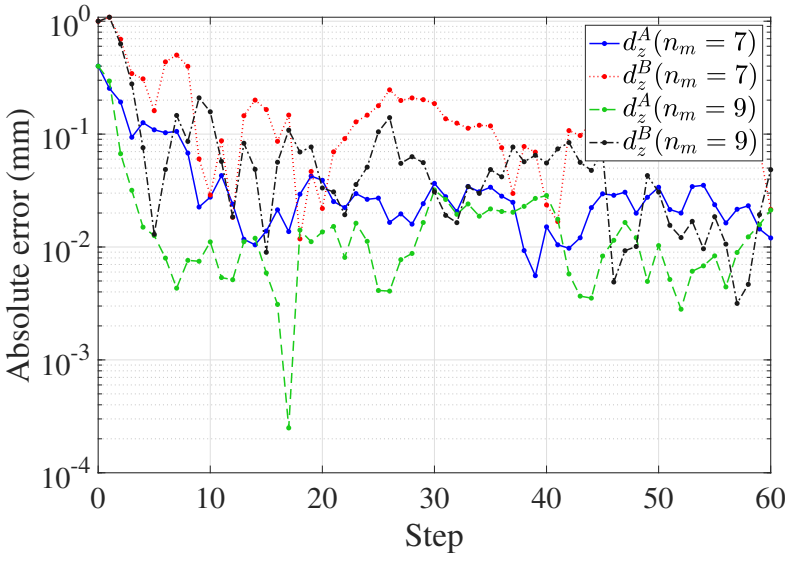

Figure 3.26: Absolute error of defocus estimates in the simulation.

After obtaining the state estimate $\hat{\boldsymbol{x}}_k$ at each step, we compute the control input $\boldsymbol{u}_k = -\boldsymbol{L}\boldsymbol{x}_k$, where $\boldsymbol{L}$ is the optimal gain matrix. $\boldsymbol{L}$ is chosen to minimize the cost function of the discrete-time LQR [47]. The cost function can be written as

$$J = \sum_{k=1}^{\infty} x_k^T \bar{Q} x_k + u_k^T \bar{R} u_k, \tag{3.24}$$

where $\bar{Q}$ is the weighted matrix of the states, and $\bar{R}$ is the weighted matrix of the control input. The $\bar{Q}$ is chosen to be five times larger than $\bar{R}$ since the range of our control input does not cause actuator saturation. The computed optimal gain $\boldsymbol{L}$ is a time-invariant diagonal matrix.

Figure 3.27 and Figure 3.28 shows the RMSE of decenter and tilt estimates with and without LQR feedback in the simulation. This is simulated under the assumption that the variance of process noises remain the same regardless the magnitude of the control inputs. The residual starts increasing when the feedback correction is initiated. This is because the observability index decrease when the misalignments approaches zeros, and the process noise accumulated over time. Figure 3.29 show the defocus residual which does not diverge when the feedback starts. This is because the defocus related measurements is non-symmetric around zero misalignments and it results in observable defocus states. Figure 3.30 shows the state estimate error covariance of the filter process. Similar to the state residuals, the uncertainly of the decenters and tilts increases when the feedback correction starts.

We assume that the process noise variances scale with the magnitude of the control input. Under this assumption the state residuals will not diverge during the feedback correction as shown in Figure 3.31 and Figure 3.32. Figure 3.33 shows that defocus states behave similar to the previous case. Figure 3.34 shows

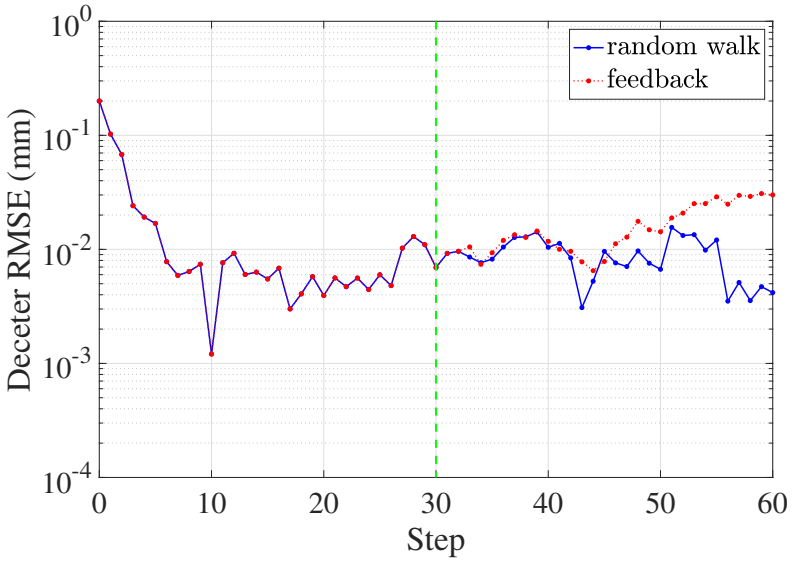

Figure 3.27: RMSE of decenter estimates with and without LQR feedback in the simulation.

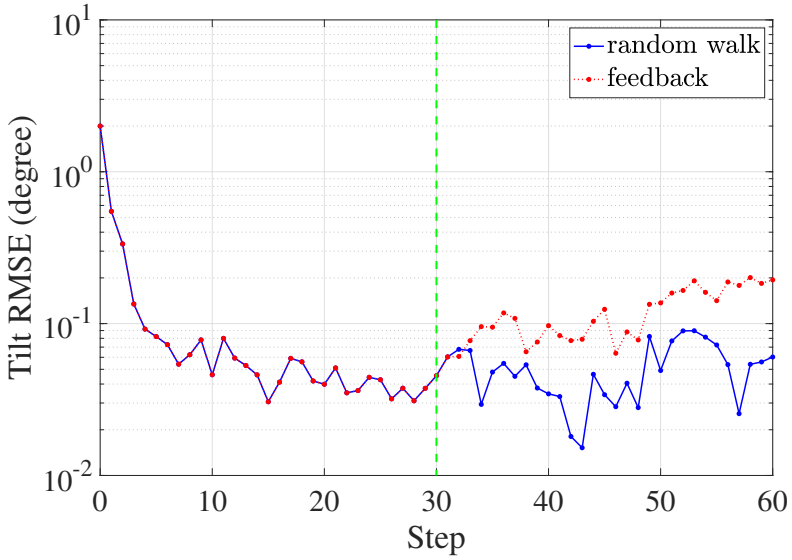

Figure 3.28: RMSE of tilt estimates with and without LQR feedback in the simulation.

that the error covariances are stable under the assumption. Figure 3.35 shows the true misalignment status of each state from a few steps before the feedback to the end of the process. The states starts converging to zero misalignments when the feedback correction starts, and remain stable after the correction.

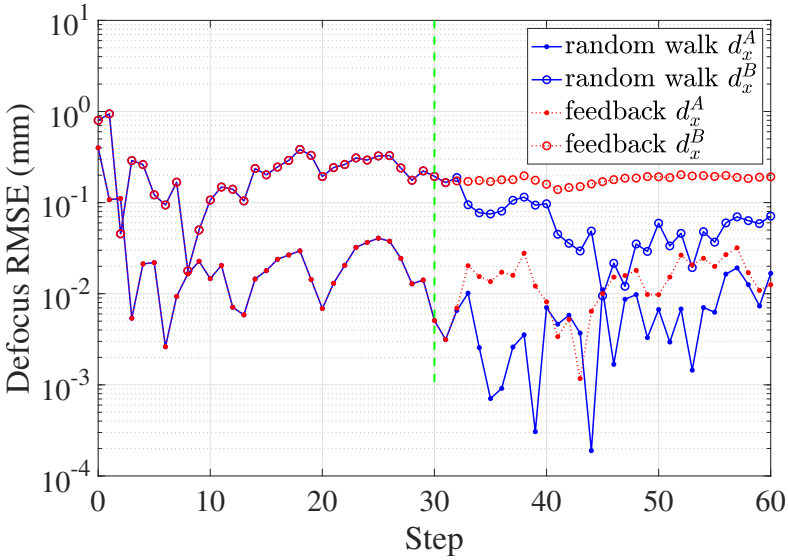

Figure 3.29: RMSE of defocus estimates with and without LQR feedback in the simulation.

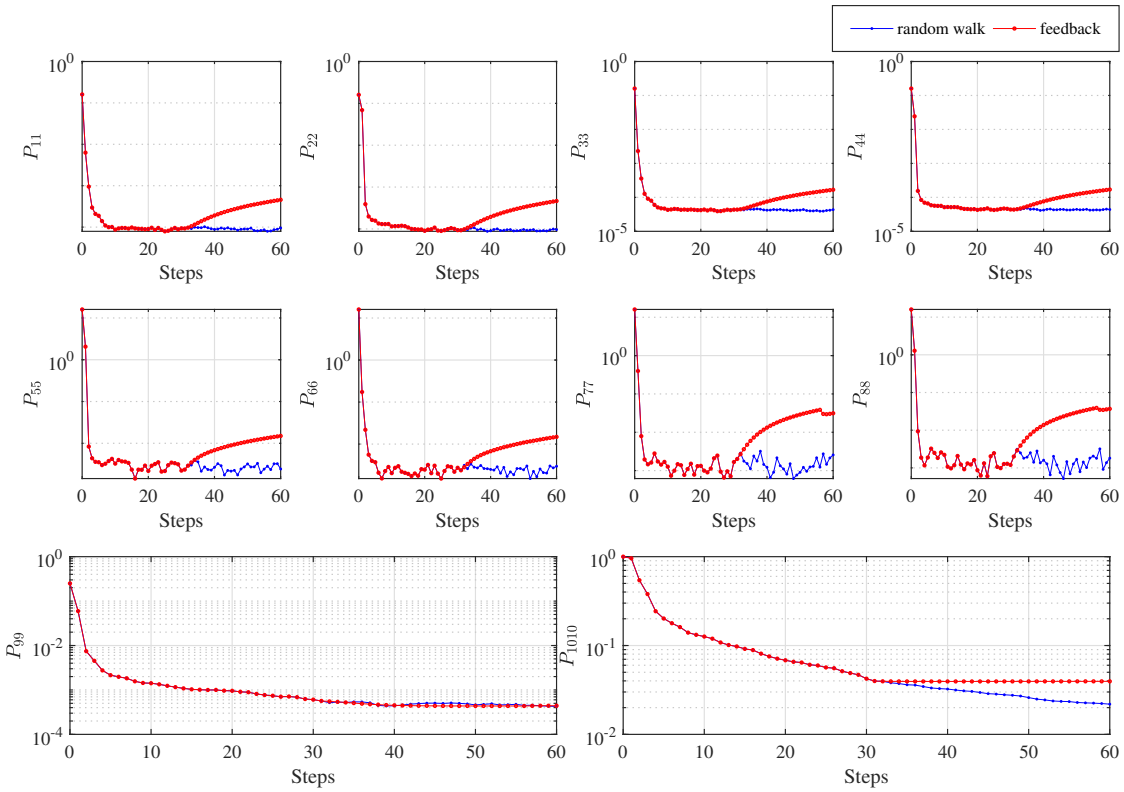

Figure 3.30: The diagonal component of the error covariance matrix in the simulation. P_{ii} represent the variance estimate of the ith state.

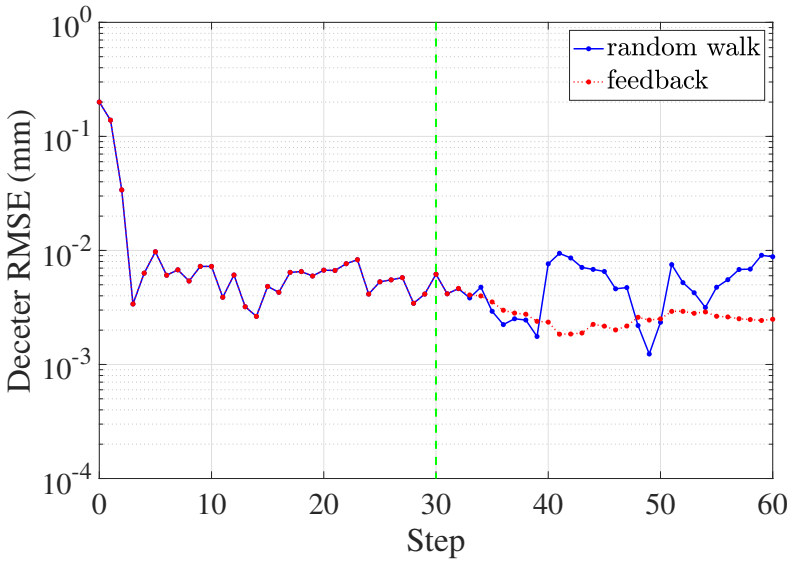

Figure 3.31: RMSE of decenter estimates with and without LQR feedback in the simulation. Assuming the process noise variance scales with the magnitude of the control input.

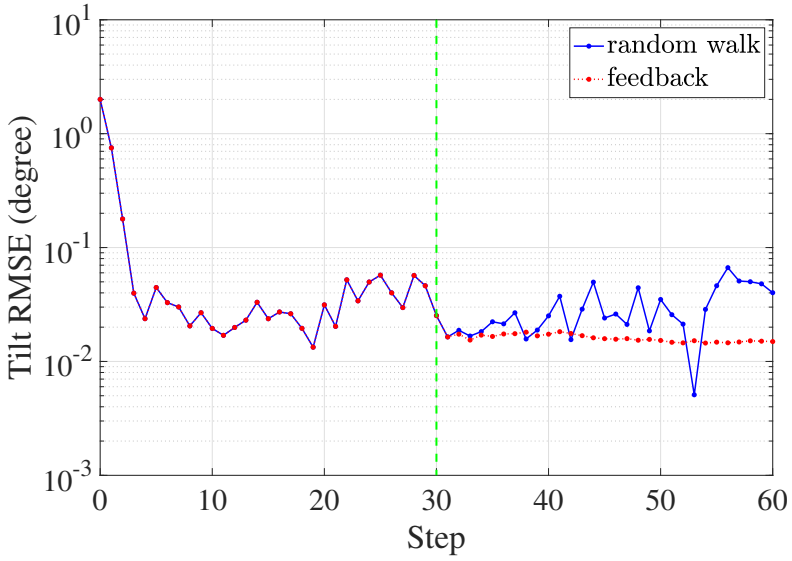

Figure 3.32: RMSE of tilt estimates with and without LQR feedback in the simulation. Assuming the process noise variance scales with the magnitude of the control input.

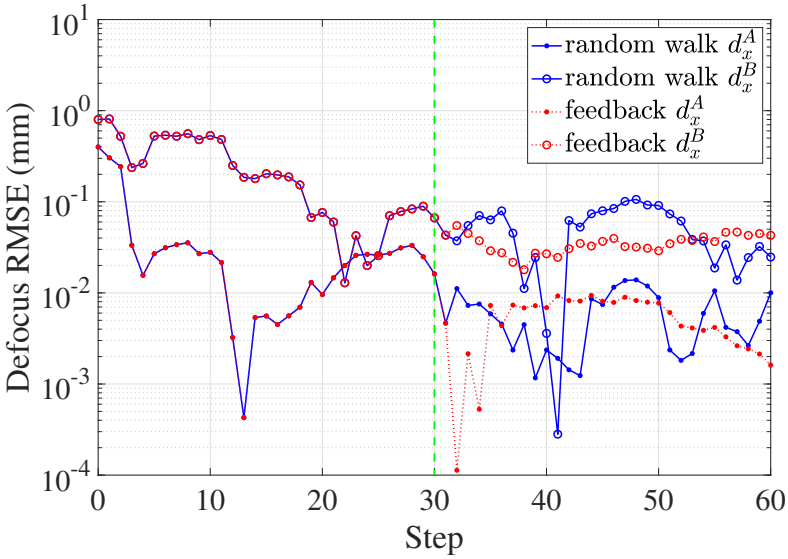

Figure 3.33: RMSE of defocus estimates with and without LQR feedback in the simulation. Assuming the process noise variance scales with the magnitude of the control input.

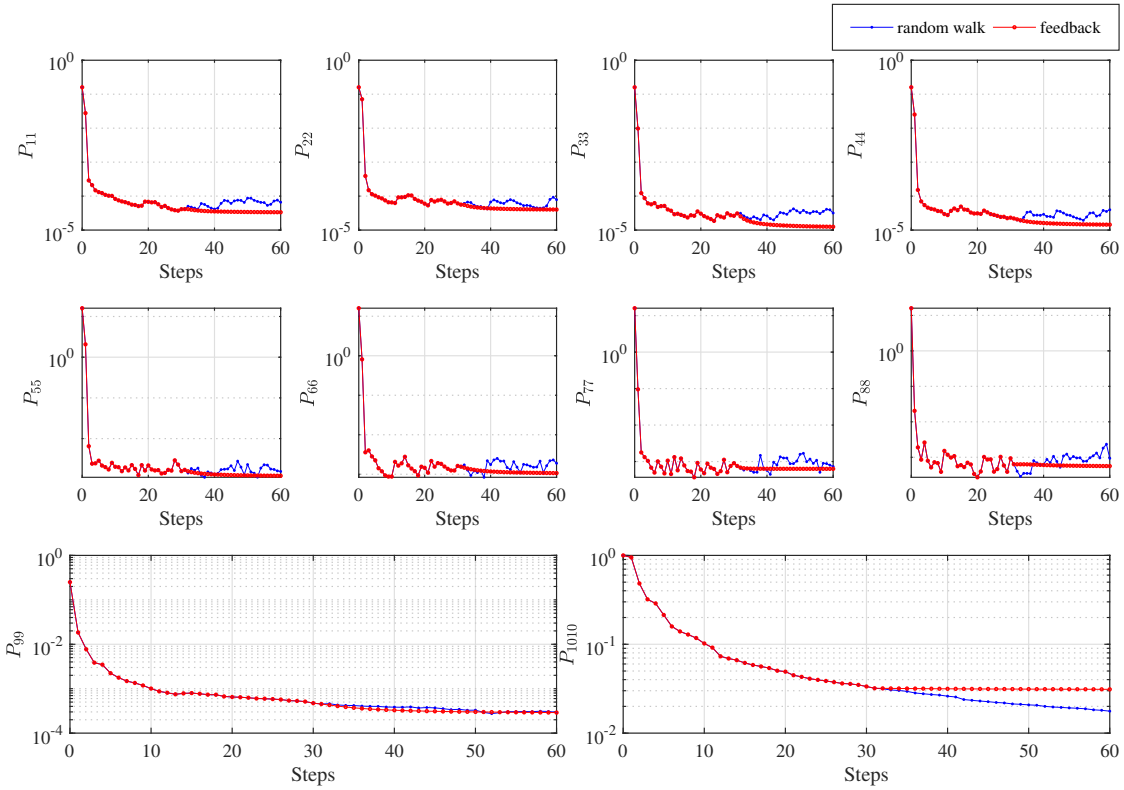

Figure 3.34: The diagonal component of the error covariance matrix in the simulation. P_{ii} represent the variance estimate of the ith state.

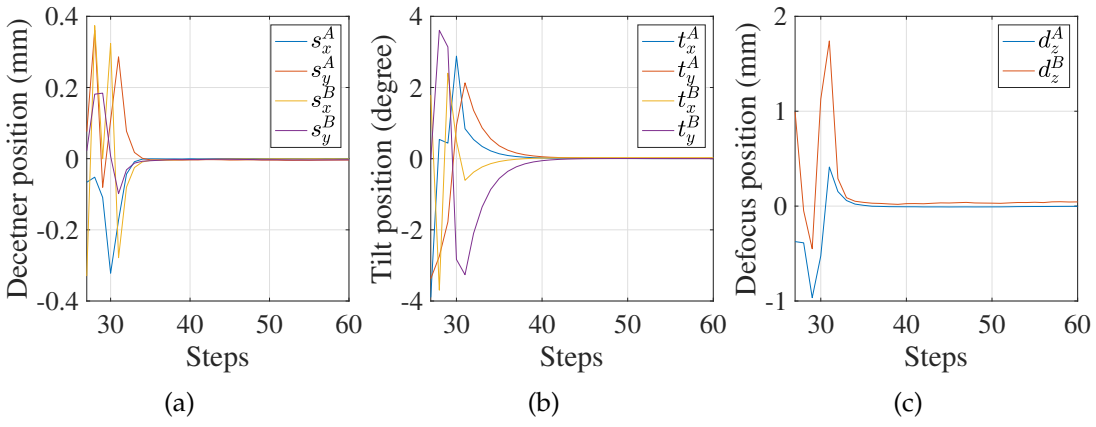

Figure 3.35: True misalignment states in the simulation.

3.6 Application to an Off-axis Parabolic Mirror Alignment

In this section we extended the method to a reflective system using an off-axis parabolic mirror (OAP). The light rays coming from a point source located at the focal point of the OAP are all reflected parallel to the vertical axis of the parabola. OAPs are widely used in optical systems, including, scanning microscopes, digital holographic systems, and space telescopes, because of the unique properties. OAPs are ideal for focusing and light collection in a scanning microscope, such as confocal microscope [66] and scanning electron microscope (SEM) [67]. OAPs can be used to project floating images of formed by a spatial light modulator (SLM) [68]. The OAPs in these systems are usually the most sensitive to misalignment compared to other optical elements. An efficient automated alignment method can greatly decrease the aberration effects in the system, and increases the flexibility of the optical system. For example, it can be used for adjusting the distance between the sample and the OAP to find the best focal point.

3.6.1 Off-axis parabolic mirror optical model

In this section we describe the overall control and estimation process of our optical system. Figure 3.36 shows the optical model and the closed-loop control system. The upper dashed block (plant) is the optical model. A diverging source is reflected by the misaligned OAP and is focused on a camera. The goal is to self-align the OAP which has 5 degrees of freedom - decenter along x, y, and z denoted by D_x, D_y, D_z, and tip and tilt along x and y-axis which is denoted by T_x, and T_y. We assume the rotation along z-axis is aligned ($T_z = 0$). The state vector

of the control system is

$$\boldsymbol{x} = [D_x, D_y, D_z, T_x, T_y]^T. \tag{3.25}$$

The discrete state space representation of the system is

$$\begin{aligned} \boldsymbol{x}_k &= \boldsymbol{F}\boldsymbol{x}_{k-1} + \boldsymbol{B}\boldsymbol{u}_k + \boldsymbol{q}_k \\ \boldsymbol{y}_k &= \boldsymbol{h}(\boldsymbol{x}_k) + \boldsymbol{r}_k\,, \end{aligned} \tag{3.26}$$

where the state transition matrix $\boldsymbol{F}$ and the control input matrix $\boldsymbol{B}$ are taken to be identity matrices. The process noise $\boldsymbol{q}_k$ has a zero mean Gaussian distribution with covariance $\boldsymbol{Q}_k$, $\boldsymbol{q}_k \sim N(0, \boldsymbol{Q}_k)$. The observation function $\boldsymbol{h}$ is a nonlinear function which maps the misaligned states $\boldsymbol{x}_k$ to the measurement $\boldsymbol{y}_k$, and $\boldsymbol{r}_k \sim N(0, \boldsymbol{R}_k)$ is the measurement noise.

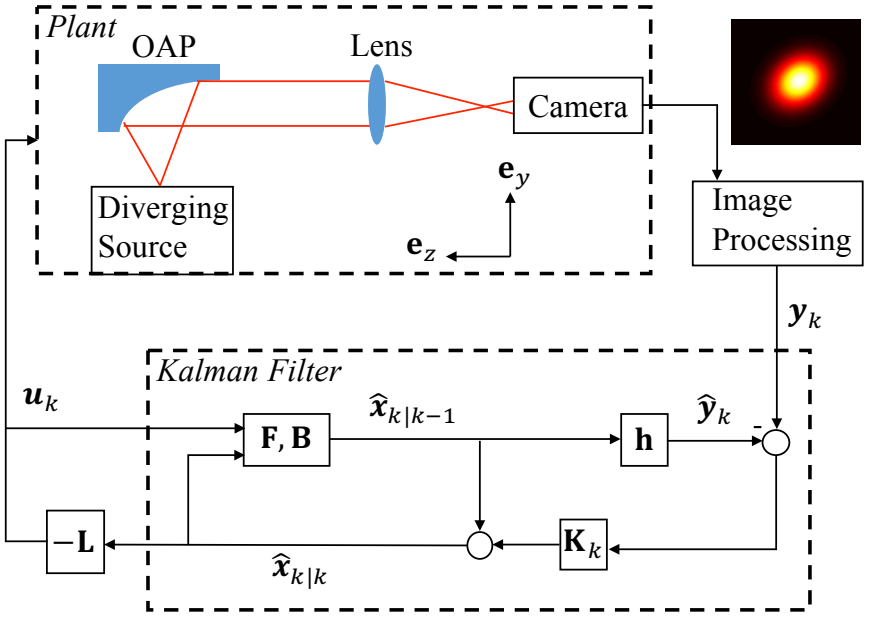

Figure 3.36: Optical model and control system. The upper dashed block represent the plant, and the lower dashed block is the Kalman filter.

The images captured from the camera are sent to a computer and go through

an image processing algorithm, from which the measurement $\boldsymbol{y}$ is obtained. The measurements and the previous command inputs are sent to the Kalman filter. The lower dashed block in Figure 3.36 represents the Kalman filter, which includes state transition matrix $\boldsymbol{F}$, control input matrix $\boldsymbol{B}$, and nonlinear measurement function $\boldsymbol{h}$. The state posteriori $\hat{\boldsymbol{x}}$ and state estimation covariance $\boldsymbol{P}$ are updated given the measurement residual and the computed Kalman gain $\boldsymbol{K}_k$. The next command input $\boldsymbol{u}_k$ can be obtained given the state estimate and the gain $\boldsymbol{L}$ computed using linear-quadratic regulator (LQR).

We use ZEMAX to simulate images with misalignment parameters. In the prescription in ZEMAX, the collimated beam is initially focused by the first lens with focal length 100 mm as shown in Figure 3.37. The beam starts to diverge after the first lens's focal point, and incident on the 90° OAP with reflected focal length 152.4 mm. The light reflected by the OAP is then focused by the second lens with focal length 150 mm to the camera.

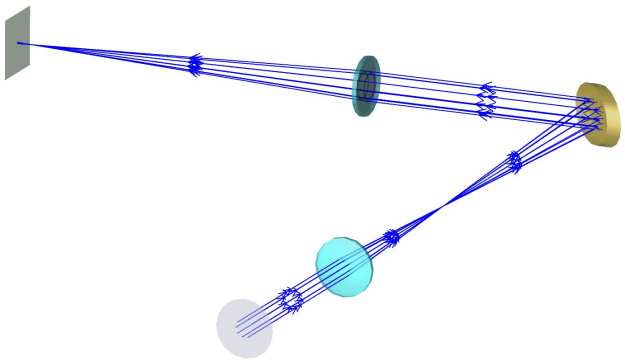

Figure 3.37: Simulated optical system in ZEMAX. The collimated beam passes through the first lens, reflected by the OAP, and focused by the second lens to a camera.

3.6.2 Simulation

The Gaussian center C_x and C_y, together with the weights of K-L modes w_1, w_2, and w_3, normalized by weight w_0, are used as the measurements. The measurement $\boldsymbol{y}$ can be written as

$$\boldsymbol{y} = [C_x, C_y, \frac{w_1}{w_0}, \frac{w_2}{w_0}, \frac{w_3}{w_0}]^T. \tag{3.27}$$

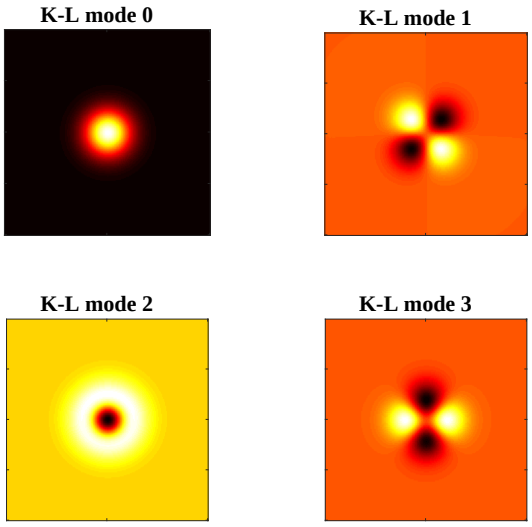

Figure 3.38: First 4 K-L modes obtained from PCA decomposition.

Image Noise

In the simulation we consider shot noise and CCD read noise [69]. The shot noise is caused by the random arrival of photons, and the arrival in a given time period is a Poisson distribution. The on-chip sources of noise that affect the measurement is the CCD read noise. CCD read noise can be expressed as a Gaussian distribution. We add Gaussian and Poisson image noise to 2000

simulated images. Both types of image noise result in a Gaussian distribution measurement noise in $\boldsymbol{y}$. The error between the noisy and noise-free measurements is $\boldsymbol{e}_{noise} = \boldsymbol{y}_{noise} - \boldsymbol{y}$. The scaled measurement error $\boldsymbol{e}^N_{noise}$ can be computed as

$$e^S_{noise,j} = \frac{e_{noise,j}}{\max\left(e_{noise,j}\right) - \min\left(e_{noise,j}\right)}, \tag{3.28}$$

where j represents the jth measurement. Figure 3.39 shows the scaled measurement error distributions of those images. We can see the error distribution of measurements y_1 to y_5 are close to normal distribution. As a result, we can model this measurement noise as white noise in Kalman filtering. The error covariance of the image noise is represented by matrix $\boldsymbol{R}_{sensor}$.

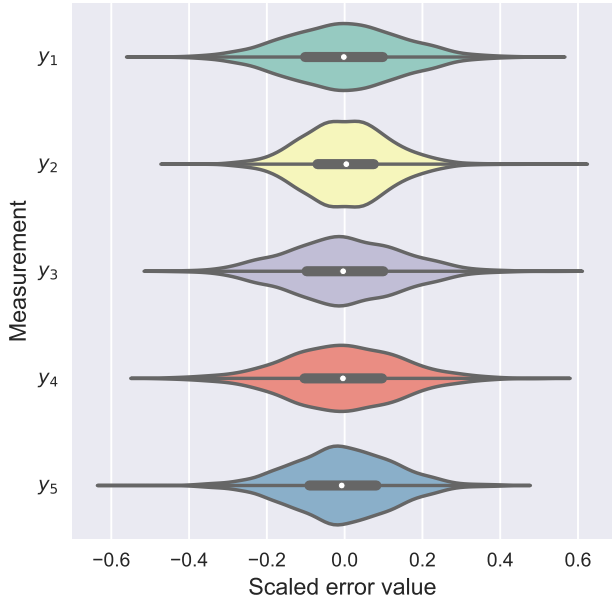

Figure 3.39: Scaled measurement error distribution of the 2000 simulated images with Gaussian and Poisson noise. Random misaligned states are given in the simulation.

Measurement Function

We collect training and test image sets by giving random misalignments in ZEMAX. We visualize the relationship between the state variables and the measurement, and express the nonlinear measurement model function $\boldsymbol{h}$ as follows

$$\begin{bmatrix} y_1 \\ y_2 \\ y_3 \\ y_4 \\ y_5 \end{bmatrix} = \begin{bmatrix} c_1^1 x_1 + c_1^2 x_2 \\ c_2^1 x_1^2 + c_2^2 x_2 + c_2^3 x_3 + c_2^4 x_4 + c_2^5 x_5^2 \\ c_3^1 x_1 + c_3^2 x_5 \\ c_4^1 x_1^2 + c_4^2 x_2 + c_4^3 x_3^2 + c_4^4 x_4 + c_4^5 x_5^2 \\ c_5^1 x_2^2 + c_5^2 x_3 + c_5^3 x_4 + c_5^4 x_5^2 \end{bmatrix}, \tag{3.29}$$

where y_1 to y_5 are the measurement, x_1 to x_5 are the states, and c_k^j is the jth coefficient of measurement k. We perform a nonlinear least squares fitting on the training set (5000 images) using the Levenberg-Marquardt algorithm [61]. The coefficients c_k^j are found, and the nonlinear measurement function $\boldsymbol{h}$ is learned to predict measurement $\boldsymbol{y}$, computed as $\hat{\boldsymbol{y}} = \boldsymbol{h}(\boldsymbol{x})$.

The error between the simulated and predicted measurements is $\boldsymbol{e} = \hat{\boldsymbol{y}} - \boldsymbol{y}$. Figure 3.40 shows the distribution of the scaled measurement error $e_j^S = e_j/(\max e_j - \min e_j)$ on the test set (5000 images). As the image noise error distribution in Figure 3.39, the model error distributions are close to normal distribution and can be treated as white noise in Kalman filtering. We can compute the error covariance of the measurement model $\boldsymbol{h}$ as

$$\boldsymbol{R}_{model} = \boldsymbol{e}\boldsymbol{e}^T, \tag{3.30}$$

and is used as part of the measurement covariance matrix $\boldsymbol{R}$ in Kalman filtering. The normalized root-mean-square error (NRMSE) are calculated as

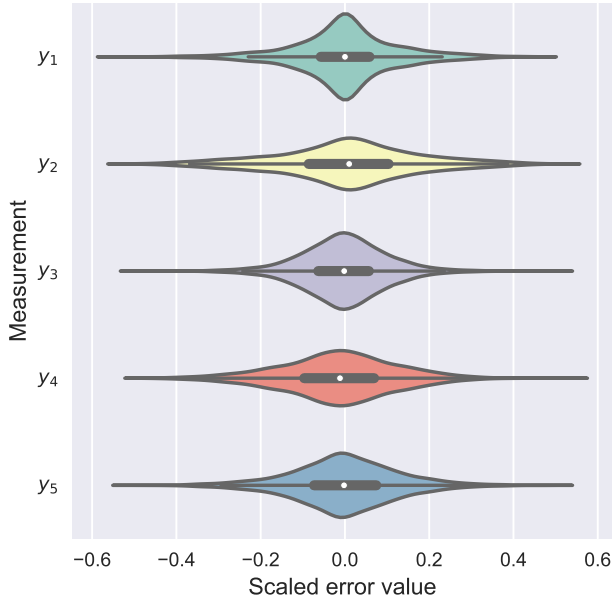

Figure 3.40: Scaled measurement model error distribution of 5000 images in the test set. Random misaligned states are given in the simulation.

Table 3.4: NRMSE of measurement error e_1 to e_5. Both training and test error are computed to ensure the model is not overfitted.

NRMSE (%)	e_1	e_2	e_3	e_4	e_5
Training set	0.07	0.24	1.10	1.35	0.99
Test set	0.07	0.25	1.05	1.34	1.01

$$\text{NRMSE}(e_j) = \frac{\sqrt{\sum_{i=1}^{n} e_{j,i}^2 / n}}{\max y_j - \min y_j}. \tag{3.31}$$

where i ranges from 1 to n for n points in the dataset. We compare the NRMSE between the training set and the test set (as shown in Table 3.4) to ensure the model is not overfitted.

Nonlinear Kalman filtering and observability

Since our state transition is linear, the nonlinear approximation only occurs in the measurement update step. The total measurement noise covariance is $\boldsymbol{R} = \boldsymbol{R}_{model} + \boldsymbol{R}_{sensor}$. $\boldsymbol{R}_{model}$ and $\boldsymbol{R}_{sensor}$ are the model function error covariance and image noise covariance discussed in Section 3.6.2 and 3.6.2. The nonlinear observability can be determined by the observability matrix

$$O = \frac{\partial}{\partial \boldsymbol{x}} \begin{bmatrix} h_1(\boldsymbol{x}) \\ h_2(\boldsymbol{x}) \\ \vdots \\ h_5(\boldsymbol{x}) \end{bmatrix}_{\boldsymbol{x}_0} = \begin{bmatrix} c_1^1 & c_1^2 & 0 & 0 & 0 \\ 2c_2^1 x_{1,0} & c_2^2 & c_2^3 & c_2^4 & 2c_2^5 x_{5,0} \\ c_3^1 & 0 & 0 & 0 & c_3^2 \\ 2c_4^1 x_{1,0} & c_4^2 & 2c_4^3 x_{3,0} & c_4^4 & 2c_4^5 x_{5,0} \\ 0 & 2c_5^1 x_{2,0} & c_5^2 & c_5^3 & 2c_5^4 x_{5,0} \end{bmatrix}. \tag{3.32}$$

where $x_{i,j}$ is the the ith state at step j. The observability matrix is always full rank ($rank(O)$=5) at any initial conditions given the coefficients learned in Section 3.6.2. The Kalman estimation together with LQR feedback is used to correct the misalignment.

Simulation Result

In the simulation the state residual is computed as $\tilde{\boldsymbol{x}} = \hat{\boldsymbol{x}} - \boldsymbol{x}$. Figure 3.41(a) and 3.41(b) show the decenter and tip-tilt state residuals respectively. IEKF estimation achieves approximately 1 μm error in decenter states D_x, D_y, and D_z. Figure 3.41(b) shows that it achieves around 2 arcsec error in tip-tilt states T_x and T_y after few steps.

The standard deviation is square root of each diagonal elements of the state

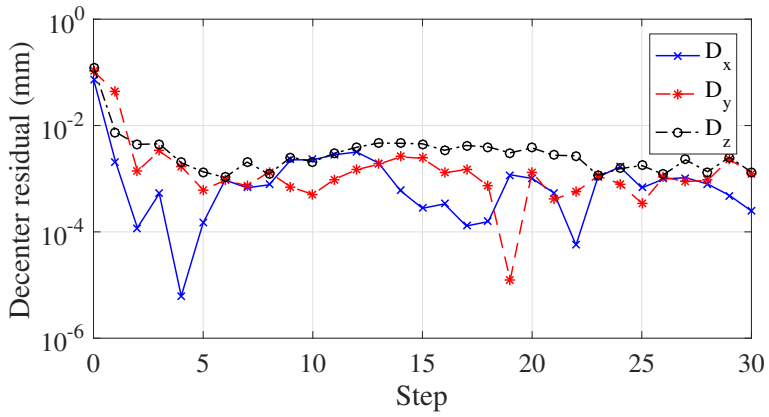

(a)

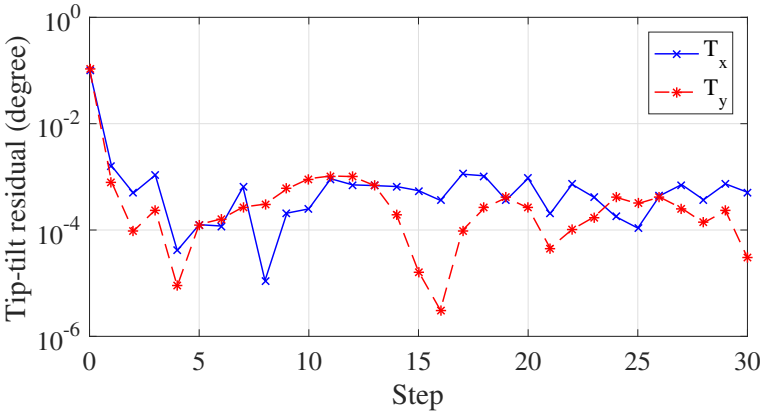

(b)

Figure 3.41: State residuals of decenter and tip-tilt using IEKF. IEKF estimation achieves approximately 1 μm and 2 arcsec errors in decenter and tip-tilt state respectively.

estimate covariance matrix $\boldsymbol{P}_k$ in IEKF simulation. This is the uncertainty of our state estimate given by the Kalman filter. Figure 3.42 shows that the uncertainty in the state estimate decreases rapidly in the first few steps.

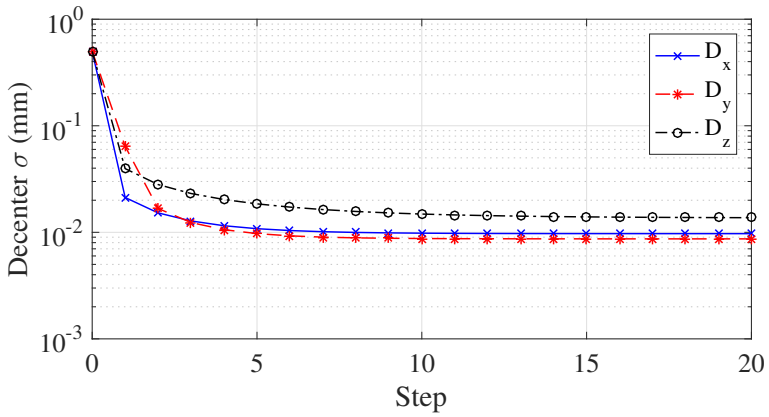

(a)

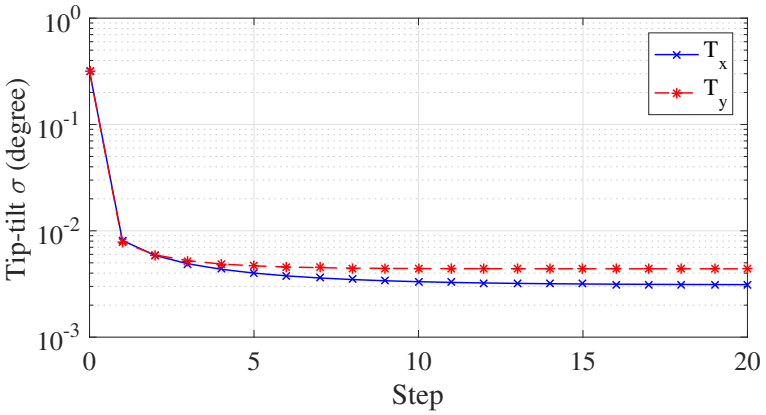

(b)

Figure 3.42: Standard deviation of the state estimate of decenter and tip-tilt using IEKF in the simulation.

3.6.3 Experiment

Setup

Figure 3.43 shows the experimental setup which has the same layout as Figure 3.37. The 635 nm laser beam passes through a customized collimator to produce a collimated beam. A neutral density (ND) filter is installed after the collimator to reduce the power of the collimated beam. The first lens is placed 100 mm after the ND filter, and the OAP is placed approximately 250 mm after the first lens.

The beam is reflected by the OAP and passes through the second lens, which is placed 100 mm away from the OAP. The CCD camera is 155 mm away from second lens. Both lenses hard mounted on the table, and the OAP is mounted on motorized tip-tilt and translation stages. The stages and CCD camera are connected to the computer which performs all closed-loop control processes, and can send actuation commands to the stages. Table 3.5 shows the detailed information of the optical components and devices in the experiment.

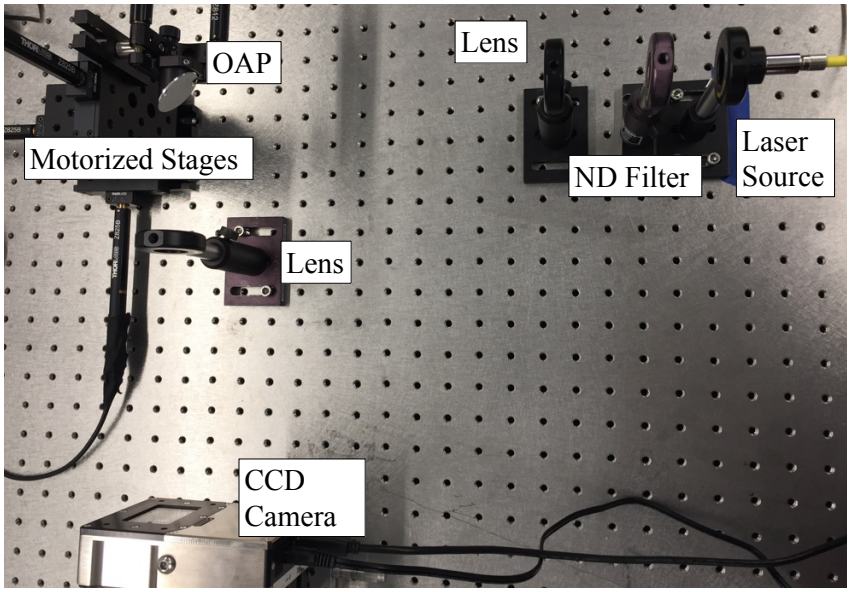

Figure 3.43: Experiment setup of optical model. The optical system after the ND filter is setup as the ZEMAX simultion shown in Figure 3.37. The detailed information of the optical components and devices are listed in Table 3.5.

Results

In the experiment we need to estimate the process noise and measurement noise covariance matrices. The process noise is estimated given the specifications of the motorized stages. The standard deviation of the process noise is

Table 3.5: List of components and devices in the experiment. The optical components, stages, and laser are from Thorlabs.

Item	**Model**	**Description**
Collimator	TC25FC-633	Diameter ($1/e^2$): 4.67 mm
ND filter	NE50B-A	OD: 5.0
Lens (first)	LB1676-A	Focal length: 100 mm
OAP	MPD169-P01	Focal length: 152.4 mm
Lens (second)	LB1437-A	Focal length: 150 mm

$[0.005, 0.005, 0.005, 0.04, 0.04]^T$. The process noise covariance matrix is an diagonal matrix, where the diagonal elements equal to the square of the standard deviations. The measurement noise covariance $\boldsymbol{R} = \boldsymbol{R}_{model} + \boldsymbol{R}_{sensor}$. $\boldsymbol{R}_{model}$ is the same as the one discussed in Section 3.6.2. $\boldsymbol{R}_{sensor}$ is obtained experimentally in the lab. We collect many stationary image sets at multiple stage positions in the experiment, and compute the standard deviation of of each data set to find the average standard deviation of the measurement as $\sigma_{sensor} = [0.33, 0.44, 0.73, 1.05, 0.82]^T \times 10^{-3}$. $\boldsymbol{R}_{sensor}$ is a diagonal matrix with the square of the standard deviation as its diagonal elements. With the estimation of the noise covariance matrices, the Kalman filter can be executed to update state estimates in the closed-loop control system.

Since the actual state is unknown in the experiment, we examine the performance from the measurements and the stage positions. In a perfectly aligned system we expect the spot shits to the camera center and have zero K-L weights. This is corresponding to measurement $\boldsymbol{y} = \boldsymbol{0}$. Figure 3.44(a) and 3.44(b) show

the center positions and the K-L weights for the first 20 steps in the experiment respectively. Both plots show the measurements converge close to zero. The Gaussian centers C_x and C_y approach zero quickly in the first few steps. The K-L weights approach zero gradually and have relatively larger bias in the end.

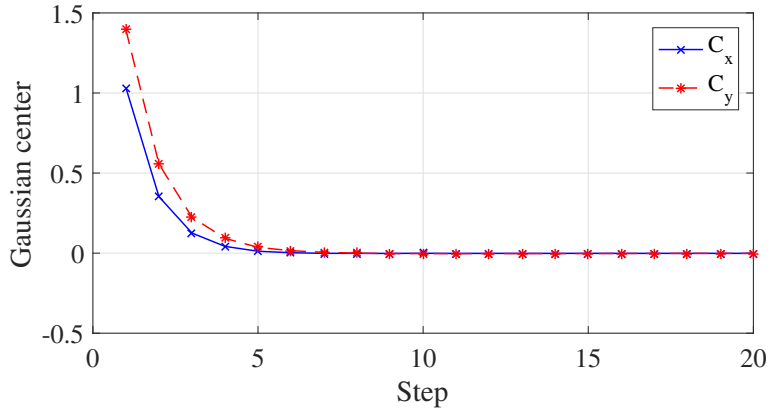

(a)

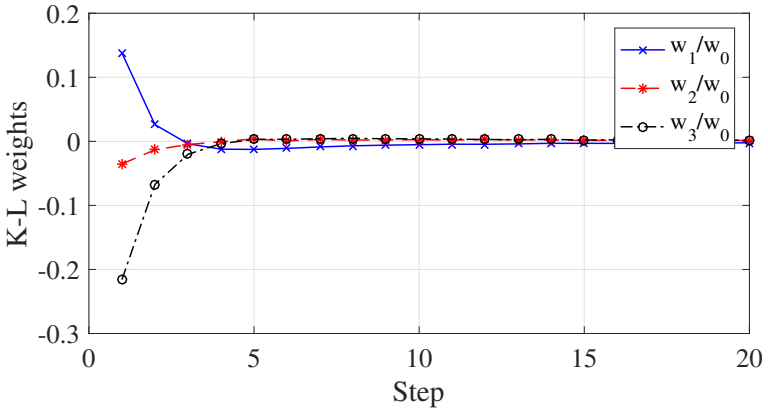

(b)

Figure 3.44: Measurements in the experiment. (a) Gaussian position measurements in the experiment. (b) K-L weights measurements in the experiment.

Figures 3.45(a) and 3.45(b) show the translation and tip-tilt stage positions of the same experiment as Figure 3.44. All the stages approach steady-state values gradually. We shift the stage position value by the steady-state values (step

50) of each stage for visualization purpose. Figure 3.46(a) and Figure 3.46(b) show the image before and after this run. The images at the left are captured in global frame (1000 × 1000 pixels), and the images at the right are the subframes (200 × 200 pixels) which are interpolated around the Gaussian center C_x and C_y. The intersection of the green dot-dashed lines in the global frame represent the center of the camera, and the one in the local frame represents the Gaussian center. After the closed-loop self-aligning process, the spot shifts to the camera center and become axial-symmetric.

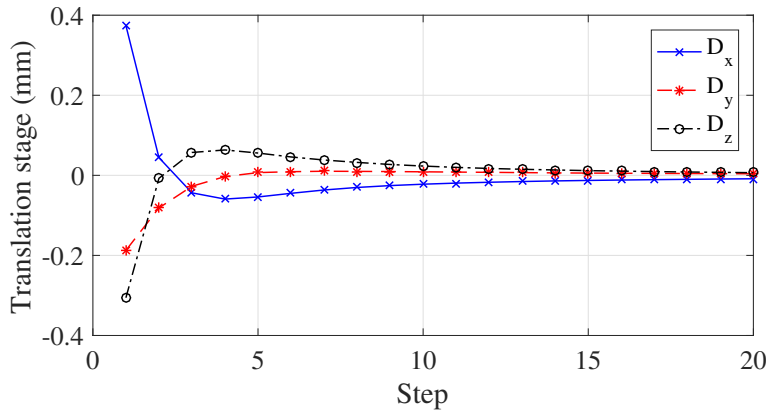

(a)

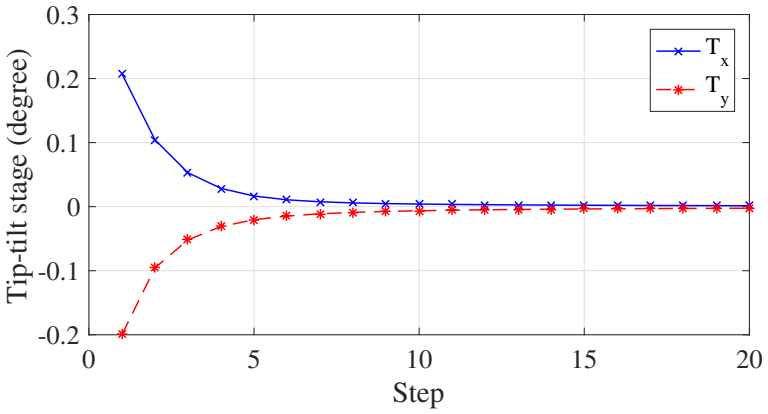

(b)

Figure 3.45: Stage position in the experiment. (a) Position of translation stages. (b) Position of tip-tilt stages.

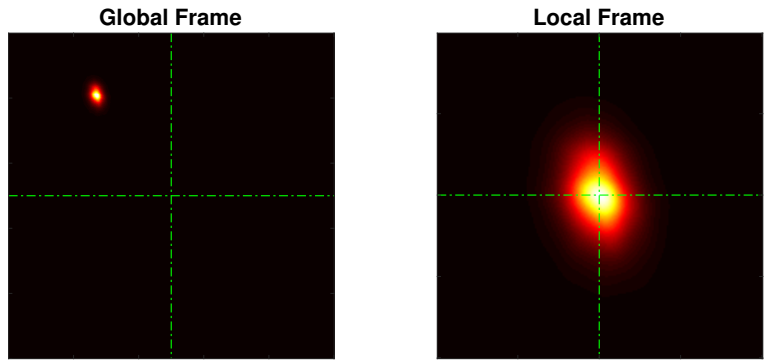

(a)

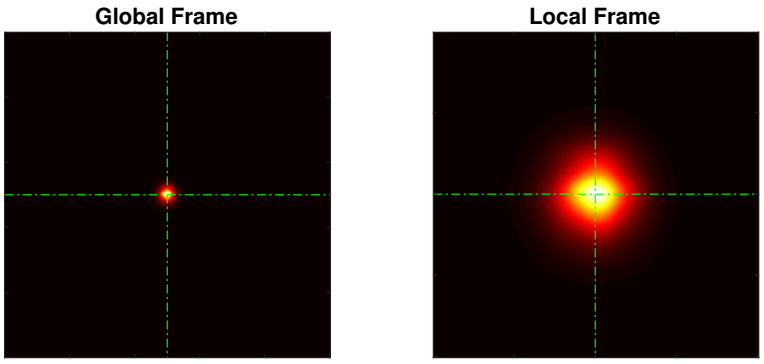

(b)

Figure 3.46: Image before and after the self-aligning process in the experiment. The images at the left are captured in global frame, and the images at the right are the subframes which are interpolated around the Gaussian centers. (a) before. (b) after.

The stage positions converge to steady-state values in a single test, but the final values vary in between different runs. We rerun the experiments for 100 times with different initial misalignment parameters, and examine the standard deviations of the final stage positions of all runs as shown in Table 3.6. Table 3.7 shows the means and standard deviations of the final measurements of the 100 tests. The mean of the measurement represents the bias in these experiments and the standard deviation shows the precision in between runs.

The self-aligning method can be separated into two steps: 1. Image processing. 2. State estimation and control. In the image processing step we use

Table 3.6: Standard deviations of the final stage positions of 100 tests with different initial misalignment parameters.

State	Standard deviation
D_x	4.1 μm
D_y	7.5 μm
D_z	2.8 μm
T_x	3.5 arcsec
T_y	2.8 arcsec

Table 3.7: Means and standard deviations of the final measurements of 100 tests with different initial misalignment parameters.

Measurement	Final value
C_x	0.62 ± 1.80 μm
C_y	-0.06 ± 1.34 μm
w_1/w_0	0.07 ± 1.14 ($\times 10^{-3}$)
w_2/w_0	-1.55 ± 1.87 ($\times 10^{-3}$)
w_3/w_0	0.16 ± 1.84 ($\times 10^{-3}$)

Gaussian fitting and PCA projection to find the measurements. K-L modes obtained given misalignment parameters are similar to low order Zernike modes. K-L mode 2 corresponds to the defocus mode, and K-L mode 1 and 3 are related to astigmatisms. Coma related K-L modes are also found but not included as measurements in the control system. K-L modes can better describe the effects of the states than Zernike modes because they are decomposed directly from the misaligned optical system. Moreover, Zernike modes are not ideally suited

for projecting elliptical spots onto rectangular grids.

In state estimation and control, the nonlinear Kalman filter and LQR successfully estimate and correct the misalignments. In the simulation we show the convergency of the state residuals after the closed-loop control. The state residuals cannot be examined in the experiment since the actual states are unknown. We show the convergency of the measurements in the experiment, and present the uncertainly of the states and measurements in between 100 tests. The deviation in between these tests is caused by several factors. The obvious one is the error in the nonlinear estimation. The process noise and measurement noise are discussed. The measurement noises include image noise and measurement model function error. The process noise are actuator repeatability, backlash, and stage hysteresis. The other possible effect is thermal drifts which is nonlinear and not modeled in this paper. The bias in the measurement is possibly caused by the slight misalignments of other components in the system.

CHAPTER 4

AMPLITUDE AND PHASE RETRIEVAL WITH SIMULTANEOUS DIVERSITY ESTIMATION USING EXPECTATION MAXIMIZATION

4.1 Introduction

We introduce various wavefront sensing and phase retrieval methods in Section 1.1 and 1.3. In the chapter an dual estimation framework for simultaneously reconstructing the wavefront and focus diversity is discussed. Algorithms including expectation-maximization (EM), dual, and joint Kalman estimation are widely used for estimating the state of a dynamic system and the model parameters simultaneously.

Dual estimation problems are very common in phase retrieval applications. The input object and optical aberrations can be jointly estimated using phase diversity [70]. A nonlinear optimization approach is used to jointly optimize over the object, the illumination beam, and the translation parameters [71]. The alternating minimization approach is used in phase recovery and source recovery [72, 73]. A conjugate-gradient nonlinear optimization is used in field retrieval with hard-edged and uniformly illuminated apertures. The unknown field and system parameters, including the focus distance and transverse shifts, are estimated by minimizing a weighted normalized mean-squared error metric [74]. The unknown continuous parameters of discrete optical propagation in phase retrieval algorithms can also be estimated using a gradient derived from algorithmic differentiation method [75]. The OPRA (OTF-based Phase Retrieval Analysis) package used on the Gemini South adaptive optics system for estimating wavefront aberration can simultaneously estimate the defocus and

plate scale parameters [76]. Many existing adaptive optics research and software also solve joint estimation problems along with phase retrieval algorithm [8, 77, 78].

Here we intend to retrieve the amplitude and phase of a wavefront while estimating the position of the moving lens used for generating phase diversity. We use an expectation-maximization (EM) algorithm with Kalman smoothing [79] for this dual estimation problem. The goal is to estimate the unknown hidden states in the E-step, and optimize the likelihood over the parameters given the observation in the M-step [80]. We treat the input field as the set of unknown parameters in the M-step and estimate the lens position, which involves introducing the control input as a hidden state in the Kalman smoothing (E-step).

4.2 Optical Model and Propagation

Figure 4.1 shows a schematic of the optical system with a moving lens. The input complex wavefront to be estimated is $\boldsymbol{U}_1(x, y)$, where x and y are the spatial coordinates perpendicular to the optical axis. $\boldsymbol{U}_1(x, y)$ can be written as $\boldsymbol{A}_1(x, y)e^{i\boldsymbol{\Phi}_1(x,y)}$, where $\boldsymbol{A}_1$ and $\boldsymbol{\Phi}_1$ are the field amplitude and phase, respectively. The distance between the unknown wavefront and the lens is l_1, and the distance from the input field to the camera is l_c. The wavefront at the focal plane is $\boldsymbol{U}_2(x, y) = \boldsymbol{A}_2(x, y)e^{i\boldsymbol{\Phi}_2(x,y)}$, and the wavefront reaching the camera is $\boldsymbol{U}_3(x, y) = \boldsymbol{A}_3(x, y)e^{i\boldsymbol{\Phi}_3(x,y)}$. The data set to be operated on is generated by recording intensities $\boldsymbol{I}(x, y) = |\boldsymbol{U}_3(x, y)|^2$ at the focal plane while moving the lens to different positions. The unknown input wavefront $\boldsymbol{U}_1(x, y)$ is then reconstructed from these intensity measurements.

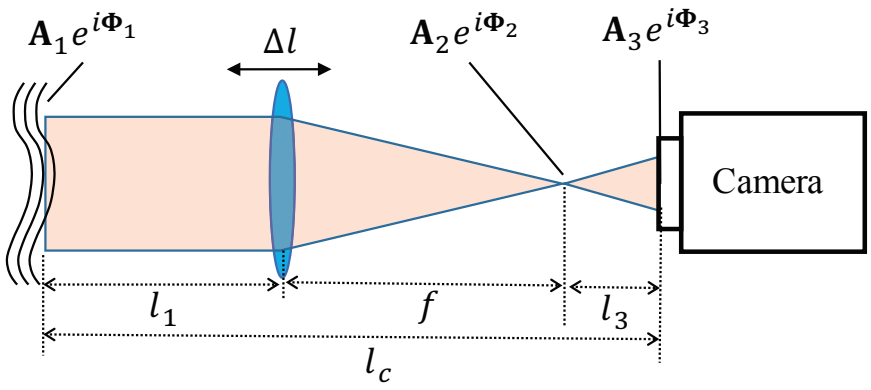

Figure 4.1: Optical model for recording multiple defocused images. The data set is generated by recording intensities at the focal plane while moving the lens to different positions. The unknown input wavefront is then reconstructed from these intensity measurements.

In this chapter the simulation and on bench experiment are conducted in near-field region where the Fresnel and angular spectrum propagation are used. However, the same algorithm can be apply on other optical Propagation as long as the forward and backward propagation formula can be derived. The detail formulas of propagation using Fourier optics are described in Appendix B. The derivation assumes scalar diffraction theory and shows the Rayleigh-Sommerfeld, Fresnel, and Fraunhofer approximations.

The optical propagation of this system is separated into two steps. The input field is propagated all the way to the focal plane, then the angular spectrum method is used for propagation from the focal plane to the camera [74]. When the input field is placed a distance l_1 before a lens with focal length f the optical

field at the focal plane can be computed as

$$\begin{aligned}\boldsymbol{U}_2(x_2, y_2) =& \frac{1}{j\lambda f} \exp\left[j\frac{k}{2f}(1 - \frac{l_1}{f})(x_2^2 + y_2^2) \right] \iint_{-\infty}^{+\infty} \boldsymbol{U}_1(x_1, y_1) \\ & \times \exp\left[-j\frac{2\pi}{\lambda f}(x_2 x_1 + y_2 y_1) \right] dx_1 dy_1. \end{aligned} \tag{4.1}$$

This can be written via a Fourier transform

$$\begin{aligned}\boldsymbol{U}_2(x_2, y_2) =& \frac{1}{j\lambda f} \exp\left[j\frac{k}{2f}(1 - \frac{l_1}{f})(x_2^2 + y_2^2) \right] \\ & \times \mathcal{F}\left\{ \boldsymbol{U}_1(x_1, y_1) \right\} \Big|_{f_X = \frac{x_2}{\lambda f}, f_Y = \frac{y_2}{\lambda f}}, \end{aligned} \tag{4.2}$$

where $\mathcal{F}\{\}$ denotes Fourier transforms, f_X and f_Y are spatial frequencies, λ is the wavelength and $k = 2\pi/\lambda$ is the wavenumber [81]. We fix the distance between the input field and the camera to l_c. Given in the lens position l_1 we can compute the distance between the focal plane and the camera $l_3 = l_c - f - l_1$. The angular spectrum propagation from the focal plane to the camera can be written as

$$\boldsymbol{U}_3(x, y) = \mathcal{F}^{-1}\Big\{ \mathcal{F}\{\boldsymbol{U}_2(x, y)\} H(f_X, f_Y) \Big\}. \tag{4.3}$$

The transfer function $H(f_X, f_Y)$ is given by

$$H(f_X, f_Y) = \exp\Big[jkl_3 \sqrt{1 - (\lambda f_X)^2 - (\lambda f_Y)^2} \Big] \tag{4.4}$$

[82].

One can also propagate from the input field to the image plane in one step using the chirp-Z transform [83] or the matrix multiply transform [84]. In the simulation we use $\lambda = 1$ μm, $f = 600$ mm, $l_c = 4f$ and 4 mm for both the height and width of the input field. The size of the input field is $N \times N$ for $N = 256$ in the simulation.

4.3 Amplitude and Phase Retrieval Algorithm

We use $\mathcal{FP}_{l_1}$ and $\mathcal{BP}_{l_1}$ to represent the forward and backward propagation between the input field and the image plane. Since the distance between the input field and the camera is fixed, the subscript l_1 determines the moving lens position in the optical system. Figure 4.2 shows the flowchart of the phase retrieval algorithm. We record n intensity images $\boldsymbol{I}_k$, where $k = 1, ..., n$, at the image plane. Each measurement is obtained after moving the lens a distance Δl_1 away from the previous measurement.

The phase retrieval algorithm starts with an initial guess of amplitude $\boldsymbol{A}_{1,0}$ and phase $\boldsymbol{\Phi}_{1,0}$. We compute the complex field $\boldsymbol{A}_3 e^{i\boldsymbol{\Phi}_3}$ at the image plane by forward propagating the initial guess. The amplitude $\boldsymbol{A}_{3,k}$ is replaced by the recorded amplitude $\sqrt{\boldsymbol{I}_k}$, then the updated output image $\sqrt{\boldsymbol{I}_k} e^{i\boldsymbol{\Phi}_{3,k}}$ is backward propagated to obtain the updated input field $\boldsymbol{A}_{1,k} e^{i\boldsymbol{\Phi}_{1,k}}$. We compute the input field estimate $\boldsymbol{U}_{est} = \boldsymbol{A}_{est} e^{i\boldsymbol{\Phi}_{est}}$ by averaging over all the updated input fields 1 to n, then pass it as the initial guess of the input field in the next loop.

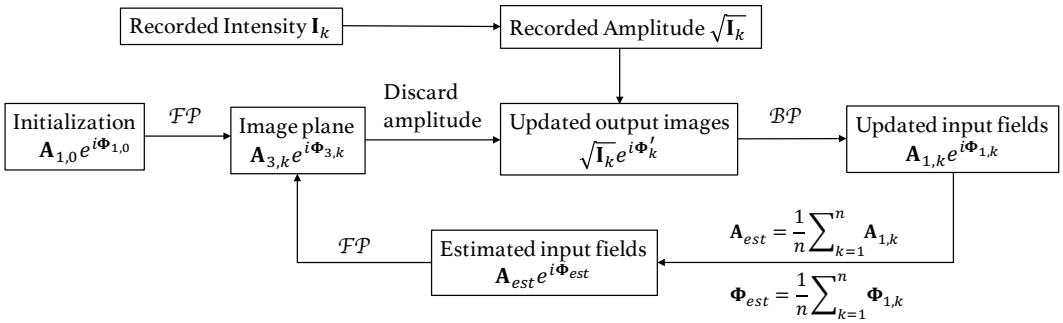

Figure 4.2: Flowchart of the iterative amplitude and phase retrieval algorithm.

4.3.1 Simulation and error metric

The number of measured intensities n and the sequential measurement distance Δl_1 affect the performance of the iterative APR. The rate of convergence increases with increasing number of measurements when $\Delta l_1 = 50$ mm. The input complex field in the simulation is an object with a binary mask and a phase of a combination of 10 Zernike terms. The phase contains Zernike terms from Noll index 4 to 13 with random coefficients [85]. Figure 4.3(a) and 4.3(b) show the binary mask and the phase of the input field respectively. Figure 4.4 shows the intensity measurements at the image plane. The reconstructed field might be multiplied by a constant phase relative to the original field since the algorithm is insensitive to constant phase offset [86]. We compute the mean-squared-error (MSE) of the estimated input field as

$$MSE = \min_{\phi_c} \frac{1}{N^2} \sum_{x=1}^{N} \sum_{y=1}^{N} \left| \boldsymbol{U}_{est}(x,y) \exp(j\phi_c) - \boldsymbol{U}_1(x,y) \right|^2, \tag{4.5}$$

where ϕ_c is a constant phase. Figure 4.5 shows the MSE of the estimated input field using iterative APR algorithm with n intensity measurements, where $n = 4, 6, 8, 10$. The rest of the simulations use $n = 10$ since its rate of convergence outperforms the others. The reconstructed amplitude using 10 measurements is shown in Figure 4.3(c), and the reconstructed phase scaled by the amplitude is shown in Figure 4.3(d).

4.3.2 Effect of focus diversity error

The iterative APR reconstruct the complex field satisfactorily without the position error of the moving lens. In practice, the reconstruction result in such system is generally constrained by the position error of the moving component. We

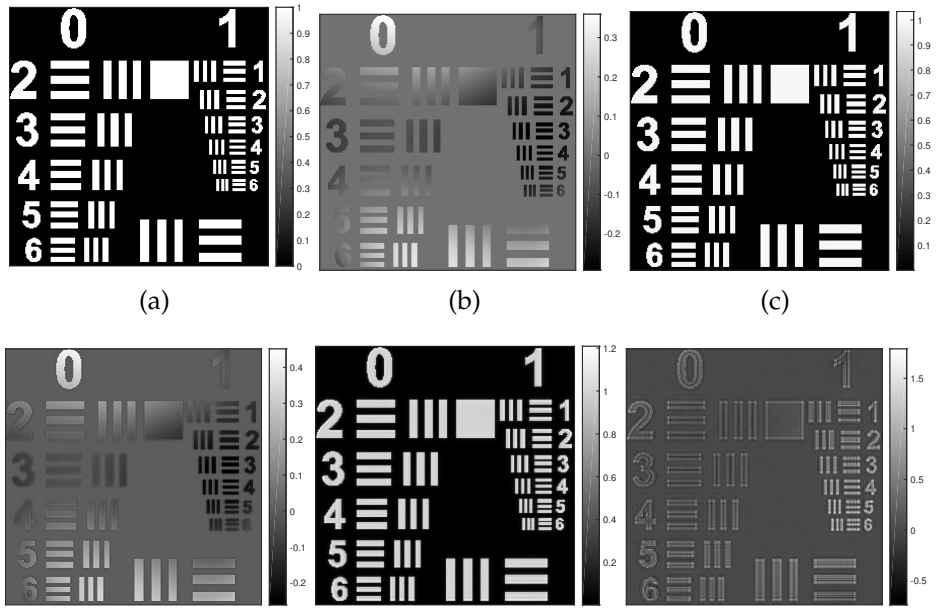

(a) (b) (c)

(d) (e) (f)

Figure 4.3: Input and estimated fields in the simulation: (a) binary mask of the input field, (b) phase of the input field, (c) reconstructed amplitude, (d) reconstructed phase, (e) reconstructed amplitude with position error σ = 1.0%, and (f) reconstructed phase with position error σ = 1.0%.

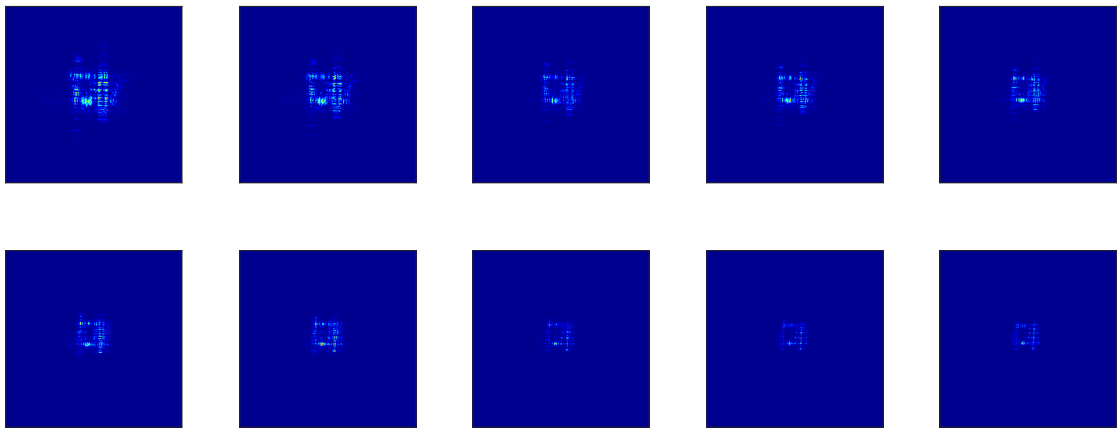

Figure 4.4: Simulated intensity measurement at the image plane.

model the position error of the moving lens by adding a Gaussian distributed noise with a standard deviation σ to the sequential control input. The lens posi-

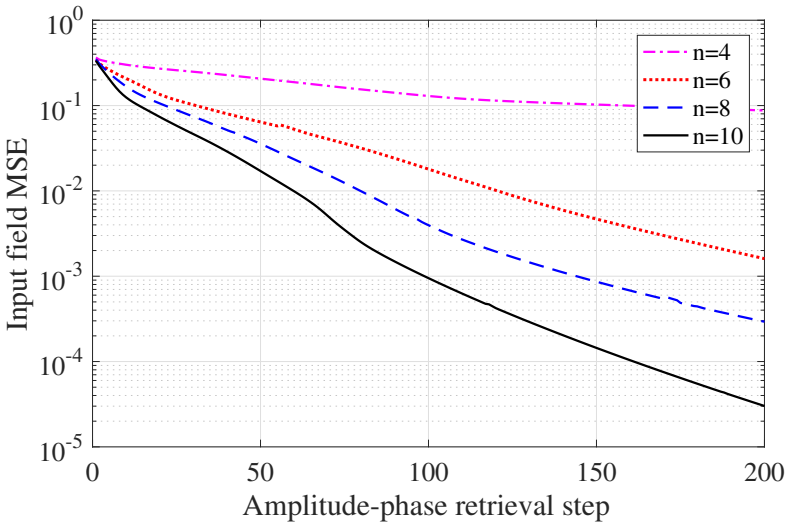

Figure 4.5: MSE of the estimated input field using iterative APR algorithm with n intensity measurements, where $n = 4, 6, 8, 10$.

tion of the kth measurement is $l_{1,k} = l_{1,k-1} + \Delta l_1 + v_{k-1}$, where $v \sim N(0, \sigma)$. Figure 4.6 shows the MSE of the estimated input field using iterative APR algorithm with and without position error. The standard deviation σ is presented as a percentage with respect to Δl_1. The reconstruction result degrades rapidly as the the process noise of the moving lens increases. Figures 4.3(e) and 4.3(f) show the reconstructed amplitude and the reconstructed phase scaled by the amplitude when $\sigma = 1.0\%$. In the next section we present the idea of using EM algorithm and Kalman smoothing for position estimation of the lens.

4.4 Expectation-maximazation Algorithm and Kalman Smoothing

The expectation-maximization (EM) algorithm is an iterative method to find maximum likelihood estimates of parameters from data set with hidden vari-

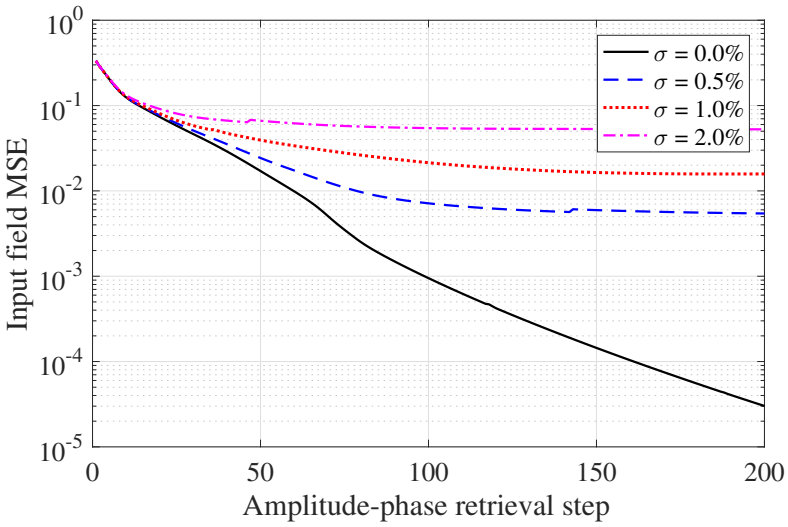

Figure 4.6: MSE of the estimated input field using iterative APR algorithm with and without position error. Standard deviation σ is presented as a percentage with respect to Δl_1.

ables [87]. The EM algorithm alternates between the steps of guessing probability distributions of hidden variables given the current model (known as the E-step) and re-estimating the model parameters using these probability distributions (known as the M-step) [88]. This has been applied to linear and nonlinear stochastic state-space models where the states are hidden from the observer and need to be estimated with the parameters of the model simultaneously [89]. In a nonlinear dynamical system an extended Kalman smoother can be used to estimate the state in the E-step, while an optimization is performed in the M-step to re-estimate the model parameters using these uncertain state estimates [80].

We use an extended Kalman smoother (EKS) for estimation of the lens position in E-step. The EKS process includes a forward filtering (EKF) and a backward smoothing step [90]. The iterated extended Kalman filter (IEKF) is used for the forward filtering pass. The prior and posterior state estimates and

covariances from step 1 to n are stored during the forward filtering process. The Rauch-Tung-Striebel (RTS) smoother [91] which utilizes the stored values is used in the backward smoothing pass. Figure 4.7 shows the schematic of EM algorithm with Kalman smoothing. The EKF takes control input, estimated complex field from the M-step and recorded intensity as inputs and outputs state estimates. Both the state, covariance estimates and their priors are stored during the forward filtering pass, and then sent to the RTS smoother to find the final state estimate. The final state estimate is used in the APR algorithm in the next EM step.

In this problem we treat the input field $\boldsymbol{U}$ as unknown parameters to be estimated in the M-step, and the lens position l_1 as the latent variable assuming the sequential control inputs preserve Markov properties. We iterate over the E-step and M-step N_{EM} times with the recorded intensities $\boldsymbol{Z} = \{\boldsymbol{I}_1, \boldsymbol{I}_2, ..., \boldsymbol{I}_n\}$ as the observations. In the M-step the iterative APR algorithm is used to obtain the estimated input field as shown in Figure 4.7. The goal is to maximize the probability of the measurement given the current estimated lens positions and the measurements

$$\boldsymbol{U}^{(t)} = \underset{\boldsymbol{U}}{\operatorname{argmax}} \Pr\left(\boldsymbol{Z} | \boldsymbol{q}_1^{(t)}, \boldsymbol{q}_2^{(t)}, ..., \boldsymbol{q}_n^{(t)}, \boldsymbol{U}\right), \tag{4.6}$$

where $t = 1...N_{EM}$ is the step in the EM algorithm. $\boldsymbol{q}_m^{(t)}$ is the distribution of the state estimate which is Gaussian with a mean and variance obtained in Kalman smoothing, where $m = 1...n$ is the index of each successive image taken (the recorded intensity values). Instead of training the entire M-step every iteration in the EM algorithm, which might be quite time consuming, we execute N_{APR} loops in the iterative APR algorithm in between the E-steps.

In the E-step we obtain the estimated l_1 positions at which we record the

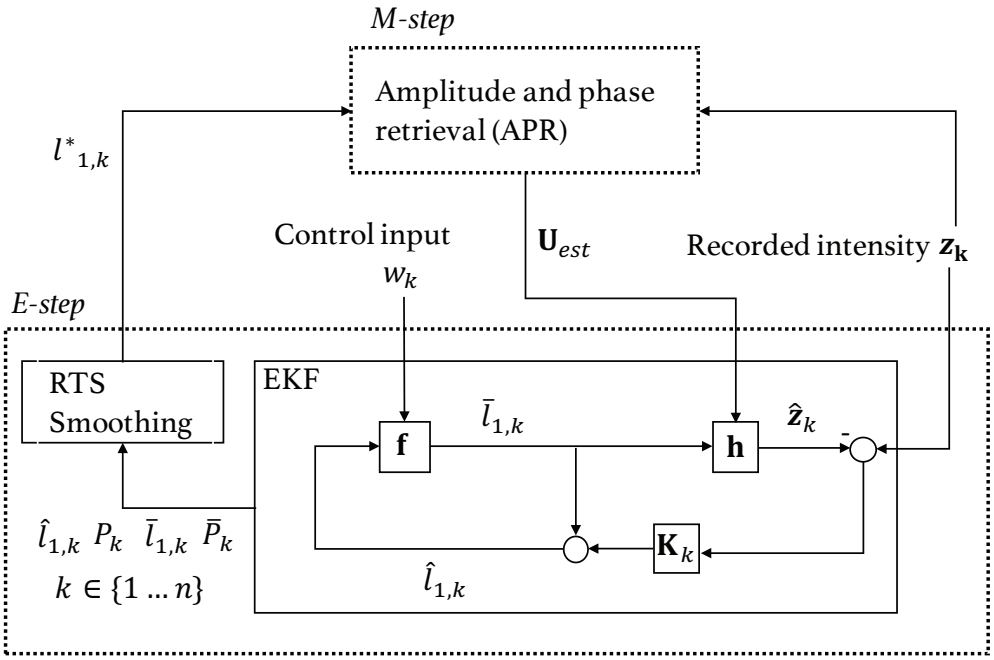

Figure 4.7: Schematic of expectation-maximization algorithm with Kalman smoothing. EKF takes control input w_k, estimated complex field $\boldsymbol{U}_{est}$ from the M-step and recorded intensity z_k as input. Both the state and covariance estimates ($\hat{l}_{1,k}$, P_k) and priors ($\bar{l}_{1,k}$, $\bar{P}_k$) are stored during the forward filtering pass, and then sent to the RTS smoother to find the final state estimate $l^*_{1,k}$. The final state estimate is used in the APR algorithm in the next EM step.

intensities using Kalman smoothing. The distribution of l_1 is estimated given the current measurements and the previous estimation of the input field ($\boldsymbol{U}_{est}$)

$$\boldsymbol{q}^{(t)} = \Pr(l_1 | \boldsymbol{Z}, \boldsymbol{U}^{(t-1)}), \tag{4.7}$$

The complex field at the image plane can be computed as $\boldsymbol{U}_3 = \mathcal{FP}_{l_{1,k}}\{\boldsymbol{U}_1\}$. We rewrite the complex field $\boldsymbol{U}_3$ as a raster-scanned complex column vector $\boldsymbol{u}_{l_{1,k}}$. The state space representation in Kalman smoothing can be written as

$$\begin{aligned} l_{1,k+1} &= \boldsymbol{f}(l_{1,k}, w_k) + v_k = l_{1,k} + w_k + v_k \\ \boldsymbol{z}_k &= \boldsymbol{h}(\boldsymbol{U}_1, l_{1,k}) + \boldsymbol{r}_k = \mathrm{diag}(\boldsymbol{u}_{l_{1,k}}{}^*)\boldsymbol{u}_{l_{1,k}} + \boldsymbol{r}_k, \end{aligned} \tag{4.8}$$

where k represents the kth step Kalman smoothing, w_k is the control input at the kth step, and z_k is the intensity measurement $\boldsymbol{I}_k$ in vector form. v_k and $\boldsymbol{r}_k$ are the process and measurement noise at the kth step, and $(\cdot)^*$ denotes the complex conjugate of a vector. $\boldsymbol{f}$ and $\boldsymbol{h}$ are the state transition and nonlinear measurement functions, respectively. The Kalman gain $\boldsymbol{K}_k$ in Figure 4.7 can be computed with the Jacobian of $\boldsymbol{f}$ and $\boldsymbol{h}$, the noise covariance matrices and state prior. Finally the Covariance-based fixed interval RTS smoother is used for the smoothing process. The details of the computation in EKF and RTS smoother can be found in [47] and [92].

The process noise covariance is σ^2, and the measurement noise covariance is a diagonal matrix $\boldsymbol{R}_k$. $\boldsymbol{R}_k$ includes not only the intensity measurement noise but also the error of the input field estimation in the M-step which is carried to the E-step. We simplify the problem by assuming that the error is independent among all pixels and they all have the same covariance σ_R^2. This tends to overestimate the covariance of the pixels with lower intensity values. However, a higher covaraince matrix tends to increase the gain of the state estimation in the Kalman filter, and results in a better input field prediction after many EM steps.

4.5 Simulation

4.5.1 Phase Retrieval Result

We set $N_{APR} = 20$ and $N_{EM} = 10$, then simulated the EM algorithm with Kalman smoothing (EM-KS) using the same input field and initial conditions as in the iterative APR. Figure 4.8 shows the result of the EM algorithm compared to the

iterative APR when the position error $\sigma = 1.0\%$. The final MSE of the reconstruction in the iterative APR is much larger than the one in the EM algorithm. An alternative E-step can be done by running a nonlinear least-square optimization which minimizes the absolute error of the intensity at each lens position. The blue circle line in Figure 4.8 shows the result of EM algorithm with nonlinear least-square optimization (EM-NLS). The Levenberg-Marquardt algorithm is used for the nonlinear optimization, and the performance of the input field estimation is close to the one obtained by Kalman smoothing.

Figures 4.9(a) and 4.9(b) show the reconstructed amplitude and the reconstructed phase scaled by the amplitude using the EM algorithm with Kalman smoothing. We can see the improvement with respect to Figure 4.3(e) and 4.3(f) which are obtained from the iterative APR. Figure 4.10(a) shows the absolute error of the intensity which is computed as

$$E_{abs} = \frac{1}{kN^2} \sum_{k}^{n} \sum_{x}^{N} \sum_{y}^{N} \left| \boldsymbol{I}_{est,k}(x,y) - \boldsymbol{I}_{k}(x,y) \right|. \tag{4.9}$$

The estimated intensity $\boldsymbol{I}_{est,k}$ is obtained by forward propagating the estimated input field $\boldsymbol{U}_{est}$ to the image plane. The EM algorithm has slightly smaller absolute intensity error then the iterative APR at $\sigma = 1\%$. We compute the MSE of the 10 estimated lens positions at every EM step as shown in Figure 4.10(b). It decreases rapidly in the beginning and approaches a constant in the end.

4.5.2 Effect of Image Noise

In the simulation we assume the image noise is dominated by the read noise and can be modeled as a Gaussian distribution with the same standard deviation among all pixels. Figure 4.11 shows the MSE of the estimated input filed

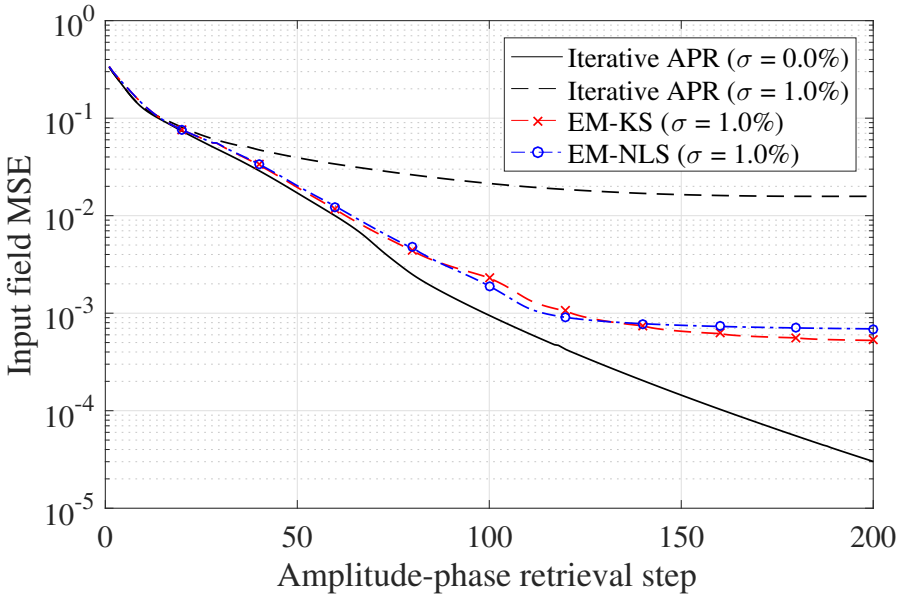

Figure 4.8: MSE of the estimated input field using the iterative APR algorithm and EM algorithm with Kalman smoothing.

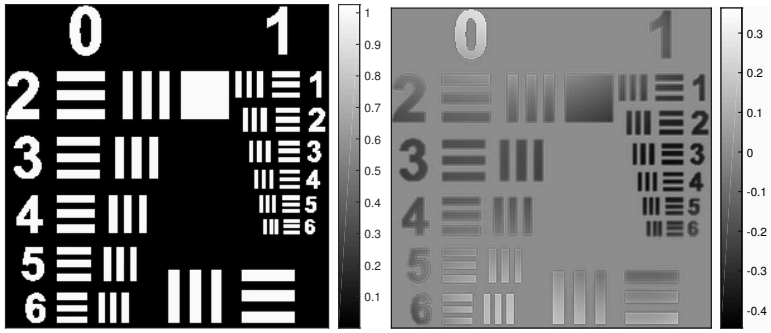

(a) (b)

Figure 4.9: Estimated fields using EM algorithm and Kalman smoothing: (a) reconstructed amplitude, and (b) reconstructed phase.

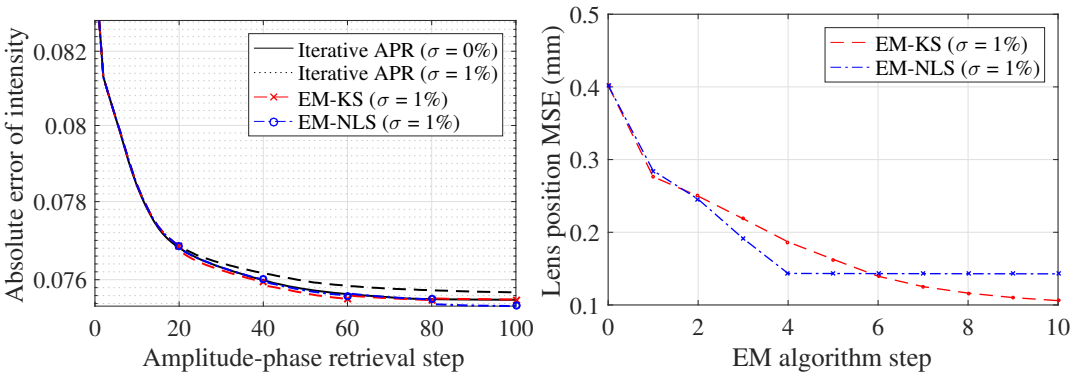

Figure 4.10: EM algorithm and Kalman smoothing estimation: (a) Absolute error of the intensity, and (b) MSE of the estimated lens position.

with $\sigma = 1\%$ and Gaussian image noise. The Gaussian noise has standard deviation 1.5% of the average intensity recorded at the image plane. Note that the APR algorithm in the M step is only an approximation for maximizing the likelihood function in the case with the Gaussian noise. With long exposure time

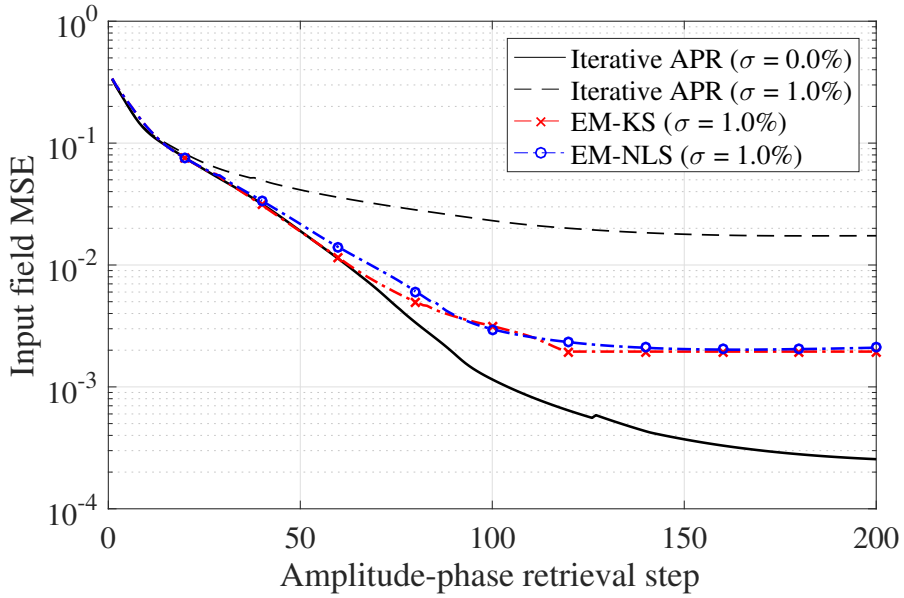

Figure 4.11: MSE of the estimated input field using the iterative APR and EM algorithm with Gaussian image noise.

the Poisson distribution of shot noise can be approximated by a Gaussian distribution with a variance equal to the number of photons arriving at the pixel. One can estimate the covariance matrix $\boldsymbol{R}_k$ with the recorded image intensity if shot noise is considered.

4.5.3 Computational Complexity

The computational complexity depends on the image size $N_p \times N_p$, the number of intensity measurements N_{l_1}, the number the EM steps N_{EM}, and the number of APR loops N_{APR} in between two EM steps. The computational cost of a 2D fast Fourier transform (FFT) and inverse FFT are both $O(N_p^2 \log N_p^2)$ for an $N_p \times N_p$ image. Both the forward and backward propagation require two FFT and two inverse FFT computation. For each EM step, IEKF requires cN_{l_1} times of forward propagation, where c is a constant depending on the iterative process in IEKF. The rest of the matrix computations in the IEKF and the smoothing process are negligible compared to the FFT computation in the forward propagation. The iterative APR requires N_{APR} times of forward and backward propagation. As a result, the EM algorithm with Kalman Smoothing takes $4N_{EM}(cN_{l_1} + 2N_{APR})$ times of FFT computation. The time to perform one EM step with $N_{l_1} = 10$ and $N_{APR} = 10$ on a 2.6 GHz and 16 GB of RAM laptop is approximately 16 seconds.

4.6 Conclusion

Iterative amplitude and phase retrieval algorithms can reconstruct an input wavefront accurately when the positions of the optical components are known

exactly. However, when a position error occurs in the optical system a proper estimation of the displacement is needed in order to produce an accurate wavefront estimation. An EM algorithm is used to simultaneously estimate the lens position and the complex field. We use the iterative APR algorithm in the M-step for complex field reconstruction and the nonlinear Kalman smoothing method in the E-step for position estimation. The MSE of the reconstructed field using the EM algorithm is much lower than using iterative APR without position estimation.

As opposed to a nonlinear least-square optimization that considers the lens positions as fixed parameters to be estimated, a Kalman smoother assumes the system is stochastic and therefore the estimation of the lens positions are uncertain. The moving lens system is treated as a hidden Markov model where the current state depends on not only the measurement, but also the previous state, and the process and measurement noise. Given enough measurements, using Kalman smoothing in the E-step makes the system more robust in the presence of image noise, as compared to NLS optimization, since the cost function in the filtering process is weighted with the process and measurement covariance matrices. In this case with only 10 intensity measurements, the Kalman smoother does not necessarily outperform the NLS optimization every time. We expect the estimation of Kalman smoother to improve when more Kalman filtering and smoothing steps are executed in a single EM step. However, the lens position step becomes smaller when collecting more intensity measurements with a limited travel range, which results in a poor estimation in the M-step since the phase diversity between images also becomes small. In the E-step the lens positions are estimated based on the input field estimated in the previous M-step. In the M-step we re-estimate the input field with the APR algorithm, which de-

pends on the prediction path of the Kalman smoother or NLS optimizer. Note that the M-step does not directly achieve a local minimum for the desired phase retrieval problem when Gaussian noise is assumed, but does achieve a local minimum of a related estimation problem. It is hard to predict which method will provide a better estimate given an arbitrary initial condition since the problem is nonlinear and non-convex.

Adding a regularization term, such as the difference between the control input and the estimated lens movement, in NLS optimization might improve its robustness to image noise. However, neither the reconstruction MSE in Kalman smoothing nor in NLS optimization approaches the value obtained without position error since the EM algorithm only guarantees a local minimum. In Kalman smoothing the state covariance gives us an estimate of the lens position error. The relationship between the input field MSE and the position error using APR algorithm can be found given the same amount of position error at each measurement [41]. Given the standard deviation of the position error, a Monte Carlo simulation can be used to estimate the input field MSE. The state covariance estimation depends on the estimate of the measurement noise covariance $\boldsymbol{R}_k$. The uncertainty of the state increases while the measurement noise covariance increases. With the growth of computing power phase retrieval algorithm has the potential to be implemented in real time. In this case the Kalman filter or other online state estimator are desired and more likely to have better estimation over time. Although the phase retrieval algorithm is perform offline, the proposed method can potentially be applied to online phase retrieval and focus diversity estimation.

CHAPTER 5

WAVEFRONT RECONSTRUCTION WITH DEFOCUS AND TRANSVERSE SHIFT ESTIMATION USING KALMAN FILTERING

5.1 Introduction

In Section 4.1 we discuss existing techniques for simultaneously estimation of system parameters and the wavefront. In this chapter we present a novel framework which is applicable to real-time implementation.

Most adaptive optics techniques solve joint estimation problems along with phase retrieval [8, 77, 78] in a nonlinear optimization framework. The unknown system variables can also be estimated using a Bayesian filtering technique. Unlike the nonlinear optimization approach which either optimizes the unknown parameters over the current measurement or uses a batch estimation after all the measurements are obtained, the Bayesian filter approach takes the past measurements into account by propagating the previous state through a state transition step and updates the estimate once a new measurement is received. The unknown states are treated as random variables and the estimation is based on the process and measurement noise statistic. A nonlinear Kalman smoother can be used with the parallel APR algorithm on an expectation-maximization (EM) framework [93].

We combine the Kalman filtering method and a serial phase retrieval algorithm to simultaneously recover the complex field and the system variables. Optimizing over the current measurement tends to overfit the data unless a proper regularization term is added to the cost function, and does not take the previous

estimates of the system parameters into account. As a result, the estimation of a Kalman filter tends to outperform those based on a single measurement alone. A batch-based estimator optimizes over all the measurements but in an offline process. With new advances in hardware, such as liquid lenses, as well as ever increasing available computing power it is now possible to implement filters for real-time operation, in cases where an online algorithm is preferred over a batch estimation.

In Section 5.2 we describe the optical model and the multiple-image phase retrieval algorithm. In Section 5.3 a nonlinear Kalman filter is applied to the phase retrieval method and is shown to successfully reduce the reconstruction error in simulation. In Section 5.4 we conduct an experiment using a translating CCD camera with error in focus diversity and transverse shifts. In each step the Kalman filter is executed prior to the phase retrieval step. A phase retrieval step is performed once the estimated defocus and transverse shifts are obtained by the filter. We show that the filtering process improves the detail and contrast of the reconstruction. Although we use a moving camera as an example the proposed method can be applied to a wide variety of optical setups that produce phase diversity, including systems with tunable lenses or deformable mirrors.

5.2 Optical model and phase retrieval

5.2.1 Phase diversity generated by a moving camera

Our system model is shown in Fig. 5.1. A collimated laser beam illuminates the test object and generates an unknown complex wavefront $\boldsymbol{U}^P(\xi, \eta)$ at the pupil

plane, where ξ and η are Cartesian coordinates. A lens with focal length f is placed at a distance of f after the object. The wavefront is focused to a CCD camera located at $(z + f)$ from the lens. The wavefront at the focal and image planes are denoted by $\boldsymbol{U}^F(x, y)$ and $\boldsymbol{U}^I(x, y)$, where x and y are the coordinates at the image plane. The optical field at the focal plane $\boldsymbol{U}^F(x, y)$ is therefore a Fourier transform of the pupil plane field $\boldsymbol{U}^P(\xi, \eta)$ written as

$$\boldsymbol{U}^F(x, y) = \frac{1}{j\lambda f}\mathcal{F}\left\{\boldsymbol{U}^P(\xi, \eta)\right\}\Big|_{f_X, f_Y}, \tag{5.1}$$

where j is the imaginary unit, $\mathcal{F}\{\}$ denotes a Fourier transforms, λ is the wavelength, $k = 2\pi/\lambda$ is the wavenumber and $f_X = \frac{x}{\lambda f}$, $f_Y = \frac{y}{\lambda f}$ are the spatial frequencies. An angular spectrum propagator is used to propagate $\boldsymbol{U}^F(x, y)$ to the defocus image planes $\boldsymbol{U}^I(x, y)$ [94]. The optical field at the image plane can be computed as

$$\boldsymbol{U}^I(x, y) = \mathcal{F}^{-1}\Big\{\mathcal{F}\{\boldsymbol{U}^F(x, y)\}A(f_X, f_Y)\Big\}, \tag{5.2}$$

where the transfer function $A(f_X, f_Y)$ is given by

$$A(f_X, f_Y) = \exp\left[jkz\sqrt{1 - (\lambda f_X)^2 - (\lambda f_Y)^2}\right]. \tag{5.3}$$

The distance z is the variable in our propagation formula. We use $\mathcal{FP}_z$ and $\mathcal{BP}_z$ to represent forward and backward propagation between the pupil and image planes.

5.2.2 Multiple-image phase retrieval algorithm

A serial phase retrieval algorithm with multiple intensity measurements is used to estimate the complex field $\hat{\boldsymbol{U}}^P$. The kth intensity measurement at the image plane is $\boldsymbol{I}_k(x, y) = |\boldsymbol{U}_k^I(x, y)|^2$. The lower dashed block in Figure 5.2 shows the

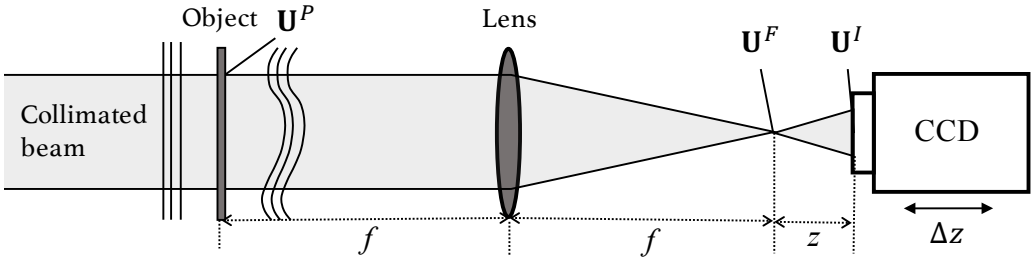

Figure 5.1: Optical model for collecting defocused images by moving the CCD camera to different positions.

flow chart of the multiple-image phase retrieval algorithm. The algorithm is initialized with a pupil plane estimate $\hat{\boldsymbol{U}}_0^P$. We obtain the estimated complex field $\hat{\boldsymbol{U}}_k^I$ at the image plane by forward propagating the previous complex field $\hat{\boldsymbol{U}}_{k-1}^P$ at the pupil plane. The estimated optical field at the image plane is given by

$$\hat{\boldsymbol{U}}_k^I = \mathcal{F}\mathcal{P}_{\hat{z}_k}\left\{\hat{\boldsymbol{U}}_{k-1}^P\right\}, \tag{5.4}$$

where $\hat{z}_k$ is the estimated distance from the focal plane to the camera at kth step. By replacing the estimated amplitude with the intensity measurement the updated optical field $\bar{\boldsymbol{U}}_k^I$ at the image plane can be computed as

$$\bar{\boldsymbol{U}}_k^I = \sqrt{\boldsymbol{I}_k}\exp\left(i\arg\left(\hat{\boldsymbol{U}}_k^I\right)\right), \tag{5.5}$$

where arg(·) operator returns the argument of a complex value. The updated field $\bar{\boldsymbol{U}}_k^I$ is back propagated to obtain the new estimated wavefront

$$\hat{\boldsymbol{U}}_k^P = \mathcal{B}\mathcal{P}_{\hat{z}_k}\left\{\bar{\boldsymbol{U}}_k^I\right\}. \tag{5.6}$$

The pupil plane $\hat{\boldsymbol{U}}_k^P$ is then passed as the initial wavefront estimate in the next loop.

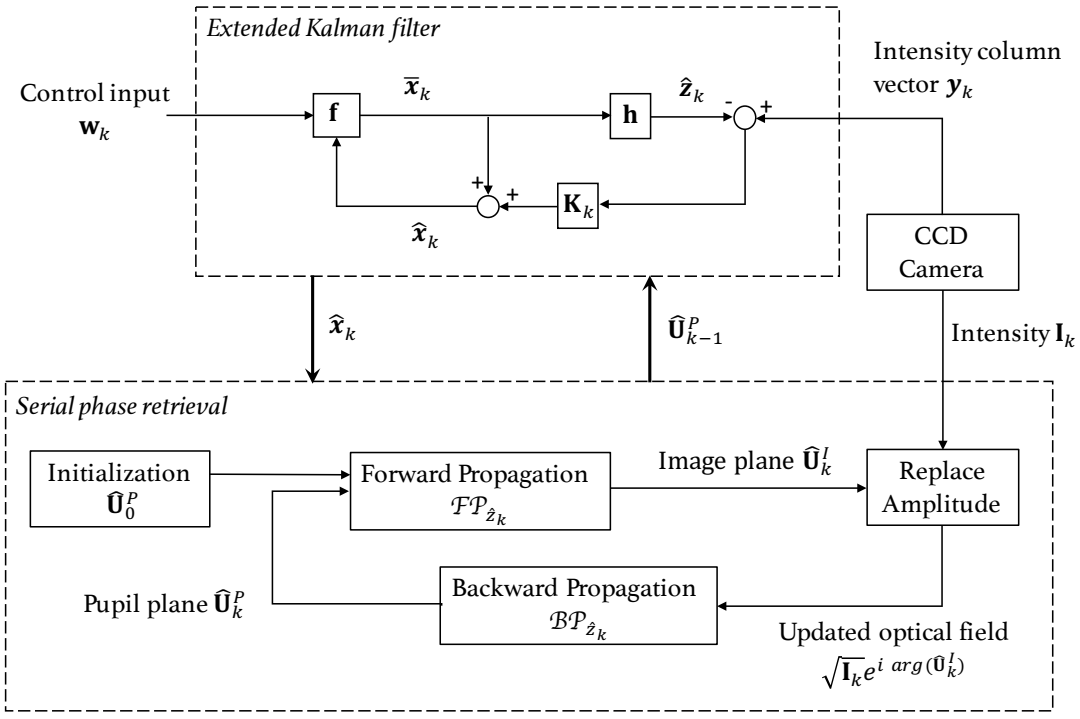

Figure 5.2: Multiple-image phase retrieval algorithm with Kalman filtering. The upper dashed block shows the operation of the EKF, and the lower dashed block is the flow chart of the multiple-image phase retrieval algorithm.

5.3 Defocus and transverse shift estimation using Kalman filtering

In this section we present the method for simultaneously estimating the unknown optical field, focus diversity, and transverse shifts of the image using an extended Kalman filter (EKF). The EKF is a nonlinear version of Kalman filter that approximates the mean and covariance of the states using local linearizations of the nonlinear systems of equations describing the state dynamics and measurement function.

The focus diversity in our system is produced by a camera mounted on a translation stage moving along the optical axis. The focus diversity represents one of the hidden state elements in the EKF since the position of the camera along the optical axis is an unknown system parameter with additional process noise. Shifts along the transverse axes x and y that occur while moving the camera from one position to another will degrade the reconstruction result. To address this, we also consider the transverse shifts, measured in units of sub-pixels, as hidden variables in our state.

5.3.1 State space model and filtering algorithm

The upper dashed block in Figure 5.2 shows the schematic of the EKF. The unknown variables to estimate at the kth step are the distance z_k and the transverse shift s_k^x and s_k^y. The vector $\boldsymbol{x}_k = [z_k, s_k^x, s_k^y]^T$ denotes the unknown state in the EKF. The 2D intensity measurement $\boldsymbol{I}_k$ can be written as a reshaped (unwrapped) column vector $\boldsymbol{y}_k$. The EKF takes in the previous estimate of the optical field $\hat{\boldsymbol{U}}_{k-1}^P$, the control input $\boldsymbol{w}_k$, and the current intensity measurement $\boldsymbol{y}_k$ to find the state estimate $\hat{\boldsymbol{x}}_k$. We assume the transverse shifts are close to their previous values, with some additional, unknown disturbances. This simplified model is a good fit for our experimental setup (see: Section 5.4), in which we use a commercial, off the shelf, motorized stage, for which the detailed dynamics and internal control loop are unknown. A more complicated model can be used if the complete mechanical behavior of the stage is known. Here the transverse shifts of the current image are the shifts of the previous image plus a Gaussian noise term.

The state transition function can be written as

$$\boldsymbol{x}_k = \boldsymbol{f}(\boldsymbol{x}_{k-1}, \boldsymbol{w}_k) + \boldsymbol{v}_k = \begin{bmatrix} z_{k-1} \\ s^x_{k-1} \\ s^y_{k-1} \end{bmatrix} + \begin{bmatrix} \Delta z_k \\ 0 \\ 0 \end{bmatrix} + \boldsymbol{q}_k, \tag{5.7}$$

where Δz_k is the control input to the camera on the translation stage and $\boldsymbol{q}_k$ is the process noise. The nonlinear measurement function is given by

$$\boldsymbol{y}_k = \boldsymbol{h}(\hat{\boldsymbol{U}}^P_{k-1}, \boldsymbol{x}_k) + \boldsymbol{r}_k = \hat{\boldsymbol{i}}_k + \boldsymbol{r}_k, \tag{5.8}$$

where $\boldsymbol{r}_k$ is the measurement noise, and $\hat{\boldsymbol{i}}_k$ is a reshaped complex column vector from the estimated intensity $\hat{\boldsymbol{I}}_k$. $\hat{\boldsymbol{I}}_k$ is obtained by performing a 2D linear interpolation on $|\hat{\boldsymbol{U}}^I_k|^2$ with transverse shifts (s^x_k, s^y_k), where $\hat{\boldsymbol{U}}^I_k = \mathcal{FP}_{z_k}\left\{\hat{\boldsymbol{U}}^P_{k-1}\right\}$. We assume both $\boldsymbol{q}_k$ and $\boldsymbol{r}_k$ are samples of zero-mean Gaussian noise with covariance $\boldsymbol{Q}_k$ and $\boldsymbol{R}_k$ respectively. The EKF consists of a state transition step followed by a measurement update. In the state transition we propagate the previous state estimate to obtain the state prior

$$\bar{\boldsymbol{x}}_k = \boldsymbol{f}(\hat{\boldsymbol{x}}_{k-1}, \boldsymbol{w}_k), \tag{5.9}$$

and the covariance prior

$$\bar{\boldsymbol{P}}_k = \boldsymbol{F}_k \hat{\boldsymbol{P}}_{k-1} \boldsymbol{F}^T_k + \boldsymbol{Q}_k, \tag{5.10}$$

where $\boldsymbol{F}_k = \frac{\partial \boldsymbol{f}}{\partial \boldsymbol{x}}\big|_{\hat{\boldsymbol{x}}_{k-1}, \boldsymbol{u}_k}$ is the Jacobian matrix of the model function $\boldsymbol{f}$, evaluated at the previous state estimate and current control input value. In this model $\boldsymbol{F}_k$ is simply an identity matrix. $\hat{\boldsymbol{P}}_{k-1}$ is the previous state covariance. In the measurement update step we use the current measurement to update the state estimate as

$$\hat{\boldsymbol{x}}_k = \bar{\boldsymbol{x}}_k + \boldsymbol{K}_k[\boldsymbol{y}_k - \boldsymbol{h}(\hat{\boldsymbol{U}}^P_{k-1}, \bar{\boldsymbol{x}}_k)] \tag{5.11}$$

with the Kalman gain

$$\boldsymbol{K}_k = \bar{\boldsymbol{P}}^T_k \boldsymbol{H}^T_k (\boldsymbol{H}_k \bar{\boldsymbol{P}}_k \boldsymbol{H}^T_k + \boldsymbol{R}_k)^{-1}, \tag{5.12}$$

where $\boldsymbol{H}_k = \frac{\partial \boldsymbol{h}}{\partial \boldsymbol{x}}\Big|_{\bar{\boldsymbol{x}}_k}$ is the Jacobian matrix of the measurement function $\boldsymbol{h}$, evaluated at the current state prior. In this thesis we use the numerical Jacobian computed by finite-difference approximations. The state perturbation in the computation is set to 10^{-6}. An alternative formula for the gain matrix, derived from a maximum a posteriori (MAP) approach, is

$$\boldsymbol{K}_k = (\bar{\boldsymbol{P}}_k^{-1} + \boldsymbol{H}_k^T \boldsymbol{R}_k^{-1} \boldsymbol{H}_k)^{-1} \boldsymbol{H}_k \boldsymbol{R}_k^{-1}. \tag{5.13}$$

This version avoids inverting $(\boldsymbol{H}_k \bar{\boldsymbol{P}}_k \boldsymbol{H}_k^T + \boldsymbol{R}_k)$, which is desirable as it represents a high-dimensional dense matrix in our case.

5.3.2 Error metric and simulation result

The parameters in the simulation are set to $f = 200$ mm and $\lambda = 635$ nm. Figures 5.3(a) and 5.3(b) show the amplitude and phase of the input object in the simulation. The simulated input wavefront is generated by creating an amplitude from a binary mask and a phase that is the combination of 10 Zernike terms with random coefficients. The side length of the mask is set as $L = 4$ mm and the detector pixel size is set to $\Delta_d = 9.1\ \mu m$. The minimum detector sampling ratio is given by $Q = \frac{\lambda f}{L \Delta_d} \approx 3.5$ which is above the Nyquist limit [95]. Figure 5.4 shows the amplitude (square root of the intensity measurement) of the optical field at the image plane. The intensity measurements are generated by simulating camera moves back and forth between -24 to 24 mm of the nominal focus position, with an 8 mm step interval. The standard deviations of the process noise are denoted by σ_z, σ_x, and σ_y. In the simulation we use $\sigma_z = 0.1$ mm, $\sigma_x = \sigma_y = 1$ pixel, and Gaussian image noise with standard deviation $\sigma_I = 1.0\%$ of the average intensity recorded at the image plane. Figures 5.3(c) and 5.3(d)

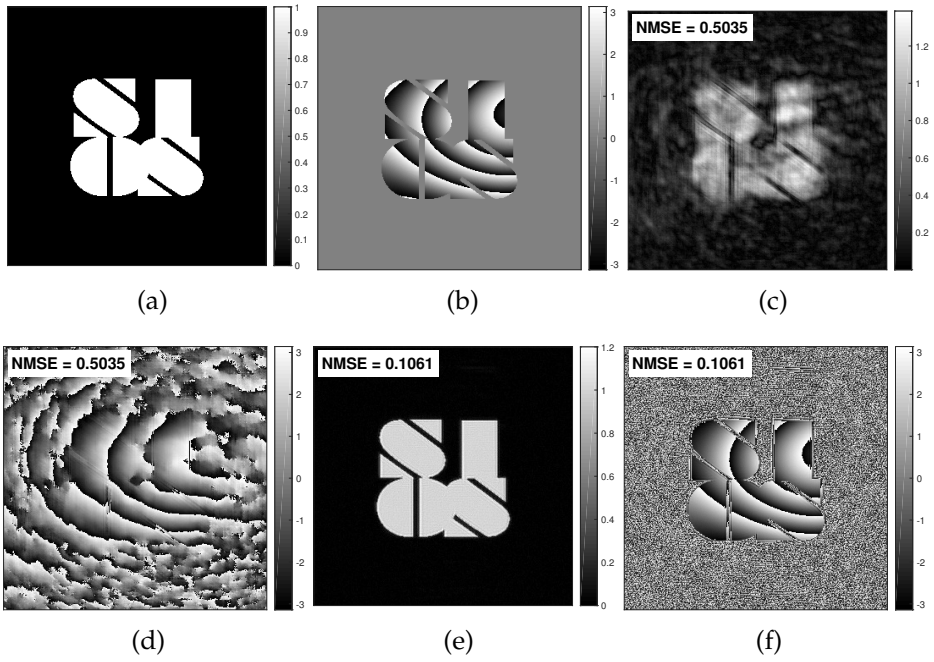

(a) (b) (c)

(d) (e) (f)

Figure 5.3: Complex fields in the simulation: (a) amplitude and (b) phase of the input field, (c) reconstructed amplitude and (d) phase with focus diversity and transverse shifts, (e) reconstructed amplitude and (f) phase using IEKF.

show the retrieved amplitude and phase of the wavefront using the multiple-image phase retrieval algorithm without the estimation of focus diversity and transverse shifts of the image. Figures 5.3(e) and 5.3(f) show the improved result with the Kalman filter estimation. In practice we use an iterated extended Kalman filter (IEKF) which improves the accuracy of the EKF by taking multiple Gauss-Newton steps during each iteration.

As the input field is known exactly in the simulation, we can define a normalized mean-squared-error (NMSE) of the estimated optical field as

$$\text{NMSE} = \min_{\phi_c} \frac{\sum_{x,y} \left| \hat{\boldsymbol{U}}^P(x,y) \exp(j\phi_c) - \boldsymbol{U}^P(x,y) \right|^2}{\sum_{x,y} |\boldsymbol{U}^P(x,y)|^2}, \tag{5.14}$$

where ϕ_c is a constant phase. The NMSE is computed using the value for ϕ_c

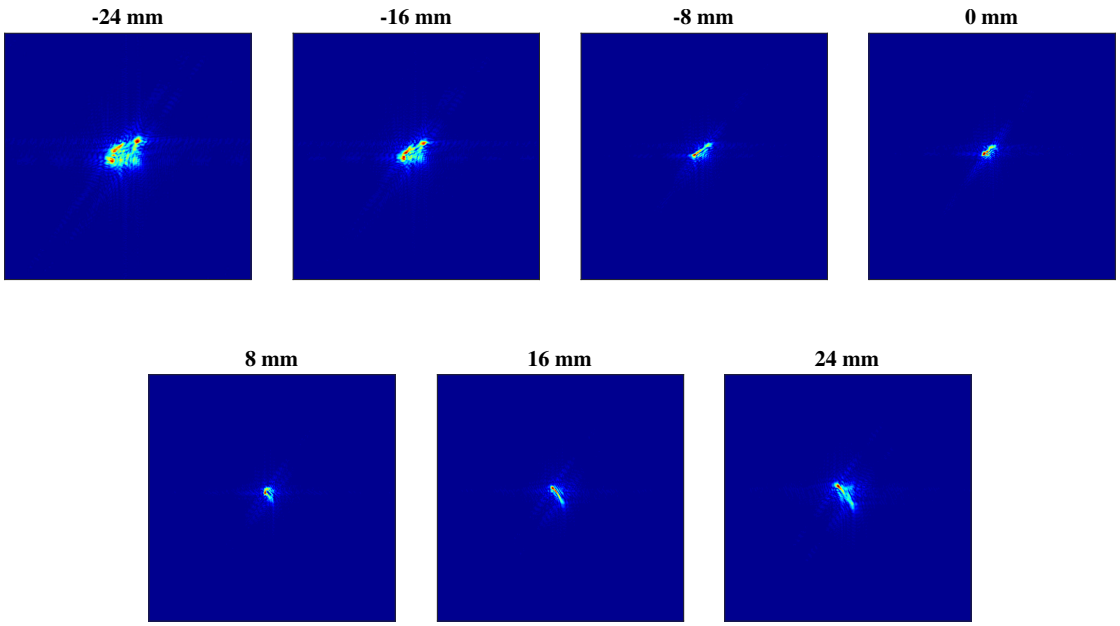

Figure 5.4: Amplitude of the optical field at the image plane.

that minimizes the error since the algorithm is insensitive to the phase offset [86]. Figure 5.5 shows the NMSE with and without the IEKF estimation. The IEKF estimation starts after 50 steps of the general phase retrieval algorithm. This gives us a proper complex field $\hat{\boldsymbol{U}}^P$ to initialize the estimation and reduces the possibility of converging to a bad local minimum. The blue circle line in Figure 5.5 shows that the algorithm is very sensitive to the position error. The red cross line shows that the IEKF estimation improves the NMSE result and remains stable after many steps. Table 5.1 shows the average NMSE of the last 20 steps with image noise varying from $\sigma_I = 0$ to 5%. The IEKF estimation is shown to improve the NMSE results under different levels of image noise.

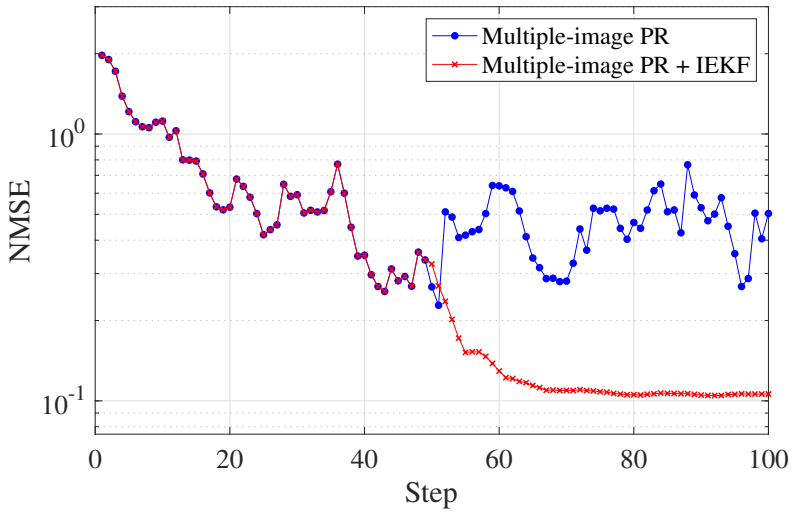

Figure 5.5: NMSE as defined in Eq. 5.14 for simulations with and without the IEKF estimation.

Table 5.1: Average NMSE of the last 20 steps at different image noise level.

	$\sigma_I = 0\%$	$\sigma_I = 1\%$	$\sigma_I = 2\%$	$\sigma_I = 5\%$
Multiple-image PR	0.4922	0.4948	0.5028	0.5324
Multiple-image PR + IEKF	0.0878	0.1058	0.1045	0.1144

5.4 Experiment

5.4.1 Test objects and experimental setup

In this section we present experimental results of the serial phase retrieval with IEKF. Figure 5.6 shows the experimental setup for the layout in Figure 5.1. A 635 nm laser beam passes through a customized collimator to produce a collimated beam, and a neutral density (ND) filter is installed after the collimator to reduce the power of the beam. A test object in the beam produces the wavefront to

be estimated, which is focused by a 200 mm lens. A CCD camera with pixel size $\Delta_d = 4.54\ \mu m$ is mounted on a translation stage for adjusting the defocus z_k within a 25 mm range.

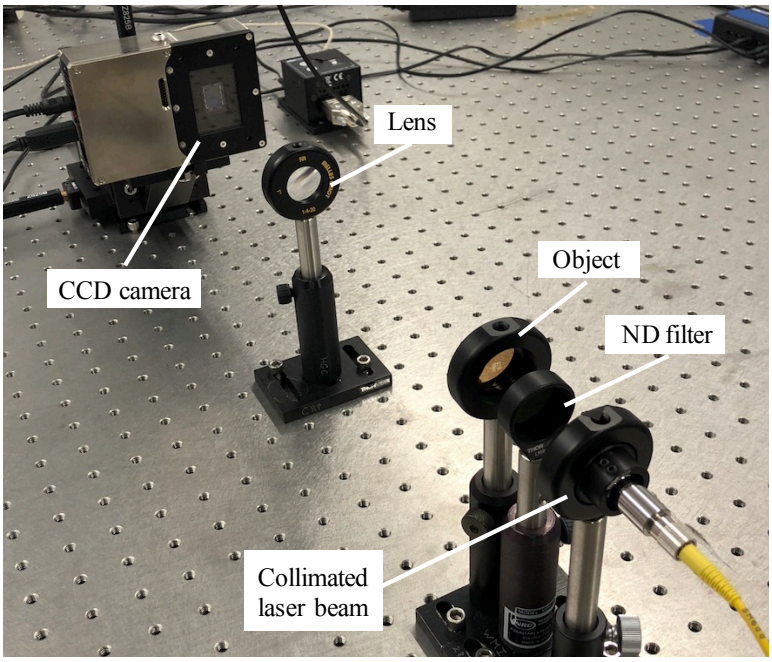

Figure 5.6: Experimental setup for wavefront retrieval.

Figure 5.7 show the two test objects used. The first test object is a Thorlabs resolution test target R1DS1N illuminated by the collimated beam. The second test object is a laser cut aperture with acronym SIOS and a phase component produced by a lens (Thorlabs LA1464-A) with an effective focal length (EFL) of 1000 mm and a back focal length (BFL) of 995.3 mm.

5.4.2 Results

The intensity measurement at the image plane using the Thorlabs resolution test target are shown in Figure 5.8. Figure 5.9 shows the phase retrieval result

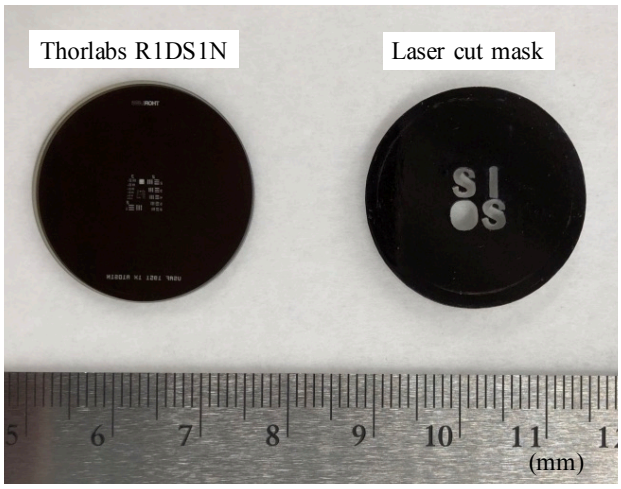

Figure 5.7: Mask of the test object.

of the Thorlabs resolution test target produced by translating the camera back and forth at $z_k = \{-12, -8, -4, 0, 4, 8, 12\}$ mm. Figure 5.9(a) and 5.9(b) are the amplitude and phase without using IEKF for defocus and transverse shift estimation. Figure 5.9(c) and 5.9(d) shows an improved reconstruction result using the IEKF. The retrieved amplitude with the IEKF is closer to the ground truth of the aperture. There appears to be a tilted wavefront in the retrieved phase. This mainly corresponds to the relative tilt between the collimated beam and the camera, and the remaining errors in transverse shift estimation also have a small effect on the detected tilted wavefront.

The intensity measurement at the image plane using the SIOS target are shown in Figure 5.10. Figure 5.11 shows the phase retrieval result of the laser cut SIOS target with a phase component produced by a convex lens. Figures 5.11(a) and 5.11(b) show the amplitude and phase result without the IEKF, and Figures 5.11(c) and 5.11(d) are those with the IEKF. The results show an obvious visual improvement when using the IEKF algorithm. Since the phase retrieved from the algorithm only returns values in the range $(-\pi, \pi]$, an unwrapping op-

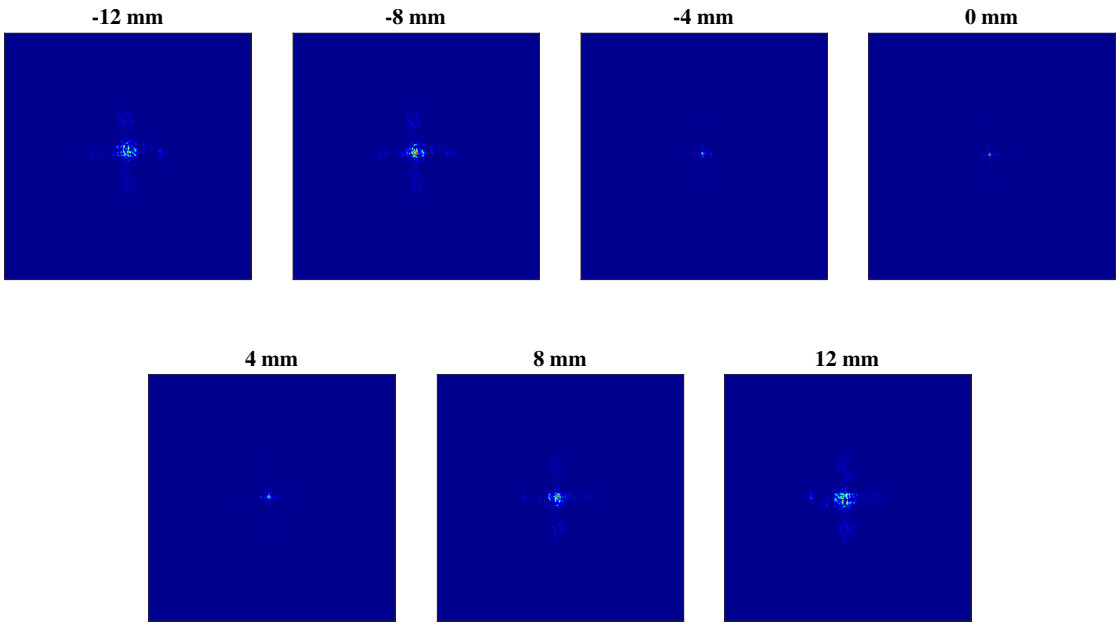

Figure 5.8: Intensity measurement of the Thorlabs resolution target at the image plane.

eration is required to remove the discontinuous 2π jumps. We use the Goldstein branch cut algorithm [96, 97, 98] for phase unwrapping.

Goldstein branch cut algorithm

The discrete formula of two-dimensional phase unwrapping can be written as

$$\psi(i, j) = \mathcal{W}\{\phi(i, j)\} = \phi(i, j) + 2\pi t, \tag{5.15}$$

where $\mathcal{W}\{\}$ is the wrapping operator, t is an integer, and $\psi(i, j)$ and $\phi(i, j)$ are the wrapped and unwrapped phase values at pixel (i,j). We wish to determine the unwrapped phase $\phi(i, j)$ given $\phi(i, j) \in (-\pi, \pi]$.

We could found different answers if we follow two different paths in the phase unwrapping procedure. These inconsistencies are called residues in the

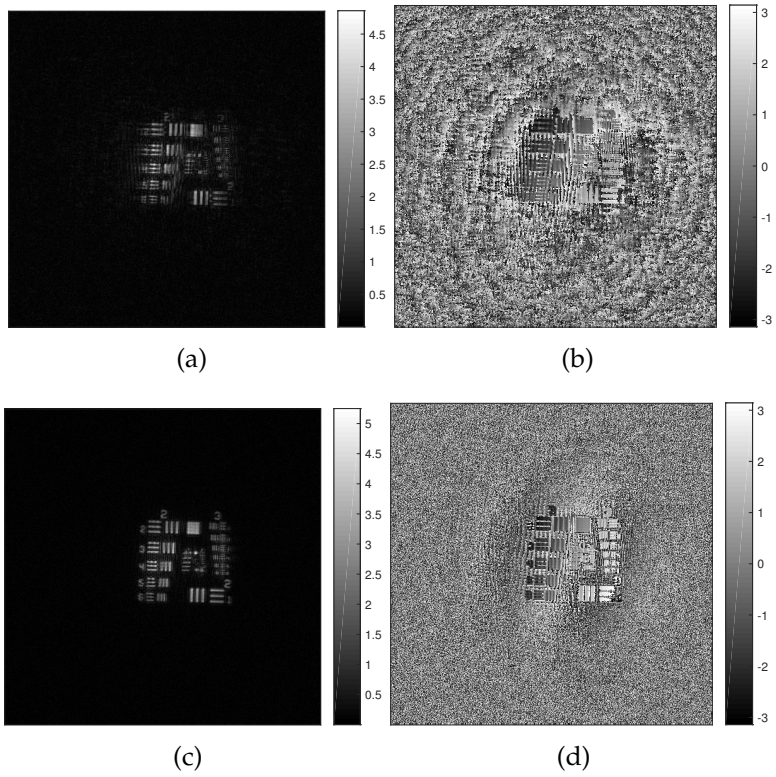

Figure 5.9: Experimental results of the Thorlabs resolution test target. (a) and (b) are the amplitude and phase without IEKF, and (c) and (d) show the results with IEKF.

unwrapping problem [97]. The residue q can be computed by summing the phase differences around the closed path of 4 adjacent pixels

$$q = \sum_{i=1}^{4} \Delta_i, \tag{5.16}$$

where

$$\begin{aligned} \Delta_1 &= \mathcal{W}\{\psi(i, j+1) - \psi(i, j)\} \\ \Delta_2 &= \mathcal{W}\{\psi(i+1, j+1) - \psi(i, j+1)\} \\ \Delta_3 &= \mathcal{W}\{\psi(i+1, j) - \psi(i+1, j+1)\} \\ \Delta_4 &= \mathcal{W}\{\psi(i, j) - \psi(i+1, j)\} \end{aligned} \tag{5.17}$$

The phase can be unwrapped along any path if there are no residues. Otherwise, branch cuts need be placed to balance the residues [97]. The Goldstein branch

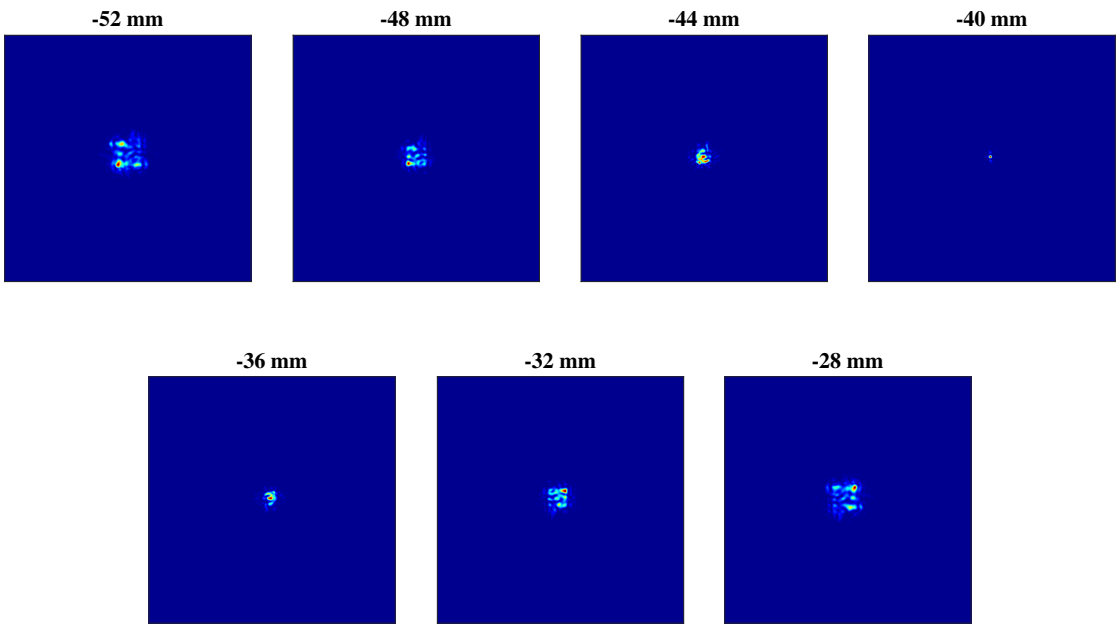

Figure 5.10: Intensity measurement of the SIOS target at the image plane.

cut algorithm is one of the path-following methods which generates optimal branch cuts. After identifing the residues and generating the branch cuts, the algorithm performs path integration around the branch cuts.

Figure 5.12 shows the unwrapped phase of Figure 5.11(d). Figure 5.12(a) shows the unwrapped phase in a heatmap. The pixels with zero values either have amplitude below a certain threshold or represent the branch cut pixels. Figure 5.12(b) shows the unwrapped phase in a 3D surface plot. The recovered focal length of the phase component is 997.6 mm which is within the tolerance (±1% of the BFL) provided by the manufacturer. Other factors that affect the result are the gap between the mask and the lens (<1mm) and the actual distance between the object and the 200 mm focusing lens, which may be slightly offset from the nominal focus length.

Figure 5.13 shows an interesting test using a transparent paper with a

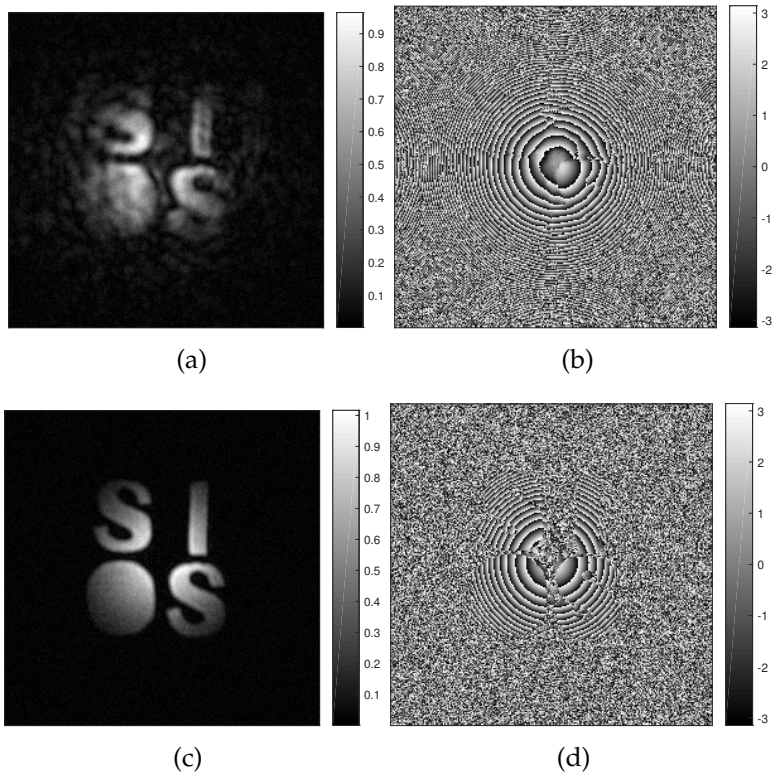

Figure 5.11: Experimental results of the laser cut mask with phase component. (a) and (b) show the result of amplitude and phase without IEKF, and (c) and (d) show the those with IEKF.

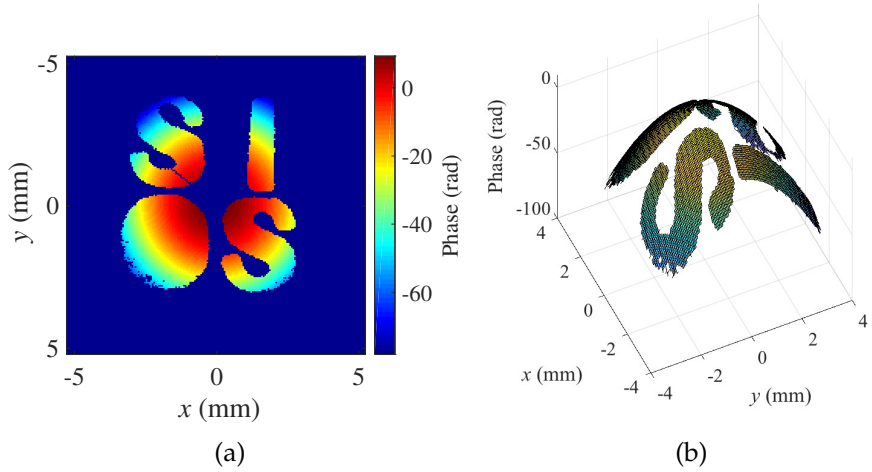

Figure 5.12: Unwrapped phase at the pupil plane. Both (a) heatmap and (b) surface plot are included.

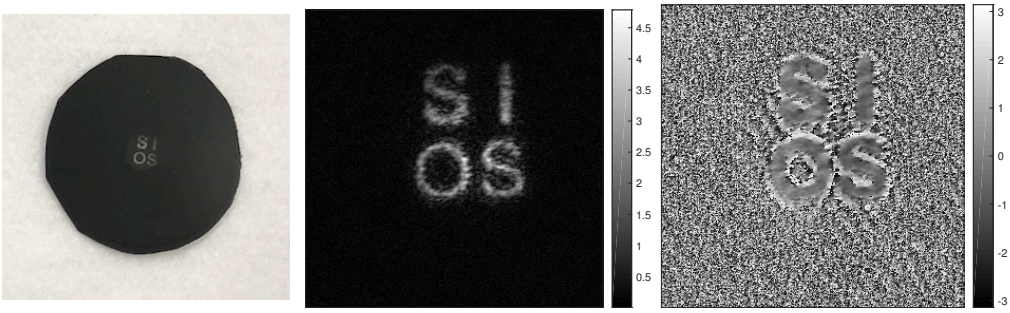

(a) (b) (c)

Figure 5.13: Experimental results of the SIOS logo printed on a transparent paper. (a) shows the printed logo mask, and (b) and (c) show the result of amplitude and phase using IEKF.

printed logo. Figure 5.13(a) show the printed SIOS logo. Figure 5.13(b) and 5.13(c) show the result of amplitude and phase using IEKF. Both the retrieval amplitude and phase looks blurry compared to the laser cut mask. This reflects the non-homogeneous properties in the transparent material and the limited precision of the paint.

Defocus and transverse shift estimation

Figure 5.14 show the stage commands and the difference between the estimate and the command (i.e. $\hat{z}_k - \sum_{i=1}^{k} \Delta z_k$). The figure does not indicate the error of the estimate since the true state is unknown, but it gives us a rough idea of the stage behavior. We can see the estimate capture the periodic pattern of the commercial stage, and the estimate indicate the overall camera position drifts slightly after 120 steps.

Figure 5.15(a) and 5.15(b) shows the estimate of $\hat{s}_x$ and $\hat{s}_y$ in subpixel. The x axis in the plot is the estimated camera position $\hat{z}_k$. The smaller (darker) dots represent the early steps and the larger (brighter) dots are the later steps. We

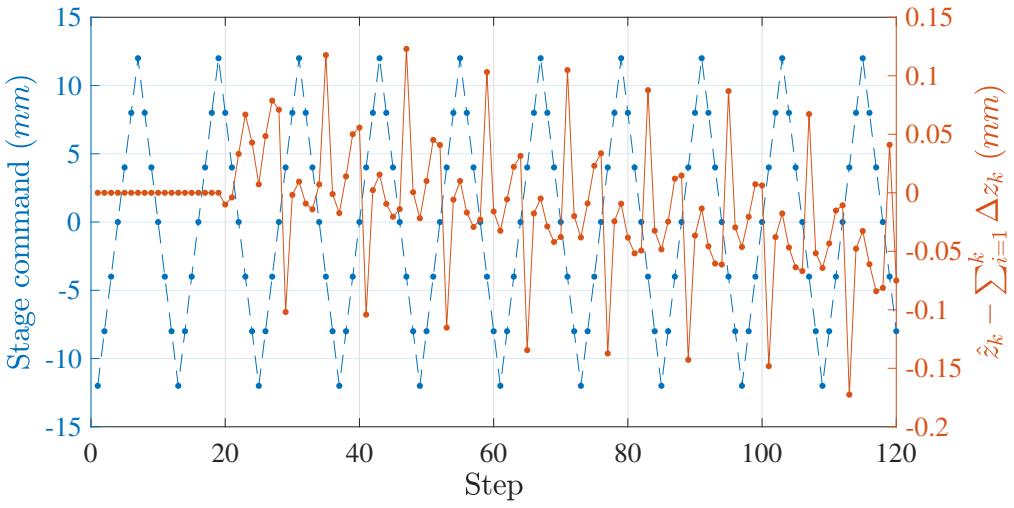

Figure 5.14: Stage commands and the difference between the estimate $\hat{z}_k$ and the command.

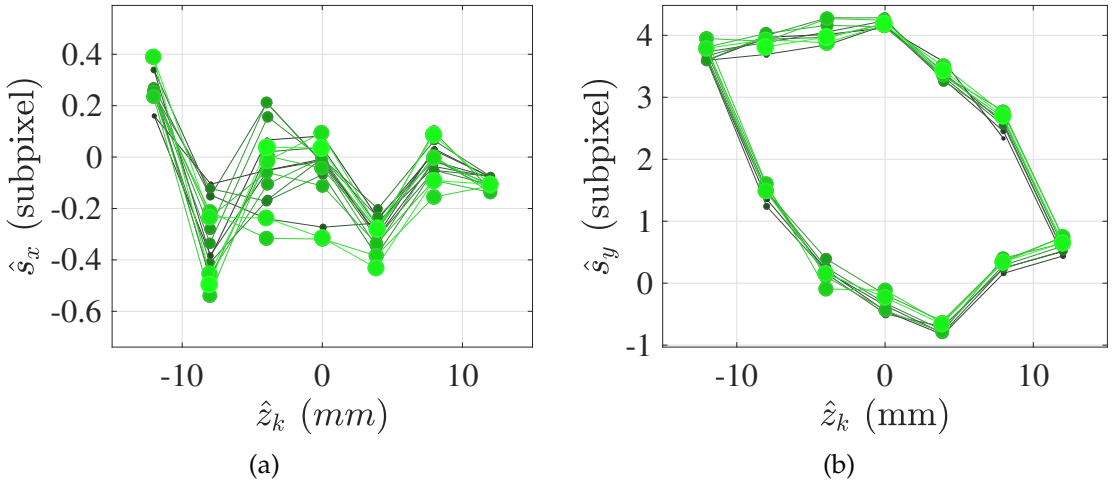

Figure 5.15: Transverse shift estimate $\hat{s}_x$ and $\hat{s}_y$.

can see that $\hat{s}_x$ varies within 1 pixel, but $\hat{s}_y$ has high variation and an obvious periodic pattern. This is caused by the torque produced by the weight of the mounted camera.

These figures show that the simple model in Equation 5.7 does not fully capture the behavior and dynamic of the commercial stage. However, the iterative process in the IEKF improve the convergency and return the estimates that cap-

ture part of the stage behavior. A more representative model can be used if the system parameters are known.

5.5 Conclusion

In summary, we present a novel method which applies stochastic filtering techniques to estimate system variables in a serial phase retrieval process. The iterated extended Kalman filter is used for online estimation of the defocus and transverse shifts in an optical system with a moving camera. We show that the IEKF successfully improves the quality of the reconstructed wavefront and reduces the NMSE in simulation. The proposed algorithm is used to recover the wavefront in an experiment where two different objects are tested. The IEKF approach enhances the details of the reconstruction. The retrieved amplitude and phase with the IEKF appears to be more representative of the true wavefront at the pupil plane than the ones using a standard phase retrieval algorithm. We introduce a non-trivial phase component by adding a convex lens right before the binary mask. The estimated focal length of the lens is obtained by unwrapping the phase and the result agrees with the value given by the manufacturer.

Our method can be applied to many different optical systems that have unknown system variables, and especially when these variables can only be observed indirectly. Some applications replace the translation stage with a focus tunable lens to speed up the image acquisition process [43, 99]. The focal length of an electrically tunable lens is adjusted by applying a current to the actuator. Instead of using a fixed look-up table obtained offline, the focal length can be estimated online using a system model that considers the probability distribu-

tion of noise and disturbances. Some systems use a deformable mirror or digital micro-mirror device (DMD) for real-time wavefront reconstruction [44, 23] where an online filtering algorithm is preferred. Many other methods that generate phase diversity (e.g. oblique illuminations [100], transverse translation diversity [71]) involve uncertain variables that can also be incorporated in our online estimators.

CHAPTER 6

CONCLUSIONS

6.1 Summary

The research presented in this thesis has demonstrated advances in estimation and control of self-aligning optical systems, simultaneous system parameter estimation in phase retrieval methods, and their application towards real-time reconstruction and alignment using focal plane sensing. The contribution are summarized below:

Automated alignment. The main purpose of the alignment task is to avoid dedicated wavefront sensors, which are expensive and produces throughput lost and non-common path error. In chapter 2 we start with a simple alignment task using image feature detection at the focal plane, and prove the automated alignment concept with a single lens and low degrees of freedom system. In chapter 4 we demonstrate an advanced self-aligning method using focal plane sensing. We utilized principle component decomposition to extract useful measurements at the focal plane, build nonlinear observer is the simulation, and implemented iterated extended Kalman filter and unscented Kalman filter for real time estimation and control in SIOS Optics Lab. The observability of the system is analyzed and discussed in the simulation, and a further application for reflective optical system using an off-axis parabolic mirror is demonstrated. We successfully prove that the automated alignment task can be done without adding an additional wavefront sensor as most of the current technology does, and instead use the existing camera in the system.

Phase retrieval. The goal of developing phase retrieval algorithm in this thesis is to minimize the reconstruction error caused by the error of the system variables. In chapter 4 we present a novel method with combine the parallel phase retrieval framework with Bayesian filtering techniques. The well-known EM algorithm is applied in the alternating optimization process. In chapter 5 we use serial phase retrieval algorithm (multi-image phase retrieval) with Kalman filtering. The major contribution of our method is the online estimation framework which is preferred over a batch estimation in real time application, and the fact that the filter takes into account the model of the system, the process and measurement noise statistic. We successfully proves the improvement on the reconstructed wavefront in the experiment.

SIOS Optics Lab. All the experiments carried out in this thesis are the first set of experiments in the SIOS Optics Lab. This includes setting up the camera system, laser source, motorized stages, writing MATLAB interfaces to communicate with the hardware, and selecting optical components for future use. This works accelerate the potential future experiments in the SIOS Optics Lab.

6.2 Future Work

There are several directions that the work in this thesis can be expanded and further developed. In the alignment work many different image information retrieval methods and observer models, such as independent component analysis (ICA) and convolution neural network (CNN), can be developed. ICA finds directions in the feature space corresponding to projections with non-Gaussian signals, which can better separate the noise and the useful signal in an exper-

imental image. With a large amount of data, a CNN which maps the images directly to the misalignments can be learned. However, two or more images are required to produce the diversity at the image plane. There are many other filtering algorithms that have the potential to improve the estimation process. For example, using the Ensemble Kalman filter (EnKF) which is a Monte Carlo approximation of Kalman filter, or a particle filter which is more computational expensive but might perform better when non-Gaussian noise presents. The fundamental methodology developed in this thesis can be extended to high dimension optical systems using a systematic approach. Our automated alignment method can be used to align the optical components in subsystems, and an overall alignment among subsystems can be carried out with the same method after the first step is completed. Last but not least, phase retrieval algorithms can be applied in real time if advanced hardware, such as high speed focus tunable lens and deformable mirror, is used, and high computational power is available. Spatial light modulator (SLM) can be used to generate dynamic phase to evaluate the performance of the algorithm. There many other researches that focus on focal plane sensing can be incorporated to the methods we developed.

APPENDIX A

NONLINEAR KALMAN FILTERING

An nonlinear discrete-time system

$$\boldsymbol{x}_{k+1} = \boldsymbol{f}(\boldsymbol{x}_k, \boldsymbol{u}_k, \boldsymbol{w}_k) \tag{A.1}$$

$$\boldsymbol{y}_k = \boldsymbol{h}(\boldsymbol{x}_k, \boldsymbol{v}_k) \tag{A.2}$$

where $\boldsymbol{x}_k \in \mathbb{R}^{n_x}$ is the state, $\boldsymbol{u}_k \in \mathbb{R}^{n_u}$ is the control input, and $\boldsymbol{y}_k \in \mathbb{R}^{n_y}$ is the measurement. Moreover, $\boldsymbol{w}_k \in \mathbb{R}^{n_w}$ and $\boldsymbol{v}_k \in \mathbb{R}^{n_v}$ are the disturbance and measurement noise. Both $\boldsymbol{w}_k$ and $\boldsymbol{v}_k$ are zero mean while noise, i.e.,

$$\mathbb{E}[\boldsymbol{v}_k] = 0, \quad \mathbb{E}[\boldsymbol{v}_k \boldsymbol{v}_j^T] = \delta_{kj} \boldsymbol{Q}_k \tag{A.3}$$

$$\mathbb{E}[\boldsymbol{w}_k] = 0, \quad \mathbb{E}[\boldsymbol{w}_k \boldsymbol{w}_j^T] = \delta_{kj} \boldsymbol{R}_k \tag{A.4}$$

A.1 Extended Kalman filter

The extended Kalman filter (EKF) consists of two steps where one is state transition and the other is measurement update. We assume the ground true of state $\boldsymbol{x}_k$ and the disturbance are close to $\hat{\boldsymbol{x}}$ and $\mathbb{E}[\boldsymbol{v}_k] = 0$, and use Taylor series expansion to estimation the state prior. In the state transition step the state estimate prior is given by

$$\bar{\boldsymbol{x}}_{k+1} = \boldsymbol{f}(\hat{\boldsymbol{x}}_k, \boldsymbol{u}_k, 0), \tag{A.5}$$

and the error covariance prior is

$$\bar{\boldsymbol{P}}_{k+1} = \boldsymbol{F}_k \hat{\boldsymbol{P}}_k \boldsymbol{F}_k^T + \boldsymbol{Q}_k, \tag{A.6}$$

where $\hat{\boldsymbol{P}}_k$ is the previous state error covariance. The Jacobian of the model function is

$$\boldsymbol{F}_k = \frac{\partial \boldsymbol{f}}{\partial \boldsymbol{x}}(\hat{\boldsymbol{x}}_k, \boldsymbol{u}_k, 0) \tag{A.7}$$

In the measurement update step we use the current measurement to update the state estimate

$$\hat{\boldsymbol{x}}_k = \bar{\boldsymbol{x}}_k + \boldsymbol{K}_k[\boldsymbol{y}_k - \boldsymbol{h}(\bar{\boldsymbol{x}}_k)] \tag{A.8}$$

with the Kalman gain

$$\boldsymbol{K}_k = \bar{\boldsymbol{P}}_k^T \boldsymbol{H}_k^T (\boldsymbol{H}_k \bar{\boldsymbol{P}}_k \boldsymbol{H}_k^T + \boldsymbol{R}_k)^{-1}, \tag{A.9}$$

where the Jacobian matrix of the measurement function $\boldsymbol{h}$ is

$$\boldsymbol{H}_k = \frac{\partial \boldsymbol{h}}{\partial \boldsymbol{x}}(\bar{\boldsymbol{x}}_k, \boldsymbol{0}). \tag{A.10}$$

An alternative formula for the gain matrix derived from a maximum a posteriori (MAP) perspective is

$$\boldsymbol{K}_k = (\bar{\boldsymbol{P}}_k^{-1} + \boldsymbol{H}_k^T \boldsymbol{R}_k^{-1} \boldsymbol{H}_k)^{-1} \boldsymbol{H}_k \boldsymbol{R}_k^{-1}. \tag{A.11}$$

This avoids inverting $(\boldsymbol{H}_k \bar{\boldsymbol{P}}_k \boldsymbol{H}_k^T + \boldsymbol{R}_k)$ which is sometimes a high-dimensional dense matrix.

Iterated extended Kalman filter

The iterated extended Kalman filter (IEKF), which is more is more computational expensive than the EKF, improve the convergence of the EKF by taking multiple Gauss-Newton steps during each filter iteration. The state transition step in the IEKF remains the same at the EKF. The Gauss-Newton steps are taken in the measurement update step until converging to the local minimum.

$\hat{\boldsymbol{x}}_{k+1}^{i}$ is the state estimate at the ith Gauss-Newton iteration. Each measurement update step is initialized by $\hat{\boldsymbol{x}}_{k+1}^{0} = \bar{\boldsymbol{x}}_{k+1}$. When deriving the EKF using MAP the resulting cost function at step $k+1$ is

$$\begin{aligned} J_c(\boldsymbol{x}_{k+1}) = & \frac{1}{2}(\boldsymbol{x}_{k+1} - \bar{\boldsymbol{x}}_{k+1})^T \bar{\boldsymbol{P}}_{k+1}^{-1}(\boldsymbol{x}_{k+1} - \bar{\boldsymbol{x}}_{k+1}) \\ & + \frac{1}{2}\left[\boldsymbol{y}_{k+1} - \boldsymbol{h}(\boldsymbol{x}_{k+1})\right]^T \boldsymbol{R}_{k+1}^{-1}\left[\boldsymbol{y}_{k+1} - \boldsymbol{h}(\boldsymbol{x}_{k+1})\right]. \end{aligned} \tag{A.12}$$

By linearizing the equation about $\hat{\boldsymbol{x}}_{k+1}^{i}$ one can get the IEKF algorithm shown in Algorihtm 1. The α and i_{max} in the algorithm can be chosen based on the application.

A.2 Unscented Kalman filter

The unscented Kalman filter (UKF), which is also known as sigma points filter, is used to address two issues in EKF and IEKF. One is the suboptimal estimation while neglecting higher order term when using the Taylor expansions. The other is the difficulty for deriving analytical expression for the Jacobian of function $\boldsymbol{f}$ and $\boldsymbol{h}$. The sigma point filter generates a cluster of points in a hypervolume space. The Cholesky factorization of the error and disturbances covariance matrix are

$$\boldsymbol{S}_k^x(\boldsymbol{S}_k^x)^T = \boldsymbol{P}_k \tag{A.13}$$

$$\boldsymbol{S}_k^v(\boldsymbol{S}_k^v)^T = \boldsymbol{Q}_k \tag{A.14}$$

where the Cholesky factors are

$$\boldsymbol{S}_k^x = [\boldsymbol{s}_{k,1}^x, \boldsymbol{s}_{k,2}^x, ..., \boldsymbol{s}_{k,n}^x] \tag{A.15}$$

$$\boldsymbol{S}_k^v = [\boldsymbol{s}_{k,1}^v, \boldsymbol{s}_{k,2}^v, ..., \boldsymbol{s}_{k,q}^v]. \tag{A.16}$$

Algorithm 1: Iterated extended Kalman filter (IEKF)

Initialize $\hat{\boldsymbol{x}}_0$, $\boldsymbol{P}_0$;

for $k = 0$ *to* N_{step} **do**

$\bar{\boldsymbol{x}}_{k+1} = \boldsymbol{f}(\hat{\boldsymbol{x}}_k, \boldsymbol{u}_k, \boldsymbol{0})$;

$\bar{\boldsymbol{P}}_{k+1} = \boldsymbol{F}_k \hat{\boldsymbol{P}}_k \boldsymbol{F}_k^T + \boldsymbol{Q}_k$;

Measure $\boldsymbol{y}_{k+1}$;

Set $i = 0$;

while $i < i_{max}$ **do**

$\hat{\boldsymbol{x}}_{k+1}^i = \bar{\boldsymbol{x}}_{k+1}$;

$\boldsymbol{H}_{k+1}^i = \dfrac{\partial \boldsymbol{h}}{\partial \boldsymbol{x}}\Big|_{\hat{\boldsymbol{x}}_{k+1}^i}$;

$\boldsymbol{P}_{k+1}^i = \left(\bar{\boldsymbol{P}}_{k+1}^{-1} + {\boldsymbol{H}_{k+1}^i}^T \boldsymbol{R}_{k+1}^{-1} \boldsymbol{H}_{k+1}^i\right)^{-1}$;

Set $\alpha = 1$;

while $\alpha > \alpha_{min}$ **do**

$$\hat{\boldsymbol{x}}_{k+1}^{i+1} = \hat{\boldsymbol{x}}_{k+1}^i + \alpha \boldsymbol{P}_{k+1}^i \boldsymbol{H}_{k+1}^i \boldsymbol{R}_{k+1}^{-1} \left[\boldsymbol{y}_{k+1} - \boldsymbol{h}(\hat{\boldsymbol{x}}_{k+1}^i)\right] + \alpha \boldsymbol{P}_{k+1}^i \bar{\boldsymbol{P}}_{k+1}^{-1} (\bar{\boldsymbol{x}}_{k+1} - \hat{\boldsymbol{x}}_{k+1}^i);$$

if $J_c(\hat{\boldsymbol{x}}_{k+1}^{i+1}) > J_c(\hat{\boldsymbol{x}}_{k+1}^i)$ **then**

$\alpha = \alpha/2$;

else

break while loop;

end

end

end

end

The $\boldsymbol{s}^x_{k,i}$ and $\boldsymbol{s}^v_{k,i}$ are the ith vector of $\boldsymbol{S}^x_k$ and $\boldsymbol{S}^v_k$. We generate $2(n_x + n_v) + 1$ sigma points as the following

$$\begin{bmatrix} \boldsymbol{x}^i_k \\ \boldsymbol{v}^i_k \end{bmatrix} = \begin{bmatrix} \begin{bmatrix} \hat{\boldsymbol{x}}_k \\ \mathbf{0} \end{bmatrix} & i = 0 \\ \begin{bmatrix} \hat{\boldsymbol{x}}_k + \sqrt{n_x + n_v + \gamma}\, \boldsymbol{s}^x_{k,i} \\ \mathbf{0} \end{bmatrix} & i \in \{1, ..., n_x\} \\ \begin{bmatrix} \hat{\boldsymbol{x}}_k - \sqrt{n_x + n_v + \gamma}\, \boldsymbol{s}^x_{k,(i-n_x)} \\ \mathbf{0} \end{bmatrix} & i \in \{n_x + 1, ..., 2n_x\} \\ \begin{bmatrix} \hat{\boldsymbol{x}}_k \\ \sqrt{n_x + n_v + \gamma}\, \boldsymbol{s}^v_{k,(i-2n_x)} \end{bmatrix} & i \in \{2n_x + 1, ..., 2n_x + n_v\} \\ \begin{bmatrix} \hat{\boldsymbol{x}}_k \\ -\sqrt{n_x + n_v + \gamma}\, \boldsymbol{s}^v_{k,(i-2n_x-n_v)} \end{bmatrix} & i \in \{2n_x + n_v + 1, ..., 2(n_x + n_v)\} \end{bmatrix}. \quad \text{(A.17)}$$

The subscript i and k are the ith sigma point and kth step in the UKF. γ can be computed from the tuning parameters in the UKF

$$\gamma = \alpha^2(n_x + n_v + \kappa) - (n_x + n_v), \quad \text{(A.18)}$$

where $\alpha \in \{10^{-4}, 1\}$ and $\kappa \in \{0, 3 - n_x - n_v\}$. These sigma points are propagated through the dynamics and measurement functions

$$\bar{\boldsymbol{x}}^i_{k+1} = \boldsymbol{f}(\boldsymbol{x}^i_k, \boldsymbol{u}_k, \boldsymbol{v}^i_k) \quad \text{(A.19)}$$

$$\bar{\boldsymbol{y}}^i_{k+1} = \boldsymbol{h}(\bar{\boldsymbol{x}}^i_{k+1}, \mathbf{0}) \quad \text{(A.20)}$$

The state and measurement prior can be computed as

$$\bar{\boldsymbol{x}}_{k+1} = \sum_{i=0}^{2(n_x+n_v)} \omega^i_m \bar{\boldsymbol{x}}^i_{k+1} \quad \text{(A.21)}$$

$$\bar{\boldsymbol{y}}_{k+1} = \sum_{i=0}^{2(n_x+n_v)} \omega^i_m \bar{\boldsymbol{y}}^i_{k+1}, \quad \text{(A.22)}$$

where the weights are given by

$$\omega_m^i = \begin{cases} \frac{\gamma}{n_x+n_v+\gamma} & i = 0 \\ \frac{1}{2(n_x+n_v+\gamma)} & i \in \{1, ..., 2(n_x + n_v) \end{cases} \tag{A.23}$$

The prior covariances matrices are

$$\bar{\boldsymbol{P}}_k = \sum_{i=0}^{2(n_x+n_v)} \omega_c^i \left(\bar{\boldsymbol{x}}_{k+1}^i - \bar{\boldsymbol{x}}_{k+1}\right)\left(\bar{\boldsymbol{x}}_{k+1}^i - \bar{\boldsymbol{x}}_{k+1}\right)^T \tag{A.24}$$

$$\bar{\boldsymbol{P}}_{\boldsymbol{xy},k+1} = \sum_{i=0}^{2(n_x+n_v)} \omega_c^i \left(\bar{\boldsymbol{x}}_{k+1}^i - \bar{\boldsymbol{x}}_{k+1}\right)\left(\bar{\boldsymbol{y}}_{k+1}^i - \bar{\boldsymbol{y}}_{k+1}\right)^T \tag{A.25}$$

$$\bar{\boldsymbol{P}}_{\boldsymbol{yy},k+1} = \sum_{i=0}^{2(n_x+n_v)} \omega_c^i \left(\bar{\boldsymbol{y}}_{k+1}^i - \bar{\boldsymbol{y}}_{k+1}\right)\left(\bar{\boldsymbol{y}}_{k+1}^i - \bar{\boldsymbol{y}}_{k+1}\right)^T + \boldsymbol{R}_k, \tag{A.26}$$

where the weights are computed as

$$\omega_c^i = \begin{cases} \frac{\gamma}{n_x+n_v+\gamma} + 1 - \alpha^2 + \beta & i = 0 \\ \frac{1}{2(n_x+n_v+\gamma)} & i \in \{1, ..., 2(n_x + n_v)\} \end{cases} \tag{A.27}$$

The β here is also a tuning parameter in the UKF, and $\beta = 2$ is used when the state is modeled as Gaussian. Finally, the update state estimate and error covariance are

$$\hat{\boldsymbol{x}}_{k+1} = \bar{\boldsymbol{x}}_{k+1} + \bar{\boldsymbol{P}}_{\boldsymbol{xy},k+1}\bar{\boldsymbol{P}}_{\boldsymbol{yy},k+1}^{-1}\left(\boldsymbol{y}_{k+1} - \bar{\boldsymbol{y}}_{k+1}\right) \tag{A.28}$$

$$\boldsymbol{P}_{k+1} = \bar{\boldsymbol{P}}_{k+1} - \bar{\boldsymbol{P}}_{\boldsymbol{xy},k+1}\bar{\boldsymbol{P}}_{\boldsymbol{yy},k+1}^{-1}\bar{\boldsymbol{P}}_{\boldsymbol{xy},k+1}^T \tag{A.29}$$

The UKF is more computational expensive than the EKF, but still generally less expensive than IEKF. While the UKF retains higher order terms it can still diverge in some cases. One can improve the performance by adding more sigma points, but the cost is the increased computational time. This is the concept of particle filter, which estimate the state and error covariance based on Monte Carlo simulation.

APPENDIX B

FOURIER OPTICS

The optical propagation for phase retrieval in this chapter are produced using Fourier optics [94]. In this section we describe the relevant formulas for near and far-field propagation, including angular spectrum, Fresnel, and Fraunhofer propagations.

B.1 Rayleigh-Sommerfeld

Figure B.1 shows the propagation in between two coordinate frames. The diffracting aperture is at (ξ,η) plane and we calculate the wavefront at (x,y) plane.

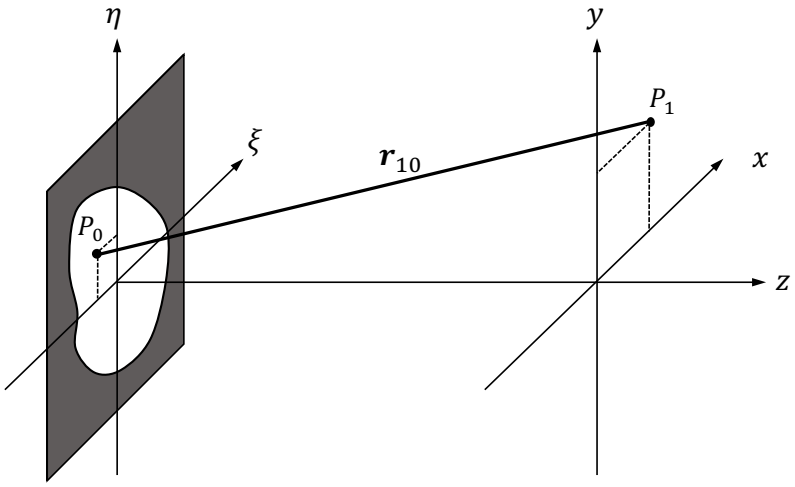

Figure B.1: Optical propagation between two coordinate planes (ξ,η) and (x,y).

Given the observation distance $r_{10} = \sqrt{z^2 + (x-\xi)^2 + (y-\eta)^2}$, the Huygens-

Fresnel principle states that

$$U(x,y) = \frac{z}{j\lambda}\iint U(\xi,\eta)\frac{\exp\left(jkr_{10}\right)}{r_{10}^2}d\xi d\eta. \tag{B.1}$$

This is derived from the scalar diffraction theory which neglect the possible coupling between the electric and magnetic fields. This approximation is good when the aperture and the propagation distance is relatively large compare to the wavelength of the light (i.e. $r_{10} \gg \lambda$). This is also known as angular spectrum propagation.

B.2 Fresnel Propagation

If the observation distance is approximated by

$$r_{10} \approx z\left[1 + \frac{1}{2}\left(\frac{x-\xi}{z}\right)^2 + \frac{1}{2}\left(\frac{y-\eta}{z}\right)^2\right], \tag{B.2}$$

then we have the Fresnel propagation equation written as

$$U(x,y) = \frac{e^{jkz}}{j\lambda z}\iint_{-\infty}^{\infty} U(\xi,\eta)\exp\left\{j\frac{k}{2z}\left[(x-\xi)^2 + (y-\eta)^2\right]\right\}d\xi d\eta. \tag{B.3}$$

This is also It can be written in a convolution form

$$U(x,y) = \iint_{-\infty}^{\infty} U(\xi,\eta)h(x-\xi, y-\eta)d\xi d\eta, \tag{B.4}$$

where the convolution kernel is

$$h(x,y) = \frac{e^{jkz}}{j\lambda z}\exp\left[j\frac{k}{2z}\left(x^2+y^2\right)\right]. \tag{B.5}$$

We rewrite this equation using Fourier convolution theorem

$$U(x,y) = \mathcal{F}^{-1}\left\{\mathcal{F}\left\{U(x,y)\right\}\mathcal{F}\left\{h(x,y)\right\}\right\} = \mathcal{F}^{-1}\left\{\mathcal{F}\left\{U_1(x,y)\right\}H(f_X,f_Y)\right\}, \tag{B.6}$$

where $\mathcal{F}\{\}$ and $\mathcal{F}^{-1}\{\}$ denote Fourier transform and its inverse respectively. $H(f_X, f_Y)$ is the Fourier transform of $h(x, y)$ and is calculated as

$$H(f_X, f_Y) = e^{jkz} \exp\left[-j\pi\lambda z(f_X^2 + f_Y^2)\right]. \tag{B.7}$$

The sufficient condition for Fresnel propagation is

$$z^3 \gg \frac{\pi}{4\lambda}\left[(x-\xi)^2 + (y-\eta)^2\right]_{max}^2. \tag{B.8}$$

However, this is a overly strict requirement and accurate result is expected for much shorter distance [94]. Another criterion is to use Fresnel number $N_F = \frac{a}{\lambda z}$, where a is half width of the aperture. The approximation works well the Fresnel number is in the order of magnitude of 1. For smooth fields over the source aperture a much higher Fresnel number is still acceptable [82].

The Fresnel propagation is considered near-field approximation. For propagation distance that satisfy

$$z \gg \frac{k(\xi^2 + \eta^2)_{max}}{2} \tag{B.9}$$

is far-field approximation and also called Fraunhofer approximation. The Fraunhofer propagation equation is given by

$$U(x, y) = \frac{e^{jkz} e^{j\frac{k}{2z}(x^2+y^2)}}{j\lambda z} \iint_{-\infty}^{\infty} U(\xi, \eta) \exp\left[-j\frac{2\pi}{\lambda z}(x\xi + y\eta)\right] d\xi d\eta. \tag{B.10}$$

BIBLIOGRAPHY

[1] A. Cusano, P. Pilla, L. Contessa, A. Iadicicco, S. Campopiano, A. Cutolo, M. Giordano, and G. Guerra, "High-sensitivity optical chemosensor based on coated long-period gratings for sub-ppm chemical detection in water," *Applied Physics Letters*, vol. 87, no. 23, p. 234105, 2005.

[2] R. F. Dantowitz, S. W. Teare, and M. J. Kozubal, "Ground-based high-resolution imaging of mercury," *The Astronomical Journal*, vol. 119, no. 5, p. 2455, 2000.

[3] J. Rolland and H. Hua, "Head-mounted display systems," *Encyclopedia of optical engineering*, pp. 1–13, 2005.

[4] N. Maeda, T. Fujikado, T. Kuroda, T. Mihashi, Y. Hirohara, K. Nishida, H. Watanabe, and Y. Tano, "Wavefront aberrations measured with hartmann-shack sensor in patients with keratoconus," *Ophthalmology*, vol. 109, no. 11, pp. 1996–2003, 2002.

[5] Y. Takaki and H. Ohzu, "Fast numerical reconstruction technique for high-resolution hybrid holographic microscopy," *Applied optics*, vol. 38, no. 11, pp. 2204–2211, 1999.

[6] M. Mihailescu, M. Scarlat, A. Gheorghiu, J. Costescu, M. Kusko, I. A. Paun, and E. Scarlat, "Automated imaging, identification, and counting of similar cells from digital hologram reconstructions," *Applied optics*, vol. 50, no. 20, pp. 3589–3597, 2011.

[7] C. Fienup and J. Dainty, "Phase retrieval and image reconstruction for astronomy," *Image Recovery: Theory and Application*, pp. 231–275, 1987.

[8] M. P. Lamb, C. Correia, J.-F. Sauvage, J.-P. Véran, D. R. Andersen, A. Vigan, P. L. Wizinowich, M. A. van Dam, L. Mugnier, and C. Bond, "Quantifying telescope phase discontinuities external to adaptive optics systems by use of phase diversity and focal plane sharpening," *Journal of Astronomical Telescopes, Instruments, and Systems*, vol. 3, no. 3, pp. 039001–039001, 2017.

[9] K. Nugent, T. Gureyev, D. Cookson, D. Paganin, and Z. Barnea, "Quantitative phase imaging using hard x rays," *Physical review letters*, vol. 77, no. 14, p. 2961, 1996.

[10] A. Kostenko, K. J. Batenburg, A. King, S. E. Offerman, and L. J. van Vliet, "Total variation minimization approach in in-line x-ray phase-contrast tomography," *Optics express*, vol. 21, no. 10, pp. 12185–12196, 2013.

[11] J. H. Bruning, D. R. Herriott, J. Gallagher, D. Rosenfeld, A. White, and D. Brangaccio, "Digital wavefront measuring interferometer for testing optical surfaces and lenses," *Applied optics*, vol. 13, no. 11, pp. 2693–2703, 1974.

[12] B. C. Platt and R. Shack, "History and principles of shack-hartmann wavefront sensing," *Journal of Refractive Surgery*, vol. 17, no. 5, pp. S573–S577, 2001.

[13] R. Tyson, *Adaptive optics engineering handbook*, vol. 67. CRC Press, 1999.

[14] H. Gong, O. Soloviev, D. Wilding, P. Pozzi, M. Verhaegen, and G. Vdovin, "Holographic imaging with a shack-hartmann wavefront sensor," *Optics express*, vol. 24, no. 13, pp. 13729–13737, 2016.

[15] L. Pueyo, J. Kay, N. J. Kasdin, T. Groff, M. McElwain, and R. Belikov, "Optimal dark hole generation via two deformable mirrors with stroke minimization," *Applied Optics*, vol. 48, no. 32, pp. 6296–6312, 2009.

[16] T. Groff, N. J. Kasdin, and M. A. Peters, "Focal plane wavefront estimation using an integral field spectrograph," in *Aerospace Conference, 2013 IEEE*, pp. 1–8, IEEE, 2013.

[17] D. Savransky, S. J. Thomas, L. A. Poyneer, D. W. Palmer, R. J. De Rosa, and M. Hartung, "Focal plane wavefront sensing and control for ground-based imaging," in *Proc. SPIE*, vol. 8447, 2012.

[18] R. A. Gonsalves and R. Chidlaw, "Wavefront sensing by phase retrieval," in *23rd Annual Technical Symposium*, pp. 32–39, International Society for Optics and Photonics, 1979.

[19] X. Wang, J. K. Wallace, and F. Shi, "Zernike wavefront sensor modeling development for lowfs on wfirst-afta," in *SPIE Optical Engineering+ Applications*, pp. 960528–960528, International Society for Optics and Photonics, 2015.

[20] F. Martinache, "The asymmetric pupil fourier wavefront sensor," *Publications of the Astronomical Society of the Pacific*, vol. 125, no. 926, p. 422, 2013.

[21] H. Lee, G. J. Hill, S. E. Tuttle, and B. L. Vattiat, "Fine optical alignment correction of astronomical spectrographs via in-situ full-field moment-based wavefront sensing," in *SPIE Astronomical Telescopes+ Instrumentation*, pp. 84500V–84500V, International Society for Optics and Photonics, 2012.

[22] A. Give'on, B. D. Kern, and S. Shaklan, "Pair-wise, deformable mirror, image plane-based diversity electric field estimation for high contrast coronagraphy," in *SPIE Optical Engineering+ Applications*, pp. 815110–815110, International Society for Optics and Photonics, 2011.

[23] A. E. Riggs, N. J. Kasdin, and T. D. Groff, "Recursive starlight and bias estimation for high-contrast imaging with an extended kalman filter," *Journal of Astronomical Telescopes, Instruments, and Systems*, vol. 2, no. 1, pp. 011017–011017, 2016.

[24] G. F. Hartig, J. E. Krist, A. R. Martel, H. C. Ford, and G. D. Illingworth, "On-orbit alignment and imaging performance of the hst advanced camera for surveys," in *Astronomical Telescopes and Instrumentation*, pp. 532–543, International Society for Optics and Photonics, 2003.

[25] B. Macintosh, J. R. Graham, P. Ingraham, Q. Konopacky, C. Marois, M. Perrin, L. Poyneer, B. Bauman, T. Barman, A. S. Burrows, A. Cardwell, J. Chilcote, R. J. De Rosa, D. Dillon, R. Doyon, J. Dunn, D. Erikson, M. P. Fitzgerald, D. Gavel, S. Goodsell, M. Hartung, P. Hibon, P. Kalas, J. Larkin, J. Maire, F. Marchis, M. S. Marley, J. McBride, M. Millar-Blanchaer, K. Morzinski, A. Norton, B. R. Oppenheimer, D. Palmer, J. Patience, L. Pueyo, F. Rantakyro, N. Sadakuni, L. Saddlemyer, D. Savransky, A. Serio, R. Soummer, A. Sivaramakrishnan, I. Song, S. Thomas, J. K. Wallace, S. Wiktorowicz, and S. Wolff, "First light of the Gemini Planet Imager," *Proceedings of the National Academy of Sciences*, vol. 111, no. 35, pp. 12661–12666, 2014.

[26] D. Savransky, S. J. Thomas, L. A. Poyneer, and B. A. Macintosh, "Computer vision applications for coronagraphic optical alignment and image processing," *Applied Optics*, vol. 52, no. 14, pp. 3394–3403, 2013.

[27] R. Galicher, P. Baudoz, G. Rousset, J. Totems, and M. Mas, "Self-coherent camera as a focal plane wavefront sensor: simulations," *Astronomy & Astrophysics*, vol. 509, p. A31, 2010.

[28] J. W. Figoski, T. E. Shrode, and G. F. Moore, "Computer-aided alignment of a wide-field, three-mirror, unobscured, high-resolution sensor,"

in *OE/LASE'89, 15-20 Jan., Los Angeles. CA*, pp. 166–177, International Society for Optics and Photonics, 1989.

[29] Z. Gao, L. Chen, S. Zhou, and R. Zhu, "Computer-aided alignment for a reference transmission sphere of an interferometer," *Optical Engineering*, vol. 43, no. 1, pp. 69–74, 2004.

[30] S. Kim, H.-S. Yang, Y.-W. Lee, and S.-W. Kim, "Merit function regression method for efficient alignment control of two-mirror optical systems," *Optics Express*, vol. 15, no. 8, pp. 5059–5068, 2007.

[31] H. Lee, G. B. Dalton, I. A. Tosh, and S.-W. Kim, "Computer-guided alignment ii: Optical system alignment using differential wavefront sampling," *Optics express*, vol. 15, no. 23, pp. 15424–15437, 2007.

[32] E.-S. Oh, S. Kim, Y. Kim, H. Lee, S.-W. Kim, and H.-S. Yang, "Integration of differential wavefront sampling with merit function regression for efficient alignment of three-mirror anastigmat optical system," in *SPIE Optical Engineering+ Applications*, pp. 77930F–77930F, International Society for Optics and Photonics, 2010.

[33] Z. Gu, C. Yan, and Y. Wang, "Alignment of a three-mirror anastigmatic telescope using nodal aberration theory," *Optics Express*, vol. 23, no. 19, pp. 25182–25201, 2015.

[34] R. W. Gerchberg, "A practical algorithm for the determination of phase from image and diffraction plane pictures," *Optik*, vol. 35, p. 237, 1972.

[35] J. R. Fienup, "Phase retrieval algorithms: a comparison," *Applied optics*, vol. 21, no. 15, pp. 2758–2769, 1982.

[36] C. Guo, C. Wei, J. Tan, K. Chen, S. Liu, Q. Wu, and Z. Liu, "A review of iterative phase retrieval for measurement and encryption," *Optics and Lasers in Engineering*, vol. 89, pp. 2–12, 2017.

[37] Y. Zhang, G. Pedrini, W. Osten, and H. J. Tiziani, "Whole optical wave field reconstruction from double or multi in-line holograms by phase retrieval algorithm," *Optics Express*, vol. 11, no. 24, pp. 3234–3241, 2003.

[38] Z. Liu, C. Guo, J. Tan, Q. Wu, L. Pan, and S. Liu, "Iterative phase-amplitude retrieval with multiple intensity images at output plane of gyrator transforms," *Journal of Optics*, vol. 17, no. 2, p. 025701, 2015.

[39] J. A. Rodrigo, H. Duadi, T. Alieva, and Z. Zalevsky, "Multi-stage phase retrieval algorithm based upon the gyrator transform," *Optics Express*, vol. 18, no. 2, pp. 1510–1520, 2010.

[40] G. Pedrini, W. Osten, and Y. Zhang, "Wave-front reconstruction from a sequence of interferograms recorded at different planes," *Optics letters*, vol. 30, no. 8, pp. 833–835, 2005.

[41] C. Guo, J. Tan, and Z. Liu, "Precision influence of a phase retrieval algorithm in fractional fourier domains from position measurement error," *Applied optics*, vol. 54, no. 22, pp. 6940–6947, 2015.

[42] C. Shen, J. Tan, C. Wei, and Z. Liu, "Coherent diffraction imaging by moving a lens," *Optics Express*, vol. 24, no. 15, pp. 16520–16529, 2016.

[43] F. Mosso, E. Peters, and D. G. Pérez, "Complex wavefront reconstruction from multiple-image planes produced by a focus tunable lens," *Optics letters*, vol. 40, no. 20, pp. 4623–4626, 2015.

[44] E. Peters, P. Clemente, E. Salvador-Balaguer, E. Tajahuerce, P. Andrés, D. G. Pérez, and J. Lancis, "Real-time acquisition of complex optical fields by binary amplitude modulation," *Optics letters*, vol. 42, no. 10, pp. 2030–2033, 2017.

[45] H. Karcher, J. Lammerding, H. Huang, R. T. Lee, R. D. Kamm, and M. R. Kaazempur-Mofrad, "A three-dimensional viscoelastic model for cell deformation with experimental verification," *Biophysical journal*, vol. 85, no. 5, pp. 3336–3349, 2003.

[46] M. Yokota, T. Kawakami, Y. Kimoto, and I. Yamaguchi, "Drying process in a solvent-based paint analyzed by phase-shifting digital holography and an estimation of time for tack free," *Applied optics*, vol. 50, no. 30, pp. 5834–5841, 2011.

[47] R. F. Stengel, *Optimal control and estimation*. Courier Dover Publications, 2012.

[48] J. Hedrick and A. Girard, "Control of nonlinear dynamic systems: Theory and applications," *Controllability and observability of Nonlinear Systems*, p. 48, 2005.

[49] E. Wan, R. Van Der Merwe, *et al.*, "The unscented kalman filter for nonlin-

ear estimation," in *Adaptive Systems for Signal Processing, Communications, and Control Symposium 2000. AS-SPCC. The IEEE 2000*, pp. 153–158, IEEE, 2000.

[50] S. J. Julier and J. K. Uhlmann, "New extension of the kalman filter to nonlinear systems," in *AeroSense'97*, pp. 182–193, International Society for Optics and Photonics, 1997.

[51] D. C. Redding, N. Sigrist, J. Z. Lou, Y. Zhang, P. D. Atcheson, D. S. Acton, and W. L. Hayden, "Optical state estimation using wavefront data," in *Optical Science and Technology, the SPIE 49th Annual Meeting*, pp. 212–224, International Society for Optics and Photonics, 2004.

[52] J. Z. Lou, D. Redding, N. Sigrist, Y. Zhang, and S. Basinger, "Jwst on-orbit multi-field wavefront control with a kalman filter," in *Optics & Photonics 2005*, pp. 58670T–58670T, International Society for Optics and Photonics, 2005.

[53] A. E. Riggs, N. J. Kasdin, and T. D. Groff, "Wavefront correction with kalman filtering for the wfirst-afta coronagraph instrument," in *SPIE Optical Engineering+ Applications*, pp. 960507–960507, International Society for Optics and Photonics, 2015.

[54] K. R. Rao and P. C. Yip, *The transform and data compression handbook*. CRC press, 2000.

[55] L. Devroye, L. Györfi, and G. Lugosi, *A probabilistic theory of pattern recognition*. Springer Verlag, 1996.

[56] U. Wandinger, "Introduction to lidar," in *Lidar*, pp. 1–18, Springer, 2005.

[57] O. Guyon, E. Pluzhnik, M. Kuchner, B. Collins, and S. Ridgway, "Theoretical limits on extrasolar terrestrial planet detection with coronagraphs," *The Astrophysical Journal Supplement Series*, vol. 167, no. 1, p. 81, 2006.

[58] G. Dial, H. Bowen, F. Gerlach, J. Grodecki, and R. Oleszczuk, "Ikonos satellite, imagery, and products," *Remote sensing of Environment*, vol. 88, no. 1, pp. 23–36, 2003.

[59] T. Toutin and P. Cheng, "Quickbird–a milestone for high-resolution mapping," *Earth Observation Magazine*, vol. 11, no. 4, pp. 14–18, 2002.

[60] R. Soummer, L. Pueyo, and J. Larkin, "Detection and characterization of exoplanets and disks using projections on karhunen-loève eigenimages," *The Astrophysical Journal Letters*, vol. 755, no. 2, p. L28, 2012.

[61] J. J. Moré, "The levenberg-marquardt algorithm: implementation and theory," in *Numerical analysis*, pp. 105–116, Springer, 1978.

[62] S. J. Julier and J. K. Uhlmann, "Unscented filtering and nonlinear estimation," *Proceedings of the IEEE*, vol. 92, no. 3, pp. 401–422, 2004.

[63] K. R. Muske and T. F. Edgar, "Nonlinear state estimation," in *Nonlinear process control*, pp. 311–370, Prentice-Hall, Inc., 1997.

[64] W. Lee and K. Nam, "Observer design for autonomous discrete-time nonlinear systems," *Systems & Control Letters*, vol. 17, no. 1, pp. 49–58, 1991.

[65] A. J. Whalen, S. N. Brennan, T. D. Sauer, and S. J. Schiff, "Observability and controllability of nonlinear networks: The role of symmetry," *Physical Review X*, vol. 5, no. 1, p. 011005, 2015.

[66] O. Albert, L. Sherman, G. Mourou, T. Norris, and G. Vdovin, "Smart microscope: an adaptive optics learning system for aberration correction in multiphoton confocal microscopy," *Optics letters*, vol. 25, no. 1, pp. 52–54, 2000.

[67] T. Coenen, B. J. Brenny, E. J. Vesseur, and A. Polman, "Cathodoluminescence microscopy: Optical imaging and spectroscopy with deep-subwavelength resolution," *MRS Bulletin*, vol. 40, no. 04, pp. 359–365, 2015.

[68] T. Kakue, T. Nishitsuji, T. Kawashima, K. Suzuki, T. Shimobaba, and T. Ito, "Aerial projection of three-dimensional motion pictures by electroholography and parabolic mirrors," *Scientific reports*, vol. 5, 2015.

[69] S. B. Howell, *Handbook of CCD astronomy*, vol. 5. Cambridge University Press, 2006.

[70] R. G. Paxman, T. J. Schulz, and J. R. Fienup, "Joint estimation of object and aberrations by using phase diversity," *JOSA A*, vol. 9, no. 7, pp. 1072–1085, 1992.

[71] M. Guizar-Sicairos and J. R. Fienup, "Phase retrieval with transverse

translation diversity: a nonlinear optimization approach," *Optics express*, vol. 16, no. 10, pp. 7264–7278, 2008.

[72] P. Netrapalli, P. Jain, and S. Sanghavi, "Phase retrieval using alternating minimization," in *Advances in Neural Information Processing Systems*, pp. 2796–2804, 2013.

[73] J. Zhong, L. Tian, P. Varma, and L. Waller, "Nonlinear optimization algorithm for partially coherent phase retrieval and source recovery," *IEEE Transactions on Computational Imaging*, vol. 2, no. 3, pp. 310–322, 2016.

[74] S. T. Thurman, R. T. DeRosa, and J. R. Fienup, "Amplitude metrics for field retrieval with hard-edged and uniformly illuminated apertures," *JOSA A*, vol. 26, no. 3, pp. 700–709, 2009.

[75] A. S. Jurling and J. R. Fienup, "Applications of algorithmic differentiation to phase retrieval algorithms," *JOSA A*, vol. 31, no. 7, pp. 1348–1359, 2014.

[76] F. Rigaut, B. Neichel, and D. Gratadour, "Opra otf-based phase retrieval analysis package." `https://github.com/frigaut/yorick-opra`, 2011.

[77] R. Conan, C. Correia, *et al.*, "Object-oriented matlab adaptive optics toolbox," in *Proc. SPIE*, SPIE, 2014.

[78] B. H. Dean, D. L. Aronstein, J. S. Smith, R. Shiri, and D. S. Acton, "Phase retrieval algorithm for jwst flight and testbed telescope," in *Proc. SPIE*, vol. 6265, p. 626511, 2006.

[79] E. A. Wan, R. Van Der Merwe, and A. T. Nelson, "Dual estimation and the unscented transformation.," in *NIPS*, vol. 12, pp. 666–672, 1999.

[80] S. Roweis and Z. Ghahramani, "Learning nonlinear dynamical systems using the expectation–maximization algorithm," *Kalman filtering and neural networks*, vol. 6, pp. 175–220, 2001.

[81] J. D. Schmidt, "Numerical simulation of optical wave propagation with examples in matlab," in *SPIE PRESS BOOK*, SPIE Bellingham, Washington, USA, 2010.

[82] D. G. Voelz, *Computational fourier optics: a MATLAB tutorial*. Spie Press Bellingham, WA, 2011.

[83] A. S. Jurling and J. R. Fienup, "Phase retrieval with unknown sampling factors via the two-dimensional chirp z-transform," *JOSA A*, vol. 31, no. 9, pp. 1904–1911, 2014.

[84] R. Soummer, L. Pueyo, A. Sivaramakrishnan, and R. J. Vanderbei, "Fast computation of lyot-style coronagraph propagation," *Optics Express*, vol. 15, no. 24, pp. 15935–15951, 2007.

[85] R. J. Noll, "Zernike polynomials and atmospheric turbulence," *JOsA*, vol. 66, no. 3, pp. 207–211, 1976.

[86] J. R. Fienup, "Invariant error metrics for image reconstruction," *Applied optics*, vol. 36, no. 32, pp. 8352–8357, 1997.

[87] A. P. Dempster, N. M. Laird, and D. B. Rubin, "Maximum likelihood from incomplete data via the em algorithm," *Journal of the royal statistical society. Series B (methodological)*, pp. 1–38, 1977.

[88] C. B. Do and S. Batzoglou, "What is the expectation maximization algorithm?," *Nature biotechnology*, vol. 26, no. 8, pp. 897–899, 2008.

[89] R. H. Shumway and D. S. Stoffer, "An approach to time series smoothing and forecasting using the em algorithm," *Journal of time series analysis*, vol. 3, no. 4, pp. 253–264, 1982.

[90] M. L. Psiaki, "Backward-smoothing extended kalman filter," *Journal of guidance control and dynamics*, vol. 28, no. 5, pp. 885–894, 2005.

[91] S. S. Haykin, *Kalman filtering and neural networks*. Wiley Online Library, 2001.

[92] G. Einicke, *Smoothing, Filtering and Prediction: Estimating the Past, Present and Future.* InTechOpen, 2012.

[93] J. Fang and D. Savransky, "Amplitude and phase retrieval with simultaneous diversity estimation using expectation maximization," *JOSA A*, vol. 35, no. 2, pp. 293–300, 2018.

[94] J. Goodman, *Introduction to Fourier optics*. McGraw-hill, 2008.

[95] R. D. Fiete, "Image quality and [lambda] fn/p for remote sensing systems," *Optical Engineering*, vol. 38, no. 7, pp. 1229–1241, 1999.

[96] M. Esseling, *Photorefractive optoelectronic tweezers and their applications*. Springer, 2014.

[97] D. C. Ghiglia and M. D. Pritt, *Two-dimensional phase unwrapping: theory, algorithms, and software*, vol. 4. Wiley New York, 1998.

[98] R. M. Goldstein, H. A. Zebker, and C. L. Werner, "Satellite radar interferometry: Two-dimensional phase unwrapping," *Radio science*, vol. 23, no. 4, pp. 713–720, 1988.

[99] P. Annibale, A. Dvornikov, and E. Gratton, "Optical measurement of focal offset in tunable lenses," *Optics express*, vol. 24, no. 2, pp. 1031–1036, 2016.

[100] A. Faridian, D. Hopp, G. Pedrini, U. Eigenthaler, M. Hirscher, and W. Osten, "Nanoscale imaging using deep ultraviolet digital holographic microscopy," *Optics express*, vol. 18, no. 13, pp. 14159–14164, 2010.